Ph.D Thesis

First Principles Study of Layered and Molecular solids

Appalakondaiah Samudrala

ACRHEM, School of Physics
University of Hyderabad
Hyderabad - 500 046

First Principles Study of Layered and Molecular Solids

A Thesis submitted to University of Hyderabad for the award of the degree of

Doctor of Philosophy

in Physics

by

Appalakondaiah Samudrala
(09ACPA09)

ACRHEM, School of Physics
University of Hyderabad
Hyderabad-500 046
May 2015

Dedicated to

My Grandmother

Declaration

I, Appalakondaiah Samudrala, hereby declare that the work presented in this thesis has been carried out by me under the supervision of Dr. G. S. Vaitheeswaran, ACRHEM, School of Physics, University of Hyderabad, Hyderabad, India, as per the Ph.D. ordinances of the University. I declare, to the best of my knowledge, that no part of this thesis has been submitted for the award of a research degree of any other University. I hereby agree that my thesis can be deposited in Shodhganga/INFLIBNET.

(Appalakondaiah Samudrala)
Reg. No: 09ACPA09.

Certificate

This is to certify that the thesis entitled ***First Principles Study of Layered and Molecular Solids*** being submitted to the University of Hyderabad by **Appalakondaiah Samudrala** (Reg. No. 09ACPA09), for the award of the degree of Doctor of Philosophy in Physics, is a record of *bonafide* work carried out by him under my supervision and is free of plagiarism.

The matter embodied in this report has not been submitted to any other University or Institution for the award of any degree or diploma.

Dr. G. S. Vaitheeswaran,
Thesis Supervisor,
ACRHEM, School of Physics,
University of Hyderabad.

Director,
ACRHEM,
University of Hyderabad.

Dean,
School of Physics,
University of Hyderabad.

A word of Gratitude

I would not have completed my research work and write this thesis without kind support and help of several people.

First and foremost I would like to express sincere thank to my supervisor **Dr. G. S. Vaitheeswaran** for opening the doors of guidance, continuous support, scholarly inputs and consistent encouragement I received throughout the research work. This thesis would not have been possible without his assistance and allow me to discuss with so many experts in my research community. I cannot thank him enough and I am grateful to him forever.

I extend my gratitude to **Prof. N. E. Christensen** and **Prof. A. Svane**, Institute of Physics and Astronomy, Aarhus University, Denmark for the valuable academic discussions and suggestions. I would like to extent my thank to **Dr. S. Lebègue**, Université de Lorraine, France for intimacy in my thesis work, providing several stages of computations, discuss ideas with me as well as give insightful comments. It is my great pleasure to thank **Dr. V. Kanchana**, Indian Institute of Technology, Hyderabad, India, provide her computational facilities and helping me throughout writing of my thesis. I acknowledge her for being in forefront to help me in any regard.

I would like to thank **Prof. K. P. N. Murthy**, **Prof. S. P. Tewari**, and **Dr. G. Manoj Kumar** University of Hyderabad for showing their straightforward approach to problems, art of imparting knowledge and skills have been instructive and inspirational to me. A special thanks goes to **Prof. M. C. Valsakumar**,SEST, University of Hyderabad, for showing his interest on my research work, fruitful discussions, being always ready to help and answer all my queries.

It has been a very pleasant experience to work in the warm and friendly atmosphere of my group members N. Yedukondalu, E. Narsimha Rao, and senior lab-mates K. Ramesh Babu and Ch. Bheemalingam. I think we have learnt many things from each other during our interesting discussions, good times we spent together. I would like to thank all my ACRHEM and School of Physics friends for helping and supporting me unconditionally on this long and sometimes difficult journey and for being with me whenever I needed. The memories and stories from time we spent together would fill a book thicker than this one. I would like to express my thanks to close friends Sreedhar, Kalyan Chandrakanth, Vasu, Suman Kalyan, Satish and Swathi for their support. I have to mention my special thanks to my friend G. Vijay Kumar and his wife Sravanthi for the encouragement and moral support they have given. Last but not least, I would like to thank to **DRDO**, India through **ACRHEM** for their financial support, present and former directors of **ACRHEM** for administrative support.

Contents

List of Figures

List of Tables

Chapter 1

Introduction

The fundamental problem in theoretical physics, chemistry and biology is towards understanding the structure and dynamics of many-electron systems by solving quantum mechanical equations. Here, the *systems* which we refer ranges from atoms, molecules, simple solids to surfaces and complex-crystals, where the number of electrons in any of these systems are large. Specifically, description and understanding of weakly interacting forces in molecular as well as layered solids are important to address the structural stability in most of the branches of science. Density-functional theory (DFT) [1, 2] is a well established computational approach, which determines various properties with low computational cost by using an approximated functional of ground state electron density. By means of state of the art DFT methods, great achievements were visualised in obtaining results for variety of systems, ranging from the total energies of basic geometries to stability of crystal structure, electronic structure, spectroscopy, magnetism, and many more. On the other hand, computational modelling of weakly (dispersive) interacting solids using DFT methods always yields results which are not accurate enough when compared with experiments. This inaccuracy in DFT results is due to insufficiencies in taking account of the asymptotic dependence of the potential for interacting atoms/molecules at large separations which shows non local nature. Although, dispersive forces are much weaker, these are crucial for the formation of chemical systems such as noble gas solids, layered materials, molecular crystals, biological systems and and many more. Particularly, van der Waals (vdW) interactions and hydrogen bonding are known to be important for correct description of structure as well as stability. It is also essential in predicting the ground state as well as high pressure structures in terms of variety of polymorphs as well as co-crystals for a given system. Here the precession of the results obtained from DFT methods mainly dependent on the exchange-correlation (*XC*) energy functional used in the calculations [3–6].

Indeed, *XC*-functionals utilize the electron density as an input, which describes the intricate many-body interactions into single particle formalism in solids. The progress and development of new *XC* functionals is indeed a popular choice of research and in this aspect, many approximations exist, starting from the local density approximation (LDA), generalized gradient approximations (GGAs), and extends "beyond GGA". Here LDA utilizes just the local electron density and GGA introduces the density gradient. The obtained total energy from these XC-functionals contribute to a small fraction of the total energies of the system, but it turns out to be crucial for the accurate description of binding in solids. Till date, the known XC-functionals such as LDA and GGA were popular, and are successful in describing the geometric properties of ionic, covalent and metallic systems. On the other hand, these functionals often show difficulties in explaining the properties such as (a) cohesion of weakly bounded systems (known as vdW interactions and hydrogen bonding in layered and molecular crystals) (b) predicting or reproducing the fundamental electronic band gap of the solids.

In a simple view, using the standard DFT- *XC* functionals result in extensive errors, which causes qualitative failure in predicted cohesion properties in soft materials. In the case of hard materials with either covalent/or ionic bonding , the cohesive energy per atom is typically in the order of eV scale. Also, the respective bond lengths are 2 - 3 Å, and the obtained DFT results are in good agreement with experimental results and can offer a broad perspective on the interpretation as well as theoretical predictions. If we consider soft materials, where the dispersive forces are found to dominant, the typical cohesive energy/atom is in the order of few meV range, also very less compared to hard materials. Here the corresponding bond lengths are above 3 Å, which means that dispersive interactions are totally inter (intra) molecular interactions. In this bonding, charge of one molecule (atom) is correlated with a nearby molecule and thus dispersive forces arises from their instantaneous fluctuating atomic or molecular dipoles. Presumably this was known for a quite long time and, many encouraging ideas were proposed to overcome the challenging failure which arise from dispersive interactions. Among numerous approaches to treat dispersive interactions, additive pair wise corrections with standard DFT, many body calculations using random phase approximation and non-local vdW functions were accounted for obtaining improved results over standard DFT [7–13]. These methods are well benchmarked and achieved the desired results for noble gas solids, layered (also chain like) solids such as graphene, h-BN, and complex organic molecular solids (some e.g.s are cubic nitrogen and its dimers, benzene [14–23].

Although, the accuracy of these approaches are very good in critical examination of lattice energies as well as geometries, performance of these methods were not equally good for all the systems. Some of the examples are D2's (Grimme proposed in 2006) method, which is widely used to study the binding properties of various solids and the structure and dynamics of molecular spin crossover compounds [24]. The OBS method with PW91 functional is also successfully used, as exemplified in the study of the interaction between NO_2 molecules and the Au-111 surface [25]. The method of TS is also very popular and was used recently to study the hydrogen bonds of ice under pressure [26] and the interlayer sliding energy landscape of hexagonal boron nitride [27]. It is also to be noted that the available reports with different dispersion correction methods were limited up to reproducing the cohesive energies, lattice parameters as well bulk moduli of a set of selected systems for the ground state structures. The central goal of this thesis is to extend to testing different dispersion correction methods for wide range of systems and to examine the performance of various dispersion correction methods from elemental to complex systems at ambient and high pressure conditions. Further, the effect of pressure on dispersive interactions were examined via bond lengths, bond angles and pressure coefficients of lattice parameters.

Apart from the lack of treating the dispersion interactions in standard DFT, the other general drawback is predicting (and reproducing) the band gap from Kohn-Sham eigenvalues. Unfortunately, the Kohn-Sham calculations strongly underestimate band gaps, often by more than a factor of 30-40 % compared with experiments due to derivative discontinuity of standard LDA or GGA *XC* functionals. Nowadays, several methods such as Hybrid functional like HSE [28, 29], Tran and Blaha modified Becke Johnson (TB-mBJ) [30, 31] potential and GW approximation [32, 33] are available to overcome this problem. Among them, GW approximation has emerged as primary computational tool for predicting electronic properties of insulators, semiconductors and band widths of metals [34, 35]. Earlier, GW method was successful in predicting or reproducing the band gaps of alkali hydrides, transition metal compounds with semicore *d*-sates, insulator to metal transitions (or vice versa), chemical bonding and many more [36–44]. In addition, the obtained quasiparticle energies within the GW approximation may be used as an input for accurate description of optical properties, and also to obtain the excitonic effects of solids by solving Bethe-Salpeter equation. It is to be noted that success over the use of the GW approximation to study materials and molecules still faces several numerical challenges and also computationally expensive.

The underlying idea of this thesis is to use the recently developed dispersion correction DFT methods and quasiparticle band gaps for large molecular (layered) solids and stressing the importance of advanced methods for predicting accurate ground state properties. The outline of the current thesis is as follows: in chapter 2, we present theory behind the computational methods used throughout this thesis. This includes a short view of DFT approximations, recent advances in DFT for treating weak interactions. Apart from these, we also discuss the basic information about quasiparticle electronic structure calculations using GW approximation.

Chapter 3 presents testing of several dispersion correction methods with standard DFT methods at low pressure regions and aims to investigate the systematic deviations with experiments in structural, elastic and vibrational properties using the same methods. For this, we have chosen elemental phosphorus as an example, which possess diverse applications similar to the known family of 2D materials such as graphene, BN and MoS_2 etc., Similar to the carbon, 3D form of phosphorus also exists in several allotropic forms, and among them black phosphorus is stable under normal conditions. From the puckered layered structure of black phosphorus, it is well known that the bonding between phosphorus layers is from vdW interactions, and these interactions are not accounted in the standard DFT methods. On the other hand, the structural properties, elastic constants and vibrational properties obtained with dispersion corrected methods are found to be in excellent agreement with experiments, which indicated the necessity of dispersion corrected DFT methods in first principles calculations.

Chapter 4 provides the detailed results on structural and vibrational properties of molecular solid XeF_2 under hydrostatic pressure conditions. Here the present calculations show that, inclusions of van der Waals corrections to standard DFT methods are important in order to obtain a good agreement between the calculated and experimental structural parameters at ambient conditions. Also, weak intra and inter-molecular interactions are considered as most important at low pressures up to 5 GPa, and almost negligible beyond 10 GPa. In contradiction to recent experimental high pressure study, the present calculations indicate the stability of parent I4/mmm phase upto 110 GPa through energetics and phonon dispersion relations.

Chapter 5 encompasses the structural and vibrational properties of complex molecular solids such as nitromethane and FOX-7 under hydrostatic pressure conditions. Our calculations reproduce the experimental trends in the ground state structural properties. The equation of state (EOS), bulk moduli, and pressure coefficients of lattice parameters are examined under hydrostatic pressure conditions. The present calculations clearly reveal the predominant role of hydrogen bonding in addressing phase stability under pressure. In the case of solid nitromethane, we found a discontinuity in the bond length, bond angles, and also a weakening of hydrogen bond strength in the pressure range from 10 to 12 GPa, picturing the structural transition from phase I to II. This is also examined by the zone center internal and external modes of this material under pressure upto 30 GPa. For FOX-7, we found a significant increment in the N–H...O hydrogen bond strength under hydrostatic compression up to 10 GPa. This is explained by the change in bond lengths and calculated IR spectra under pressure.

Chapter 6, gives the details of the calculations for a several C-H-N-O based energetic materials to explore structural and electronic properties. A comprehensive comparison of theoretical ground state volumes and bulk moduli with available experiments were done by employing various dispersion correction methods applied to the standard PBE functional. Furthermore, we examine the mean absolute deviation of each dispersion correction method for several energetic solids. This chapter brings out the fact that there exists no unique dispersion correction method which is found to be appropriate for all organic energetic solids. This work also emphasizes the importance of quasiparticle band structure calculations in predicting exact band gap, which plays a key role in electronic excitations and further useful in determining the optical absorption as well as decomposition mechanisms.

Finally chapter 7, summarizes the present thesis, open up with future scopes and ideas leading to further explorations of energetic solids are presented.

References

[1] P. Hohenberg and W. Kohn, Phys. Rev., **136**, B864 (1964).

[2] W. Kohn and L. J. Sham, Phys. Rev., **140**, B1133 (1965).

[3] D. M. Ceperley and B. J. Alder, Phys. Rev. Lett., **45**, 566 (1980).

[4] J. P. Perdew and A. Zunger, Phys. Rev. B, **23**, 5048 (1981).

[5] J. P. Perdew and Y. Wang, Phys. Rev. B, **45**, 13244 (1992).

[6] J. P. Perdew, K. Burke and M. Ernzerhof, Phys. Rev. Lett., **77**, 3865 (1996).

[7] S. Grimme, J. Compu. Chem., **27**, 1787-1799 (2006).

[8] S. Grimme, S. Ehrlich and L. Goerigk, J. Compu. Chem., **32**, 1456 (2011).

[9] A. Tkatchenko and M. Scheffler, Phy. Rev. Lett., **102**, 073005 (2009).

[10] A. Tkatchenko, R. A. Di. Stasio, R. Car and M. Scheffler, Phy. Rev. Lett., **108**, 236402 (2012).

[11] M. Dion, H. Rydberg, E. Schröder, D. C. Langreth and B. I. Lundqvist, Phy. Rev. Lett., **92**, 246401 (2004).

[12] J. Harl and G. Kresse, Phys. Rev. Lett., **103**, 056401 (2009).

[13] J. Harl, L. Schimka and G. Kresse, Phys. Rev. B, **81**, 115126 (2010).

[14] T. Bucko, J. Hafner, S. Lebègue and J. G. Ángyán, J. Phys. Chem. A, **114**, 11814 (2010),.

[15] A. O. -D. -L. Roza and E. R. Johnson, J. Chem. Phys., **137**, 054103:1-10 (2012).

[16] J. Klimes and A. Michaelides, J. Chem. Phys., **137**, 120901:1-12 (2012).

[17] T. Risthaus and S. Grimme, J. Chem. Theory Comput., **9**, 1580 (2013).

[18] T. Bucko, S. Lebègue, J. Hafner and J. G. Ángyán, Phy. Rev. B, **87**, 064110-1:15 (2013).

[19] K. Berland and P. Hyldgaard, Phy. Rev. B, **87**, 205421-1:15 (2013).

[20] T. Bucko, S. Lebègue, J. Hafner and J. G. Ángyán, J. Chem. Theory Comput., **9**, 4293 (2013).

[21] A. M. Reilly and A. Tkatchenko, J. Phys. Chem. Lett., **4**, 1028 (2013).

[22] T. Bucko, S. Lebègue, J. Hafner and J. G. Ángyán, J. Chem. Phys., **141**, 034114 (2014).

[23] J. Moellmann and S. Grimme, J. Phys. Chem. C, **118**, 7615 (2014).

[24] T. Bucko, J. Hafner, S. Lebègue, and J. G. Angyán, Phys. Chem. Chem. Phys., **14**, 5389 (2012).

[25] T. F. Zhang, M. Sacchi, D. A. King, and S. M. Driver, J. Phys. Chem. C, **116**, 5637 (2012).

[26] B. Santra, J. Klimes, D. Alfe, A. Tkatchenko, B. Slater, A. Michaelides, R. Car, and M. Scheffler, Phys. Rev. Lett., **107**, 185701 (2011).

[27] N. Marom, J. Bernstein, J. Garel, A. Tkatchenko, E.Joselevich, L. Kronik, and O. Hod, Phys. Rev. Lett., **105**, 046801 (2010).

[28] J. Heyd, G. Scuseria and M. Ernzerhof, J. Chem. Phys., **118**, 8207 (2003).

[29] A. V. Krukau, O. A. Vydrov, A. F. Izmaylov and G. Scuseria, J. Chem. Phys., **125**, 224106 (2006).

[30] F. Tran and P. Blaha, Phys. Rev. Lett., **102**, 226401, (2009).

[31] D. Koller, F. Tran and P. Blaha, Phys. Rev. B, **83**, 195134, (2011).

[32] John P. Perdew and Mel Levy, Phys. Rev. Lett., **51**, 1884-1887 (1983).

[33] R. O. Jones and O. Gunnarsson, Rev. Mod. Phys., **61**, 689-746 (1989).

[34] S. Lebègue, B. Arnaud, M. Alouani and P. E. Blöchl, Phys. Rev. B, **67**, 155208 (2003).

[35] R. H. Scheicher, D. Y. Kim, S. Lebègue, B. Arnaud, M. Alouani and R. Ahuja, Appl. Phys. Lett., **92**, 201903 (2008).

[36] W. -D. Schone and A. G. Eguiluz, Phys. Rev. Lett., **81**, 1662 (1998).

[37] B. Arnaud and M. Alounai, Phys. Rev. B, **62**, 4464 (2000).

[38] A. Fleszar and W. Hanke, Phys. Rev. B, **71**, 045207 (2005).

[39] P. E. Trevisanutto, C. Giorgetti, L. Reining, M. Ladisa and V. Olevano, Phys. Rev. Lett., **101**, 226405 (2008).

[40] K. Kaasbjerg and K. S. Thygesen, Phys. Rev. B, **81**, 085102 (2010).

[41] T. Kaewmaraya, D. Y. Kim, S. Lebègue, C. J. Pickard, R. J. Needs and R. Ahuja, Phys. Rev. B, **84**, 092101 (2011).

[42] S. Lany, Phys. Rev. B, **87**, 085112 (2013).

[43] F. Karlicky and M. Otyepka, J. Chem. Theory. Comput., **9**, 4155 (2013).

[44] M. A. Kochman and C. A. Morrison, J. Chem. Theory. Comput., **9**, 1182 (2013).

Chapter 2

Theoretical methods

In this chapter we present the details of the theoretical techniques used in calculating various physical and chemical properties of the layered as well as molecular solids. We also present the basic principles of density functional theory (DFT), local density approximation(LDA), and generalized gradient approximation(GGA) along with semi-empirical dispersion corrections to the density functional theory. The computational methods used in the DFT implementations are also described. Apart from this, we formally shown the basic formulism of quasiparticle corrections to the standard DFT methods.

2.1 Density Functional Theory(DFT)

In order to describe an interacting electron-nucleus system one has to write the corresponding Hamiltonian as follows [1–3]:

$$H = -\sum_{I=1}^{P} \frac{\hbar^2}{2M_I}\nabla_I^2 - \sum_{i=1}^{N} \frac{\hbar^2}{2m_i}\nabla_i^2 + \frac{e^2}{2}\sum_{I=1}^{P}\sum_{J\neq I}^{P} \frac{Z_I Z_J}{|R_I - R_J|} + \frac{e^2}{2}\sum_{i=1}^{N}\sum_{i\neq j}^{N} \frac{1}{|r_i - r_j|} \tag{2.1}$$

where $R = \{R_I, I = 1, 2, ...P\}$ is a set of P nuclear coordinates, and $r = \{r_i, i = 1, 2, ...N\}$ is a set of N electronic coordinates. Z_I and M_I are the nuclear charges and masses, respectively. The first and second terms correspond to the kinetic energy operators for nuclei and electrons, whereas the third, fourth and fifth terms are the potential operators that describe the nucleus-nucleus, electron-electron and electron-nucleus interactions, respectively. In order to study the properties of an interacting electron-nucleus system, one has to solve the time-independent Schrödinger equation:

$$H\Psi_n(R,r) = \varepsilon_n \Psi_n(R,r) \tag{2.2}$$

where ε_n are the energy eigenvalues and $\Psi_n(R,r)$ are the corresponding eigenstates or wave functions. This problem is almost impossible to treat within quantum mechanical frame work, except for the hydrogen atom. There are several features that contribute to this difficulty, but the most important among them is the multi component many body nature of the system, and the two body nature of the Coulomb interaction which makes the above Schrödinger equation inseparable. The usual choice to solve the above complicated equation is to resort to a few reasonable and well-controlled approximations, which encompass a wide variety of problems of interest.

Born and Oppenheimer [4] proposed a scheme for separating the motion of nuclei from that of the electrons. The nuclei are much heavier than the electrons and consequently much slower, so the effects of nuclei are treated as an external potential applied to the electrons. Therefore, the wave function can now be written as the product of the electronic and ionic wave functions, with the electronic part being obtained by solving the following Schrödinger equation

$$H_e\psi_e(R,r) = \varepsilon_e\psi_e(R,r) \tag{2.3}$$

with the electronic Hamiltonian given by

$$H_e = -\sum_{i=1}^{N} \frac{\hbar^2}{2m_i}\nabla_i^2 + \frac{e^2}{2}\sum_{i=1}^{N}\sum_{i\neq j}^{N} \frac{1}{|r_i - r_j|} - \frac{e^2}{2}\sum_{I=1}^{P}\sum_{i=1}^{N} \frac{Z_I}{|R_I - r_i|} \tag{2.4}$$

$$H_e = T + U + V \tag{2.5}$$

where T represents the kinetic energy operator, V represents the external potential (i.e electron-nucleus interaction) and U represents the electron-electron interaction. Within the Born-Oppenheimer approximation the complexity of the system is significantly reduced. However, the problem is still too difficult to be solved due to the electron-electron interaction. Indeed the electrons in any of solid systems cannot be treated as like non interacting classical particles, and the main difficulty is that electrons interact among themselves via Coulomb two-body forces. For an atom with Z electrons, the probability of finding an electron in space depends on the location of the (Z-1) electrons, so that they can not be considered as individual entities. This phenomenon is known as *correlation*. Therefore, the concept of one-electron wave functions can not be applicable in many cases. The wave function of many-electron system cannot be simply written as the product of the wave functions of individual electrons. Many approaches have been developed starting from Hartree-Fock method to density functional theory (DFT) to solve the above equation. In this thesis, we have used the DFT method, which is explained in the following sections.

2.1.1 The Hohenberg-Kohn Theorems

L.H. Thomas [5] and E. Fermi [6] proposed that the full electronic density is the fundamental variable of the many-body problem. Thomas and Fermi approach was developed with the hope that the energy can be written exclusively in terms of the electronic density. In 1964, Hohenberg and Kohn [7] formulated and proved a theorem that put on solid mathematical ground the ideas of Thomas and Fermi. Based on these theorems Hohenberg and Kohn formulated *density functional theory* as an exact theory of many-body systems. It is applicable to any system of interacting particles. The theorems are as follows:

Theorem I: For any system of interacting particles in an external potential $V_{ext}(r)$, this potential is determined uniquely by the ground-state particle density $n(r)$.

There is a one-to-one correspondence between the potential and the ground state particle density $n(r)$. The ground state expectation value of any observable is a unique functional of the ground state particle density.

Theorem II: An universal functional for the energy $E[n(r)]$ can be defined, valid for any $V_{ext}(r)$.

For a particular $V_{ext}(r)$ the ground state energy of the system is the global minimum of $E[n(r)]$. The density $n(r)$ that minimizes $E[n(r)]$ is the ground state density.

2.1.2 The Kohn-Sham equations

Kohn and Sham have developed a frame work based on the Hohenberg and Kohn theorems that can be applied for practical problems [8]. The main idea consists in replacing the interacting many-body problem by a corresponding non-interacting particle system in an appropriate external potential. It is useful to decouple the kinetic energy, $T[n]$ into two parts (non-interacting system + rest term)as $T[n] = T_s[n] + T_c[n]$, where $T_s[n]$ is the kinetic energy of the non-interacting system and $T_c[n]$ represents the remainder. $T_s[n]$ is not known as a functional of n, but it can be expressed in terms of the single-particle orbitals, $\phi_i(r)$, of a non-interacting system with density n via

$$T_s[n] = -\frac{1}{2}\sum_{\sigma}\sum_{I=1}^{N}\int dr\phi_i{}^*(r)\nabla^2\phi_i(r). \tag{2.6}$$

For a system containing an even number of spin-up and spin-down electrons the density of the original many-body system can be written in terms of the orbitals as

$$n(r) = \sum_{\sigma} n(r,\sigma) = \sum_{\sigma}\sum_{I=1}^{N}|\phi_i(r)|^2. \tag{2.7}$$

Thus, all $\phi_i(r)$ are functionals of n and since T_s is an explicit orbital functional it is also an implicit density functional, $T_s[n] = T_s[\phi_i[n]]$. Moreover the total number of electrons N is a simple functional of the density

$$N = \int n(r)dr \tag{2.8}$$

The classical Coulomb self-interaction energy of the electron density, i.e., Hartree energy is defined as

$$U_H[n] = \frac{1}{2}\int\int drdr'\frac{n(r)n(r')}{|r-r'|} = \frac{1}{2}\int V_C(r)n(r)dr \tag{2.9}$$

where $V_C(r) = \int dr\frac{n(r)}{|r-r'|}$ and the energy of the external potential can be written as a functional of the density

$$\int n(r)V_{ext}(r)dr \tag{2.10}$$

The Kohn-Sham approach [8] is to rewrite the energy functional of the interacting system in the form

$$\begin{aligned} E_{KS}[n] &= T[n] + U[n] + V[n] \\ &= T_s[\phi_i[n]] + U_H[n] + E_{xc}[n] + V_{ext}[n] \\ &= T_s[n] + \int n(r)[V_{ext}(r) + \frac{1}{2}V_C(r)]dr + E_{xc}[n] \\ &= T_s[n] + V_{eff}. \end{aligned} \tag{2.11}$$

Where $V_{eff} = \int n(r)[V_{ext}(r) + \frac{1}{2}V_C(r)]dr + E_{xc}[n]$, The exchange-correlation energy $E_{xc}[n]$ contains the differences between $T - T_s$(i.e. T_C) and $U - U_H$. One has to find a good approximation to E_{xc} in order to get good results for real materials. The effective Hamiltonian for a system of non-interacting particles moving in a potential called V_{KS}, constructed so that the total density of the system is the same as for the real system of interacting electrons, is

$$V_{KS}(r) = V_{ext}(r) + V_C(r) + V_{xc}(r) \tag{2.12}$$

with

$$V_{xc} = \frac{\delta E_{xc}}{\delta n} \tag{2.13}$$

is given as

$$H_{KS} = -\frac{1}{2}\nabla^2 + V_{KS}(r). \tag{2.14}$$

This gives rise to the Kohn-Sham Schrödinger-like equation

$$(H_{KS} - \varepsilon_i)\phi_i(r) = 0 \tag{2.15}$$

where ε_i are the eigenvalues of H_{KS}, and the orbitals satisfying above equation, ϕ_i, minimize the Kohn-Sham energy. This yields orbitals that reproduce the density of the original interacting system and the total energy, E_{KS}. These are independent particle equations with a potential that must be found self-consistently with the resulting density. In practice one starts with an initial guess for $n(r)$ and calculates the resulting $V_{KS}(r)$, and finally solves the Kohn-Sham Schrödinger-like equation for the ϕ_i. The orbitals yield a new density and the process is iteratively repeated until convergence.

2.2 Approximations for E_{xc}

2.2.1 Local Density Approximation (LDA)

In the Kohn-Sham approach [8], finding a good approximation for the exchange-correlation functional E_{xc} is the main challenge. Among many approaches, Local Density Approximation (LDA) has been the most commonly used. The LDA functional can be written as:

$$E_{xc}[n] = \int n(r)\epsilon_{xc}[n(r)]dr \tag{2.16}$$

where ϵ_{xc} is an energy per particle that depends only upon $n(r)$. Especially for a slowly varying $n(r)$ it is reasonable to assume that $\epsilon_{xc}[n(r)]$ is a functional of constant density $n(r) = n =$ constant. Then we need not find $\epsilon_{xc}[n(r)]$ for any shape of $n(r)$. Instead, it is enough to know $\epsilon_{xc}[n(r)]$ for a series of constant n. This is the idea behind the LDA.

2.2.2 Generalized Gradient Approximation (GGA)

An obvious way to improve on LDA is to take the gradients of the density into account. A first approach is systematic calculation of gradient corrections of the form $|\nabla n(r)|, |\nabla n(r)|^2, \nabla^2 n(r)$ etc. This is called the gradient expansion approximation (GEA), which gives worse results than LDA. It is realized that one could use more general functions of $n(r)$ and $\nabla n(r)$:

$$E_{xc}{}^{GGA}[n] = \int f(n(r), \nabla n(r)) dr \tag{2.17}$$

These are the GGA functionals and different GGA's differ in the choice of the function $f(n(r), \nabla n(r))$. Some very popular functionals go beyond GGA, and may even contain parameters optimized for certain class of molecules. One example is Becke three parameter Lee Yang Parr (B3LYP), very common in quantum chemistry.

Precisely, LDA uses the exchange-correlation density of the uniform electron gas assuming same charge density at every point in the system regardless of the inhomogeneity of the real charge density. The GGA uses the gradient of the charge density to correct for this deviation, and therefore thought to be more accurate.

2.2.3 Hybrid functionals

Hybrid functionals are a class of approximations to the exchange-correlation energy functional in density functional theory (DFT) that incorporate a portion of exact exchange from Hartree-Fock theory with exchange and correlation from ***Ab-initio*** or empirical. The hybrid approach to construct density functional approximations was introduced by Axel Becke in 1993 [9]. Hybridization with Hartree-Fock (exact) exchange provides a simple scheme for improving many molecular properties, such as atomization energies, bond lengths and vibration frequencies, which tend to be poorly described with simple ***Ab-initio*** functionals [10]. For example, the popular B3LYP (Becke, three-parameter, Lee-Yang-Parr)

[11, 12] exchange-correlation functional is:

$$E_{xc}{}^{B3LYP} = E_{xc}{}^{LDA} + a_0(E_x{}^{HF} - E_x{}^{LDA}) + a_x(E_x{}^{GGA} - E_x{}^{LDA}) + \\ a_c(E_c{}^{GGA} - E_c{}^{LDA}) \tag{2.18}$$

where a_0 =0.20, a_x =0.72 and a_c =0.81. B3P86 specifies the same functional with the non-local correlation provided by Perdew 86 [9].

2.3 Bloch's theorem and periodic boundary conditions

Condensed phases such as solids, liquids, amorphus materials, and systems of lower dimensionality such as surfaces or wires are macroscopic objects constituted by a huge number of atoms of the order of Avogadro's number (6x10^{23}/mol). In crystalline solids, a small number of atoms (a basis) is replicated periodically along one, two, or three directions in space. The unit or Wigner-Seitz cell, which is a minimal cell that contains the whole symmetry of the system, together with the lattice vectors contains all the necessary information to reproduce the infinite crystalline structure. Bloch's theorem [13] connects the properties of the electrons in a periodic infinite system with those of the electrons in the unit cell. The wave function of an electron in external periodic potential $v(r) = v(r + a_i)$ can be written as the product of a function with the same periodicity of the potential and a purely imaginary phase factor arising from the translational symmetry, i.e

$$\psi_k(r) = e^{ik.r} u_k(r) \tag{2.19}$$

with $u_k(r) = u_k(r + a_i)$, a_i with $i = 1, 2, 3$ are primitive vectors of unit cell. The wave function at location displaced by the unit vector, $r + a_i$ assumes the form

$$\psi_k(r + a_i) = e^{ik.a_i} \psi_k(r) \tag{2.20}$$

so that the probability density $|\psi(r)|^2$ is exactly the same because the purely imaginary phase factor cancels out.

For each a_i, there will be set of k vectors which satisfies $e^{ik.a_i} = 1$. The set three such smallest independent such vectors are called *reciprocal lattice vectors*. The primitive vectors in reciprocal space are defined by the relation $a_i.b_j = 2\pi\delta_{ij}$. We consider a system of non-interacting, free electrons in a one-dimensional periodic box of length a. The electronic wave functions are the solutions of the one dimensional Schrödinger equation

$$-\frac{\hbar^2}{2m}\frac{d^2\psi_k(x)}{dx^2} = \varepsilon(k)\psi_k(x) \tag{2.21}$$

The wave functions $\psi_k(x) = e^{ikx}$ are solutions of the above equation and the corresponding eigenvalues are

$$\varepsilon(k) = \frac{\hbar^2 k^2}{2m} \tag{2.22}$$

The relation between energy and wave vector is called *dispersion relation* and the allowed values of $\varepsilon(k)$-in this case all positive values-form the *energy bands*.

Bloch's theorem indicates that it is not necessary to determine the electronic wave functions everywhere in space. It is sufficient to know the solution in the unit cell. The wave function in the neighboring cell is exactly the same except for the phase factor $e^{ik.a}$.

2.4 Pseudopotentials

The wave functions for free electrons in a periodic crystal can be expanded in plane waves. The electrons in a solid (or atom or molecule) can be treated as core electrons and valence electrons. Core electrons are localized and tightly bound to the nuclei, while valence electrons are more extended. Most physical properties of materials depend on the valence electrons and much lesser than the core electrons. Since the valence electronic wave functions have to maintain orthogonality with the core electronic wave functions, the oscillation of the valence electronic wave function is rapid in the core region, the region near nuclei. When a plane wave basis set is chosen to expand the Kohn-Sham wave functions of all the electrons, an extremely large number of plane waves is required to accurately describe the deep potential near the nuclei and the rapid oscillations of the valence electronic wave functions in the core region. In practical calculations the pseudopotential approximation is used to avoid the direct consideration of the less important core electrons in the bonding process and the rapid oscillation of the valence wave functions in the core region. Specifically, in the pseudopotential scheme, core electrons are considered together with nuclei to form a new ionic potential and the strong ionic potential in the core region is replaced by a weaker screened pseudopotential that acts on a set of pseudo wave functions rather than the true valence wave functions. The use of the effective new pseudopotential to describe the electron-ion interaction leads to a reduction in the number of electrons that need to be described. Moreover many fewer plane waves are necessary to describe the much softer and smoother pseudo valence wave functions. Thus faster calculations can be performed or the treatment of bigger systems is possible under the pseudopotential approximation. Pseudopotentials replace the ionic potential with one that is smoother in the core region, but still reproduces the true valence charge density outside the core region. There are many pseudopotential schemes.

For instance, norm-conserving pseudopotentials are accurate and the condition of these pseudopotentials requires a relatively large number of plane waves (or large energy cutoff) for "semilocal" oribtals of elements because of their substantial fraction inside the core region and their importance to the bonding. While ultrasoft (for e.g. Vanderbilt's) pseudopotentials relax certain requirements and are faster than norm-conserving pseudopotentials , leading to a new pseudo wave function that can be expanded with a much smaller plane wave basis set. The charge deficiency due to the relaxation of the norm-conservation conditions are equilibrated by the introduction of atom-centered augmentation charges to ensure the proper density and potential. These augmentation of charges are defined as the charge difference between the all electron and pseudo wave functions, and for convenience they can be treated in a regular grid. Another closely related approach to Vanderbilt's pseudopotential scheme is the projector augmented wave (PAW) method introduced by Blöchl. In the PAW method, a linear transformation is defined to connect the all electron wave functions and pseudo wave functions, the total energy is derived in a consistent way by applying this transformation to the Kohn-Sham equations. In contrast to the pseudopotential method, the PAW method retains the all electron wave functions and potentials, avoids the introduction of a pseudopotential, and retains all the information on the core states. Ultrasoft, norm-conserving and PAW are all used in this thesis.

2.5 Dispersion correction for DFT

Hydrogen bonding and van der Waals (vdW) interactions are crucial for the formation and stability of molecular type crystals. Hybrid semi-empirical solutions are used to introduce damped atom-pairwise dispersion corrections of the form C_6R^{-6} in the DFT formalism. The missing dispersion contribution to the interatomic interaction is approximated by a simple isotropic potential. At long range, this potential is given by the $C_6^{ij}R_{ij}{}^{-6}$ term, where C_6^{ij} is a material-specific, so-called dispersion coefficient between any atom pair i and j at distance R_{ij}. At short range, the long-range expression is matched to the DFT potential by multiplication with a damping function $f(R_{ij}{}^0, R_{ij})$, which reduces the additional dispersion contribution to zero, subject to a cutoff defined by some suitably calculated combination $R_{ij}{}^0$ of the vdW radii of the atom pair. As C_6^{ij} coefficients are additive, the dispersion-corrected total energy E_{tot} may therefore be written as:

$$E_{tot} = E_{DFT} + S_i \sum_{i=1}^{N} \sum_{j>i}^{N} f(S_R R_{ij}{}^0, R_{ij}) C_{6,ij} R_{ij}{}^{-6} \tag{2.23}$$

where E_{DFT} is the standard DFT total energy. where N is the number of atoms, R_{ij} is the distance between ith and jth atom pairs, C_6^{ij} are pairwise dispersion coefficients, f_d is a damping function, and s_6 is a global scaling factor which depends on the density functional being used. Numerous types of damping functions were proposed to avoid the divergent behavior of the dispersion energy at short distances [20–24, 27]. The effect of a damping function [20] of the type

$$f_d = \frac{1}{1 + exp(-d(\frac{R}{R_{vdw}} + 1))} \tag{2.24}$$

The dispersion energy correction term is calculated separately from the DFT calculation. Since it is a long-range effect its influence on the electron densities should be small which allows a separate calculation for the correction. This method is general and can be combined with any exchange-correlation functional, with C_6 coefficients being determined either empirically [20, 21] D2 or ***Ab-initio*** methods [23–25]. Obtaining an accurate set of coefficients is of vital importance. Next, the discussions are towards the methods used in this thesis for dispersion correction namely, DFT–D(Grimme as well as TS) and vdW–DF.

In an earlier version of the DFT–D method, Wu et al [20] calculated empirical atomic C_6^{ij} coefficients by least squares fitting from experimental molecular C_6^{ij} coefficients obtained by using dipole oscillator strength distributions (DOSD's). Grimme [22, 23] initially used the C_6^{ij} coefficients from Wu et al [20] while averaging them over possible hybridization states (for the carbon atom). Later, in his less empirical DFT–D2 approach using DFT/PBE calculations of atomic ionization potentials (I_p^i) and static dipole polarizabilities (α^i) were computes the dispersion coefficient for an atom with the equation:

$$C_6^{ij} = 0.05NI_p^i\alpha^i \tag{2.25}$$

A geometric mean combination rule of the form shown below is used to get C_6^{ij} coefficients from atomic C_6^i and C_6^j coefficients. Grimme and coworkers solved these limitations with the newer DFT–D3 approach [23]. DFT-D3 method includes C_6 and C_8 terms for the two body dispersion correction has also an option for the three body dispersion correction.

$$C_6^{ij} = \sqrt{C_6^i C_6^j} \tag{2.26}$$

$$E_{disp} = \sum_{AB} \sum_{n=6,8} s_n \frac{C_n^{AB}}{r_n^{AB}} f_{d,n}(r_{AB}) \tag{2.27}$$

$$f_{d,n}(r_{AB}) = \frac{1}{1 + 6(r_{AB}(s_{r,n}R_0^{AB})^{-\alpha_n}} \tag{2.28}$$

The global scaling factor (s_n), which depends on the density functional used, is only adjusted for n $>$ 6 ($s_6 = 1$) to ensure the correct asymptotic behavior. This (s_8 to be precise) is the first parameter in DFT–D3 that is empirically determined for each different density functional. Along with this change, they have adopted the type of damping function (Eq. 2.28) initially used by Chai and Head–Gordon [27] which is more convenient for higher order dispersion correction. However, in a more recent paper [29] they have replaced this with the Becke–Johnson (BJ) type damping which gives finite dispersion energies at shorter distances rather than "zero" dispersion energy. They have noted that although the BJ damping is the primary choice, overall this only provides a slightly better (although more physically sound) energies for the tests they have performed [29]. In this thesis we have used the damping function as shown in Eq. 2.28 for the DFT–D3 calculations. The $s_{r,6}$ is the second parameter (since $s_{r,8}$ is set to be equal to 1) that is empirically determined by a least squares fit to a big data set of noncovalent interaction energies. The steepness parameters α_6 and α_8 were manually set to be 14 and 16, respectively.

Dispersion coefficients are calculated via ab–initio time–dependent (TD) DFT, where C_{6s} are calculated using the Casimir–Polder equation with averaged dipole polarizabilities at imaginary frequencies ($\alpha(i\omega)$). Here, $\alpha(i\omega)$ values were computed not for free atoms but using the stable hydrides of each element (except the rare gas atoms).

$$C_6^{AB} = \frac{3}{\pi} \int_0^\infty \alpha^A(i\omega)\alpha^B(i\omega)d\omega \tag{2.29}$$

Grimme et al. propose to account for the chemical environment dependence of the dispersion coefficients by using the number coordination number of the atoms.

For example, As the coordination number of an atom increases it can be thought of as being squeezed, hence the dispersion coefficient decreases. The reference C_6^{AB} coefficient calculated by the Casimir–Polder equation is adjusted by using the coordination number for the atom pair in the system of interest. Higher order C_8 terms are then obtained using recursion relations using the C_6 values. The accuracy of the molecular C_6 coefficients obtained theoretically can be tested using the experimentally known dipole oscillator strength distributions (DOSDs). The DFT–D3 method gives an 8.4 % mean absolute error for the accuracy of the molecular C_6 coefficients based on the DOSD data reported by Meath et al.

Two other dispersion correction schemes (Becke–Jonhson and Tkatchenko Sheffler) [24, 25] that depend on the chemical environment of the atoms were proposed before DFT–D3. Around an electron there is a depletion of density, which is named a exchange–correlation hole. The electron and its exchange hole has zero charge overall but a non–zero dipole moment. The Becke–Johnson model proposes a spherical shape of this exchange-correlation hole which generates a dipole moment as the source for the dispersion interaction. System dependent inter–atomic dispersion coefficients C_6^{ij} are obtained by using atomic polarizabilities and exchange(only)-hole dipole moment using the equation 2.30. The dispersion coefficients respond to chemical environment in two ways. One they are scaled using effective atomic volumes and secondly through the changes of the exchange–hole which affect the dipole moments that appear in equation 2.30. The molecular C_{6s} obtained using this method give 12.2 % mean absolute error (MAE) based on the data of Meath and co-workers [23]. One disadvantage of the BJ methods is that the computational cost is high (on the order of a hybrid DFT calculation) compared to other DFT–D methods [30].

$$C_6^{AB} = \frac{\alpha^A \alpha^B < d_x^2 >_A < d_x^2 >_B}{< d_x^2 >_A \alpha^B + < d_x^2 >_B < d_x^2 >_A} \tag{2.30}$$

Another method for computing nonempirical dispersion coefficients, which is sensitive to chemical environment of the atom, is the TS scheme of Tkatchenko and Scheffler [25]. In this procedure C_6^{ij} terms describing the vdW interaction between two atoms or molecules are computed using equation 2.26 which they obtained thorough a series of approximation starting with the Casimer–Polder integral (Eq. 2.31).

$$C_6^{AB} = \frac{2C_6^{AA} C_6^{BB}}{\frac{\alpha_0^B}{\alpha_0^A} C_6^{AA} + \frac{\alpha_0^A}{\alpha_0^B} C_6^{BB}} \tag{2.31}$$

The free–atom reference values of α_0^A and C_6^{AA} are taken from a self–interaction corrected TDDFT calculations of Chu and Delgarno[31]. They take the advantage of the relationship between the effective volume and polarizability to calculate dispersion coefficients that depend on the chemical environment of the atom. Hirshfeld partitioning [32] of the electron density of the system is used to obtain each atoms contribution to the density. This effective density, hence the volume, is compared to the density of the free–reference atom to obtain a scaling factor which is used to define the response of the dispersion coefficient's to chemical environment. The accuracy of the molecular C_6^{ij} coefficients obtained using the vdw–TS method with respect to the experimental values is the most accurate (5.4 % MAE) [25] compared to the ones discussed so far. Among the DFT–D methods discussed so far DFT–D3 of Grimme et al. and BJ method use higher order dispersion coefficients (at least the C_8^{ij}) when calculating the dispersion energy but vdW–TS includes only the leading C_6^{ij} term. The reason behind this is the assumption that shorter–ranged dispersion energy is included already when GGA functionals are used and some of it is also included artificially by the use of the damping function.

$$E^{ABC} = C_9^{ABC} \frac{3\cos\alpha\cos\beta\cos\gamma + 1}{(r_{AB} r_{BC} r_{AC})^3} \tag{2.32}$$

All of these (DFT–D3, vdW–TS and BJ) methods also have versions those provide description for dispersion energy beyond the two body pairwise methods [23, 33–35].

The other dispersion correction method used in the preset work is “vdW-DF”, a nonempirical nonlocal van der Waals functional and can capture dispersion interactions self-consistently. The main ingredient for the vdW–DF method is the inclusion of a long range non–local correlation energy functional of the form shown in equation

$$E_C^{non-local} = \int \int \rho(r)\Phi(r, r')\rho(r')drdr' \tag{2.33}$$

The nonlocal correlation functional ($E_C^{non-local}$) involves integration over the electronic densities at two points (r and r’) with the non–local kernel Φ(r,r’) relating the charge density, ρ, at r to that at r'. Promising solutions toward this non–local functional for vdW electron-electron correlation was initially given by the Rutgers-Chalmers collaboration [38, 40] The vdW–DF non–local functionals represent the exchange–correlation energy (E_{XC}) functional as,

$$E_{XC}[\rho] = E_X^{GGA} + E_X^{LDA} + E_C^{non-local} \tag{2.34}$$

where the first term on the right hand side of the equation is the exchange energy from a GGA functional, and the other two terms represent contributions from the short–range correlation energy from LDA and the long–range non–local correlation energy. The kernel Φ in equation 2.33 is a functional of the density and its gradient (vdW–DF2) where a local polarizability model is used to account for the dispersion interactions [38, 39, 41, 42]. Since the $E_C^{non-local}$ is constructed in a way that it vanishes at the uniform electron gas limit, there is no double counting when it is used with the local LDA correlation[41]. The original vdW–DF1 functional [38, 40] uses the revPBE exchange functional [43]. However since the revPBE exchange functional can bind spuriously by exchange alone and is too repulsive near equilibrium separation61 the newer versions of this method (such as vdw–DF2) use different exchange functionals such as PW86 [45] or optimized versions of PBE.

2.6 The GW approximation

The well known Green's function *G(x, x', t, t')*, is the fundamental quantity of many-body perturbation theory, which describes the probability of finding an electron with spin ξ at time *t* and position *r*, if another electron with spin ξ' is added (or removed) at position *r'* at time *t'*. It can be shown that the poles of the Green's function describe the energies needed to add/remove an electron from the system and that the imaginary part of the Green's function (Also known as spectral function) proportional to the photoemission spectrum. For a system of noninteracting electrons moving in the external potential *v(x)*, the energies to add or remove an electron are given by the eigen energies of

$$\begin{aligned}(T + v(x))\psi_n &= \epsilon_n \psi_n \\ Here T + v(x) &= H_0(x)\end{aligned} \tag{2.35}$$

with the kinetic energy operator T = -$(\hbar^2/2m)\nabla^2$, and the corresponding Green's function G$_H$ (Hartree Green's function) becomes

$$\begin{aligned}G_H^{-1}(x, x', \omega) &= \delta(x - x')[\omega - H_0] \\ G_H^{-1}(x, x, \omega) &= \sum_n \frac{\psi_n(x)\psi_n^*(x)}{\omega - \epsilon_n + i\eta sgn(\epsilon_n - \boldsymbol{\mu})}\end{aligned} \tag{2.36}$$

where η is a positive infinitesimal and μ is the Fermi energy of the system. The spectral function of a non-interacting system, therefore, consists of δ-like functions at the one-electron energies ϵ_n. For a system of interacting electrons, the perturbation caused by the addition or removal of an electron is screened and the sharp independent particle peaks in the spectral function are replaced by quasi-particle (QP) peaks with finite widths. The relation between the non-interacting Green's function G$_H$ and the Green's function of the interacting system G is given by the Dyson equation

$$G^{-1}(x, x', \omega) = G_H^{-1}(x, x', \omega) - \Sigma(x, x', \omega) \tag{2.37}$$

where the self-energy operator Σ includes the many-body effects due to exchange and correlation. The poles of the interacting Green's function can be found by solving the QP equation:

$$H_0(x)\psi_n^{QP}(x) + \int dx'\Sigma(x, x', E_n^{QP})\psi_n^{QP}(x') = E_n^{QP}\psi_n^{QP} \tag{2.38}$$

where the QP energies are complex quantities describing the position (Re (E$_n^{QP}$)) and width (IM$_n^{QP}$) of the QP peaks. The relation between the Green's function G, the self-energy Σ, the irreducible polarizability P, the screened Coulomb interaction W = $\epsilon^1 v$, and the so-called vertex function Γ, is given by Hedin's equations

[48, 49].

$$P(12) = -i \int d(34) G(13) G(41^+) \Gamma(342) \tag{2.39}$$

$$W(12) = v(12) + \int d(34) W(13) P(34) v(342) \tag{2.40}$$

$$\Sigma(12) = i \int d(34) G(14^+) W(13) \Gamma(423) \tag{2.41}$$

$$\Gamma(123) = \delta(12)\delta(23) + \int d(4567) \frac{\delta\Sigma(12)}{\delta G(45)} G(46) G(75) \Gamma(673) \tag{2.42}$$

$$\Gamma(12) = G_{KS}(12) + \int d(34) G_{KS}(13) \Sigma(34) G(42) \tag{2.43}$$

The Dyson equation for the relation between the interacting and non-interacting Green's function, Eq. 2.37, is thereby rephrased in Eq. ?? for the case that the KS-DFT system is taken as the reference system, as usually done in practical calculations. Hedin's equations should in principle be solved selfconsistently, but this is involved. The most common approximation to simplify this approach is the so-called GW approximation. The vertex corrections are thereby excluded which corresponds to setting $\Gamma(123) = \delta(12)\delta(13)$ in Eq. 2.43. Consequently, the irreducible polarizability (in eq. 2.40) is described by $P(12) = iG(12)G(21^+)$, which equals the RPA approximation and the neglect of electron-hole interactions. The self energy, finally, is approximated by

$$\Sigma(12) = iG(12^+) W(12) \tag{2.44}$$

explaining the name of the "GW" approximation.

2.6.1 Solving quasiparticle equation

The QP equations for a periodic crystal can be written as:

$$(T + v_{ext} + v_H \psi_{nk}^{QP}(r) + \int d^3r' \sum(r, r', E_{nk}^{QP}) \psi_{nk}^{QP}(r') = E_{nk}^{QP} \psi_{nk}^{QP}(r) \tag{2.45}$$

Normally, the wave functions are taken from a KS calculation (ψ_{nk} instead of ψ_{nk}^{QP}) and are not updated throughout the calculations. Self-consistency with respect to the wave functions can nevertheless be introduced (see the scQPGW method described in 50–52). Additionally, Eq. 2.45 is solved only on the real axis, i.e., imposing the constraint that E_{nk}^{QP} is real. If the DFT wave functions are considered, the quasiparticle energies equal the solution of

$$E_{nk}^{QP} = Re[< \psi_{nk}|T + v_{ext} + v_H + \Sigma(E_{nk}^{QP})|\psi_{nk} >] \tag{2.46}$$

An iterative solution to Eq. 2.46 can be found by

$$\begin{aligned} E_{nk}^{N+1} &= Re[< \psi_{nk}|T + v_{ext} + v_H + \Sigma(E_{nk}^{N+1})|\psi_{nk} >] = \\ & Re[< \psi_{nk}|T + v_{ext} + v_H + \Sigma(E_{nk}^{N})] + (E_{nk}^{N+1} - E_{nk}^{N}) \\ & \times Re[<< \psi_{nk}|\frac{\partial \Sigma(\omega)}{\partial \omega})_{\omega = E_{nk}^{N}}|\psi_{nk} >] \end{aligned} \tag{2.47}$$

i.e., by linearizing $\Sigma(\mathrm{E}_{nk}^{N+1})$ around $\Sigma(\mathrm{E}_{nk}^{N})$. The superscript QP has and will be omitted in the following. By introducing the normalization factor Z that accounts for the fact that the weights of the QP peaks are reduced at the cost of emerging satellites

$$Z_N^{nk} = (1 - Re[< \psi_{nk}|\frac{\partial \Sigma(\omega)}{\partial \omega})_{\omega = E_{nk}^{N}}|\psi_{nk} >])^{-1} \tag{2.48}$$

the QP energies can be approximated as

$$E_{nk}^{N+1} = E_{nk}^{N} + Z_{nk}^{N} Re[< \psi_{nk}|T + v_{ext} + v_H + \Sigma(E_{nk}^{N})|\psi_{nk} > - E_{nk}^{N}] \tag{2.49}$$

Several degrees of selfconsistency can be distinguished depending on how the expectation value of the self-energy operator ($\Sigma(\omega_{nk,nk}) = <\psi_{nk}|\Sigma(\mathrm{E}_{nk}^{N})|\psi_{nk}>$) is shown in below

$$\begin{aligned} &\frac{i}{2\pi V} \sum_{q,G,G'} \sum_{n'} 2 \int d\omega' W_q(G, G', \omega') < \psi_{nk}|e^{i(G+q)r}|\psi_{n'k+q} >< \psi_{n'k+q}|e^{-i(G'+q)r'}|\psi_{nk} > \\ &\quad (\frac{1}{\omega + \omega' - \epsilon_{n'k+q} + i\eta sgn[\epsilon_{n'k+q} - \boldsymbol{\mu}]} + \times \frac{1}{\omega - \omega' - \epsilon_{n'k+q} + i\eta sgn[\epsilon_{n'k+q} - \boldsymbol{\mu}]}) \end{aligned} \tag{2.50}$$

is calculated. In the most common approximation, G_0W_0, only one iteration step of Eq. 2.49 is performed and DFT eigenenergies are chosen as a starting point. The dielectric function for the evaluation of the screened Coulomb interaction W is calculated using DFT eigenvalues. In the GW_0 approximation, several circles of Eq. 2.49 are considered and the eigenvalues in Eq. 2.50 are approximated by E_{nk}^{N} of the previous iteration. The dielectric function ϵ, which enters the screened Coulomb kernel W, is thereby fixed at the DFT level. Finally, W in Eq. 2.50 can also be updated in each iteration. The GW calculations presented in part of this thesis have mostly been performed applying the G_0W_0 approximation. We have used the implementation of the G_0W_0 approximation [53, 54] provided by the code VASP(Vienna ***Ab-initio*** Simulation Package) [55].

References

[1] J. Kohan off, *Electronic structure calculations for solids and molecules: Theory and Computational Methods*, Cambridge University Press, Cambridge (2006).

[2] W. Koch and M.C. Holthausen, *A Chemist's Guide to Density Functional Theory*, Wiley Vch, New York (2002).

[3] R.G. Parr and W. Yang, *Density Functional Theory fo Atoms and Molecules*, Oxford University Press, Oxford (1989).

[4] M. Born and J. R. Oppenheimer, Am. J. Phys., **84**, 451 (1927).

[5] L. H. Thomas, Proc. Cambridge Phil. Soc, **23**, 542 (1927).

[6] E. Fermi, Z. Phys., **48**, 73 (1928).

[7] P. Hohenberg and W. Kohn, Phys. Rev., **136**, B864 (1964).

[8] W. Kohn and L. Sham, Phys. Rev., **140**, A1133 (1965).

[9] A. D. Becke, J. Chem. Phys., **98**, 1372 (1993).

[10] J. P. Perdew, M. Ernzerhof and K. Burke, J. Chem. Phys., **105**, 9982 (1999).

[11] K. Kim and K. D. Jordan, J. Phys. Chem., **98**, 10089 (1994).

[12] P. J. Stephens, F. J. Devlin, C. F. Chabalowski and M. J. Frisch, J. Phys. Chem., **98**, 11623 (1994).

[13] F. Bloch, Z. Phys., **52**, 555 (1928).

[14] M.L. Cohen and V. Heine, Solid State Physics, **24**, 37 (1970).

[15] M.T. Yin and M.L. Cohen, Phys. Rev. B, **25**, 7403 (1982).

[16] D. Vanderbilt, Phys. Rev. B, **41**, 7892 (1990).

[17] M. C. Payne, M. P. Teter, D. C. Allan, T. A. Arias and J. D. Joannopoulos, Rev. Mod. Phys., **64**, 1045 (1992).

[18] G. Kerker, J. Phys. C, **13**, 189 (1980).

[19] L. Kleinman and D. M. Bylander, Phys. Rev. Lett., **48**, 1425 (1982).

[20] Q. Wu and W. Yang, J. Chem. Phys., **116**, 515 (2002).

[21] S. Grimme, J. Comp. Chem., **25**, 1463 (2004).

[22] S. Grimme, J. Comp. Chem., **27**, 1787 (2006).

[23] S. Grimme, J. Antony, S. Ehrlich and H. Krieg, J. Chem. Phys., **132**, 154104 (2010).

[24] E. R. Johnson and A. D. Becke, J. Chem. Phys., **127**, 154108 (2007).

[25] A. Tkatchenko and M. Scheffler, Phys. Rev. Lett., **102**, 073005 (2009).

[26] J. Hepburn, G. Scoles and R. Penco, Chem. Phys. Lett., **36**, 451 (1975).

[27] J. -D. Chai and M. H. -Gordon, Phys. Chem. Chem. Phys., **10**, 6615 (2008).

[28] C. Adamo and V. Barone, J. Chem. Phys., **110**, 6158 (1999).

[29] S. Grimme, S. Ehrlich and L. Goerigk, J. Comp. Chem., **32**, 1456 (2011).

[30] L. A. Burns, A. V. Mayagoitia, B. G. Sumpter and C. D. Sherrill, J. Chem. Phys., **134**, 084107 (2011).

[31] X. Chu and A. Dalgarno, J. Chem. Phys., **121**, 4083 (2004).

[32] F. L. Hirshfeld, Theo.Chim. Acta., **44**, 129 (1977).

[33] A. O. -d. -l. Roza and E. R. Johnson, J. Chem. Phys., **138**, 054103 (2013).

[34] O. A. v. Lilienfeld and A. Tkatchenko, J. Chem. Phys., **132**, 234109 (2010).

[35] A. Tkatchenko, R. A. DiStasio, R. Car and M. Scheffler, Phys. Rev. Lett., **108**, 236402 (2012).

[36] T. Risthaus and S. Grimme, J. Chem. The.Compu., **9**, 1580 (2013).

[37] A. M. Reilly and A. Tkatchenko, J. Phys. Chem. Lett., **4**, 1028 (2013).

[38] M. Dion, H. Rydberg, E. Schröder, D. C. Langreth and B. I. Lundqvist, Phys. Rev. Lett., **92**, 246401 (2004).

[39] K. Lee, E. D. Murray, L. Kong, B. I. Lundqvist and D. C. Langreth, Phys. Rev. B, **82**, 081101 (2010).

[40] T. Thonhauser, V. R. Cooper, S. Li, A. Puzder, P. Hyldgaard and D. C. Langreth, Phys. Rev. B, **76**, 125112 (2007).

[41] O. A. Vydrov and T. V. Voorhis, Phys. Rev. A, **81**, 062708 (2010).

[42] J. F. Dobson and T. Gould, J. Phys.:Cond. Matt., **24**, 073201 (2012).

[43] Y. Zhang and W. Yang, Phys. Rev. Lett., **80**, 890 (1998).

[44] A. Puzder, M. Dion and D. C. Langreth, J. Chem. Phys., **124**, 164105 (2006).

[45] J. P. Perdew and W. Yue, Phys. Rev. B, **33**, 8800 (1986).

[46] G. R.-Perez and J. M. Soler, Phys. Rev. Lett., **103**, 096102 (2009).

[47] P. L. Silvestrelli, K. Benyahia, S. Grubisic, F. Ancilotto and F. Toigo, J. Chem. Phys., **130**, 074702 (2009).

[48] L. Hedin, Phys. Rev., **139** A796 (1965).

[49] L. Hedin and S. Lundquist, Solid State Physics, edited by H. Ehrenreich, F. Seitz, and D. Turnbull, vol 23, Academic, New York (1969).

[50] S.V. Faleev, M. van Schilfgaarde, T. Kotani, Phys. Rev. Lett. **93**, 126406 (2004).

[51] M. van Schilfgaarde, T. Kotani, S.V. Faleev, Phys. Rev. Lett. **96**, 226402 (2006).

[52] M. Shishkin and G. Kresse, Phys. Rev. Lett. **99**, 246403 (2007).

[53] S. Lebègue, B. Arnaud, M. Alouani and P. E. Blöchl, Phys. Rev. B, **67**, 155208 (2003).

[54] S. Lebègue, B. Arnaud, and M. Alouani, Phys. Rev. B, **72**, 085103 (2005).

[55] G. Kresse and J. Furthmuller, Phys. Rev. B, **54**, 11169 (1996).

Chapter 3

Role of dispersion corrected DFT methods on structural, elastic, and vibrational properties of black phosphorus

In this chapter, results are presented for ***layered black phosphorus***, where the dispersion interactions are more predominant between layers. The present example provides a good primer for more complicated systems to quantify the effect of weak dispersion interactions on basic ground state properties. In addition to that, various dispersion correction methods along with standard Density functional theory (DFT) functionals were also tested to understand the improvement on structure- related properties.

3.1 Introduction

Phosphorus, belongs to the group 5A of the Periodic Table, exists in different allotropic modifications including white, black and amorphous red at ambient conditions [1]. Among these allotropic forms black phosphorus is the most stable one [2], crystallizes in an orthorhombic structure [4] and a direct narrow band gap semiconductor [3]. Recent experiments and theoretical measurements reported that few layers (mono, bi) of black phosphorus could be an interesting Quasi 2D material, similar to graphene, boron-nitrides , and transition metal-chalcogenides. The electronic properties of 2D phosphorous highly depend on the inter-layer interactions and its thickness. For e.g. enhancement of band gap (0.3 to 1.5 eV)

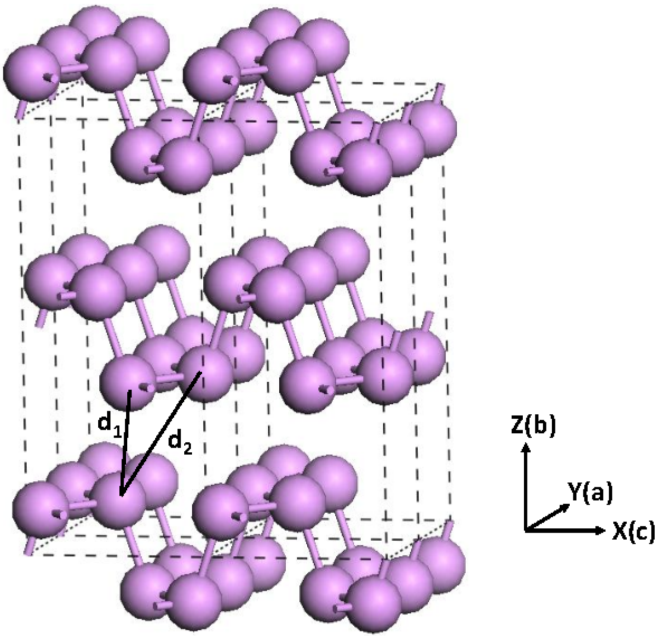

Figure 3.1: Crystal structure of black phosphorus. Here d_1 and d_2 are the nearest and next-nearest interlayer atomic distances.

was observed from bulk phosphorus to multi-layer phosphorus, which shows promising nanoelectronic applications .

Experimental reports at high pressures found that, orthorhombic black phosphorus transforms to a rhombohedral structure around 5 GPa and further on to a simple cubic structure at 10 GPa [5–9] which is quite stable up to megabar pressures. At very high pressures of 137 GPa and 262 GPa, further structural phase transitions (such as simple hexagonal and body centered cubic respectively) have been reported using x-ray diffraction [10, 11]. The physical properties of black phosphorus such as, anisotropic electrical resistivity, optical reflectance, photoemission spectra, infrared absorption spectra, and phonon dispersions were reported by various experimental measurements [3, 12–16].

On the theoretical side, investigations of the electronic structure [17–19] using the linear muffin tin orbital (LMTO) method [20], and optical properties using the self consistent pseudopotential method were published [2, 21]. Lattice dynamical properties of black phosphorus including phonon dispersion relations, were obtained [22] using a valence force field method. A number of papers discussed the high-pressure behavior of black phosphorus, notably the structural stability and the electronic structure [19, 23–31]. Du et al [32] performed calculations for single layered and bulk black phosphorus and reported that black phosphorus might be used as anode material for lithium ion batteries.

Apart from above all , black phosphorus has a layered structure where each phosphorus atom is covalently bonded with three neighboring phosphorus atoms in the same layer, the layers being weakly coupled by van der Waals (vdW) forces. At ambient conditions black phosphorus crystallizes in a base centered orthorhombic structure (see Fig. 1) with the space group of *Cmca* (no. 64). The experimental lattice parameters [4] are a=3.31 , b= 10.47, and c=4.37 Å. The crystal structure consists of puckered layers of P atoms with three short covalent bonds (two at 2.22, and one at 2.28 Å), with vdW bonding along the b-axis, with the vertical distance between layers being 3.27 Å. The orthorhombic unit cell contains 8 phosphorus atoms in the crystallographic (8f) positions [4] $(0, u, v)$. The nearest and next-nearest atomic separations between the layers (d_1 and d_2 in Fig. 1) are 3.6 Å and 3.8 Å. These structural details clearly emphasize the necessity to include the vdW interactions in the theoretical calculations of ground state structural properties of this system to ensure accurate description of experimental results.

The main focus of the present chapter is to calculate the ground state structural, elastic and dynamical properties of black phosphorus and to compare several schemes for inclusion of vdW interactions.

3.2 Computational details

The calculations in this chapter were performed using the Cambridge Series of Total Energy Package (CASTEP) [34, 35] code based on DFT using Vanderbilt-type ultra soft pseudo potentials [36] for the electron-ion interactions. The exchange-correlational potential of Ceperley and Alder [37] as parameterized by Perdew and Zunger (CAPZ) in LDA [38], and the GGA schemes of Perdew and Wang (PW91) [39] and of Perdew-Burke-Ernzerhof (PBE) [40] were used. Dispersion corrected density functional theory (DFT-D) approaches to treat vdW interactions were employed, notably Ortmann, Bechstedt and Schmidt (OBS) [41] correction to PW91, as well as Tkatchenko and Scheffler (TS) [42] and D2 [33] corrections to PBE. To perform our calculations, a plane wave cut-off energy of 520 eV is used and the first Brillouin zone of the unit cell is sampled according to the Monkhorst-Pack scheme [48] by means of a (9x6x8) k-point sampling. The Pulay [49] density mixing scheme was applied for the electron energy minimization process. During the structural optimization process iterations were continued until the change in total energy was less than $5e-6$ eV/atom, and the maximum displacement of atoms was also less than $5e-5$ Å. The elastic constants are calculated using the volume-conserving strain technique as implemented in the CASTEP code [50, 51].

3.3 Results and discussions

3.3.1 Structural properties

The theoretical equilibrium crystal structure was obtained by performing full structural optimization including lattice constants and the internal coordinates u and v, using LDA, GGA, and the three dispersion-corrected GGA (GGA-D) methods as mentioned in above section. The calculated structural parameters are presented in Table 3.1. Taking the experimental ambient volume as reference, the observed difference between calculated and experimental volume of -11 % with LDA, +8 % with PW91, and +10 % with PBE. The large errors reflect that none of these approximations to the exchange-correlation potential are able to capture the nature of the vdW interactions correctly in black phosphorus. The DFT-D schemes perform much better (see Table 3.1), the errors in predicted equilibrium volumes being only +1.5 %, +2.9 %, and -0.3 %, respectively, for the PW91-OBS, PBE-TS, and -D2 parametrizations. Considering the three lattice parameters, it is clear that the largest error is found for the b-parameter, the characteristic dimension in the Z direction, i.e., perpendicular to the covalent P layers. Thus, the interlayer interaction is dominated by dispersive forces (vdW), and an accurate description of this type of interaction is important. Comparison of the data for

Table 3.1: The calculated ground state properties of orthorhombic black phosphorus at ambient pressure. ***a***, ***b*** and ***c*** are the lattice parameters, *V* the volume of the orthorhombic unit cell, and *u* and *v* the internal crystallographic parameters.

Method	XC	a(Å)	b(Å)	c(Å)	V(Å^3)	u	v
DFT	LDA	3.28	10.10	4.07	134.9	0.1059	0.0711
	LDA-HL[a]	3.24	10.19	4.24	140.0	0.1013	0.0789
	PW91	3.29	11.07	4.52	164.5	0.0950	0.0871
	PBE	3.28	11.22	4.54	167.1	0.0935	0.0876
GGA-D	PW91-OBS	3.29	10.63	4.41	154.1	0.0996	0.0832
	PBE-TS	3.29	10.82	4.39	156.3	0.0979	0.0830
	PBE-D2	3.30	10.43	4.40	151.3	0.1017	0.0833
Exp[b]		3.3133	10.473	4.374	151.77	0.1034	0.0806

a : Ref. [19], *b* : Ref. [4].

PBE and PBE-D2 in Table 3.1 shows that the inclusion of vdW interaction reduces the ***c***-parameter by $\sim$ 3 %, whereas the ***b***-parameter is reduced by $\sim$ 7 %. On the other hand, the internal parameters *u* and *v* are about equally well predicted by all functionals considered, probably because these parameters are determined by the P-P covalent bonds, which are usually well described by LDA and GGA. The overall best agreement with experimental parameters is achieved with the PBE-D2 functional. The present LDA calculations are in reasonable agreement with the earlier LDA-HL [19] calculations (see Table 1.1). The minor differences are most likely due to the different parametrizations of the LDA functional used and to the different basis sets (plane waves in the present work versus full potential LMTO in Ref [19]).

To investigate the response of black phosphorus to external pressure, hydrostatic compression was applied to the unit cell in the pressure range of 0 to 5 GPa in steps of 0.5 GPa. This was done by variable cell optimization under the constraint of a diagonal stress tensor with values of the diagonal elements fixed to specify the desired pressure. The change in the lattice parameters ***a***, ***b*** and ***c*** with pressure is compared with the experimental values [55] and shown in Fig. 3.2. It is seen that the ***a*** lattice parameter shows only a weak variation under pressure, which reflects strong bonding along this direction. This fact is correctly captured by all the functionals used in this present chapter, although we obtain a larger

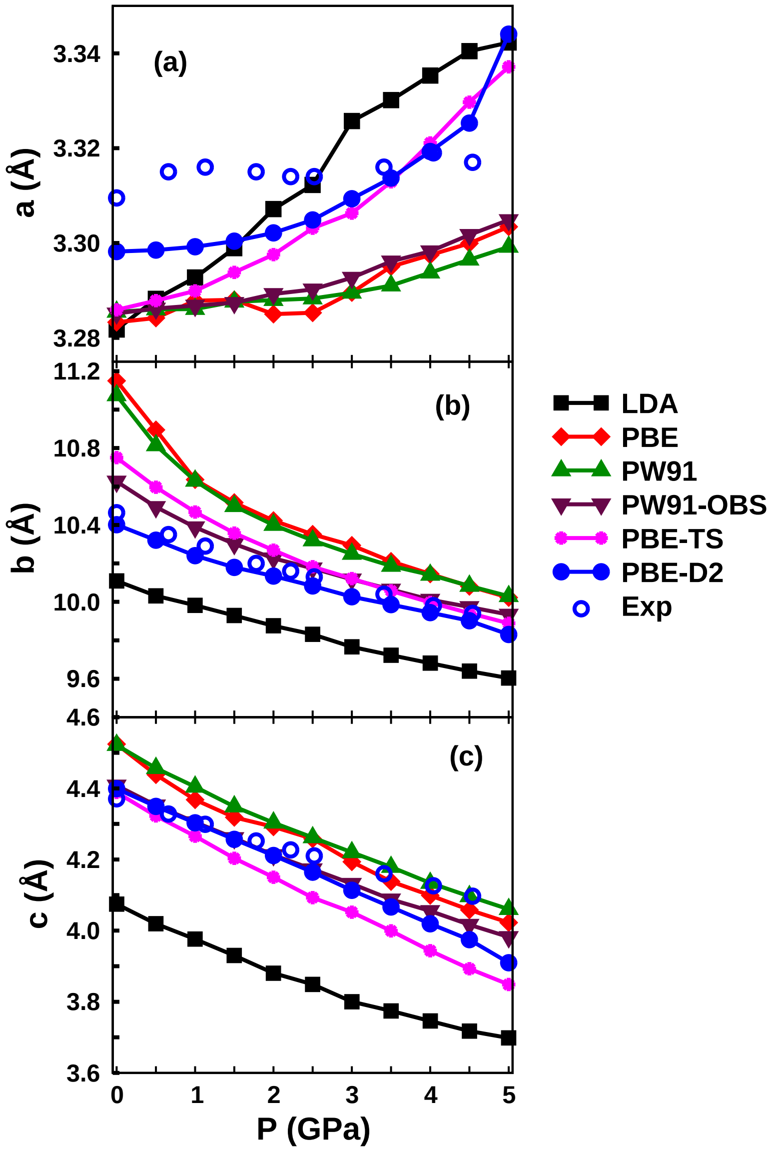

Figure 3.2: (a)-(c) Pressure dependence of lattice parameters *a*, *b* and *c* up to 5 GPa within LDA, GGA and GGA-D, compared to experimental values (Ref. [55]). Note the different scales on the vertical axes, in particular the small scale in (a).

Table 3.2: The calculated first order pressure coefficients of the lattice parameters (Eq. (3.1)) of orthorhombic black phosphorus, using LDA-CAPZ as well as GGA with and without dispersive corrections (see caption of Table 1.1). The experimental results are taken from Ref. [4]. Units are 10^{-3}Å·GPa^{-1}.

	DFT			DFT-D			Expt.
axis	LDA	PW91	PBE	PW91-OBS	PBE-TS	PBE-D2	
a	11	~ 1	2	3	2	~ 0	~ 0
b	-123	-460	-566	-261	-411	-124	-125
c	-101	-125	-135	-118	-147	-82	-55

variation than in the experiments. In fact all functionals predict slight increase in ***a*** lattice parameter with pressure. The variation is much larger for ***b*** and ***c***. For the ***b*** parameter, a reduction of $\sim$ 0.52 Å is observed experimentally over the pressure range of 0-4.5 GPa [55]. This is correctly reproduced when the vdW correction is included, but it appears as about twice with the standard PW91 and PBE functionals. As for the ***c*** parameter, experimentally a reduction by approximately 0.27 Å is seen in this pressure range (Fig. 1.2(c)) and this variation is overestimated by all methods tested, even those corrected for vdW interactions. These results are also quantified in terms of the pressure coefficients defined as (with x being either ***a***, ***b***, or ***c***)

$$\gamma(x) = \left.\frac{dx}{dP}\right|_{P=0} \tag{3.1}$$

which are shown in Table 3.2. The pressure coefficient for the lattice parameter ***a*** is very small for all approximations, in accordance with the experimental data [4]. For the lattice parameter ***b***, the pressure coefficient varies significantly between different approximations, but comes very close to the experimental value with D2's corrected functional. The magnitude of the pressure coefficient for the parameter ***c*** is roughly twice as large as found experimentally using PBE, with the best agreement found again with D2's method.

The calculated pressure-volume P(V) relation of black phosphorus is shown in Fig. 3.3 and compared with experimental results [55]. Apart from the offset in equilibrium volumes discussed above, it is noticeable that both the GGA

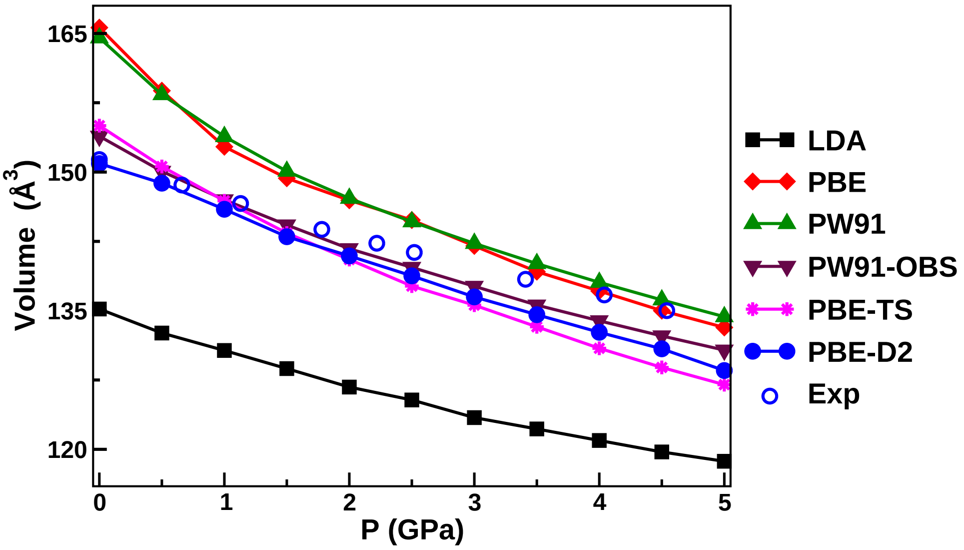

Figure 3.3: Comparison of the pressure dependence of the crystal volume as calculated within LDA, GGA and GGA-D, compared to experimental volumes (Ref. [55]).

and GGA-D calculations find black phosphorus to be more compressible than reported experimental values. The slopes of the calculated $V(P)$ relations at $P = 0$ are larger than seen in experiments [55], with the exception of the D2 approach. This implies that the bulk moduli calculated with these approaches are significantly smaller than the experimental value. For the D2 functional the initial slope is very similar to the experimental value, and the calculated bulk modulus within the D2 approach is $B = 31.3$ GPa, which is in good agreement with experimental values of 32.5 GPa [4] and 36 GPa [55]. Therefore, comparing all the theoretical approaches applied here for black phosphorus, D2's functional, shows overall best agreement, and it is noticeable that the dispersion correction provided by the D2 functional has the right magnitude at low pressure, but seems to be slightly too strong for elevated pressures. However, one should consider in mind that the experiments under pressure are performed at room temperature, whereas theory pertains to $T = 0$. The variation of the internal coordinates u and v under pressure are illustrated in Fig. 3.4. All functionals capture the increasing (decreasing) trends of $u(P)$, ($v(P)$) as found in the experiment [55]. Clearly, the LDA shows poorest agreement with the experimental data, and the vdW corrected GGA show

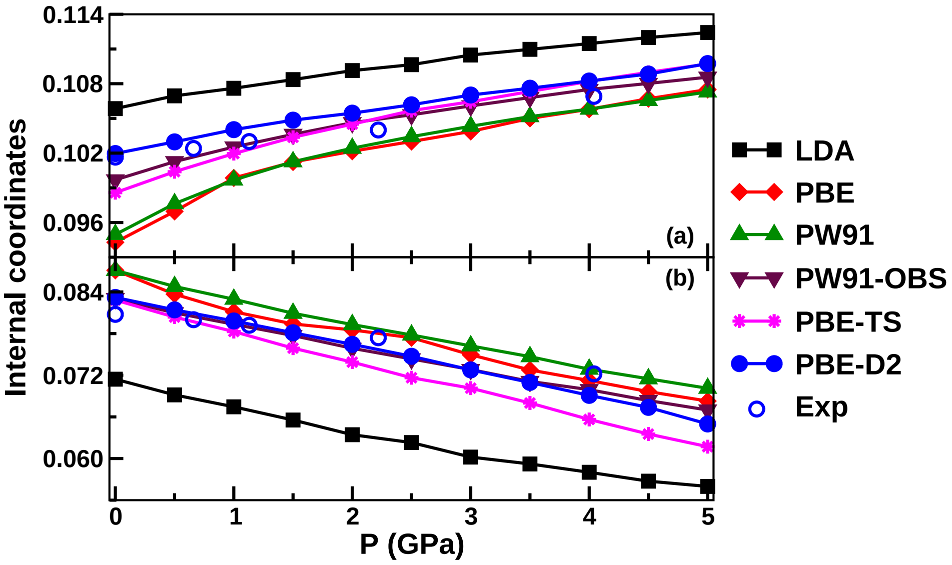

Figure 3.4: Internal coordinates, (a). *u* and (b). *v* , of black phosphorus up to 5 GPa as calculated within LDA, GGA and GGA-D, together with experimental values (Ref. [55]).

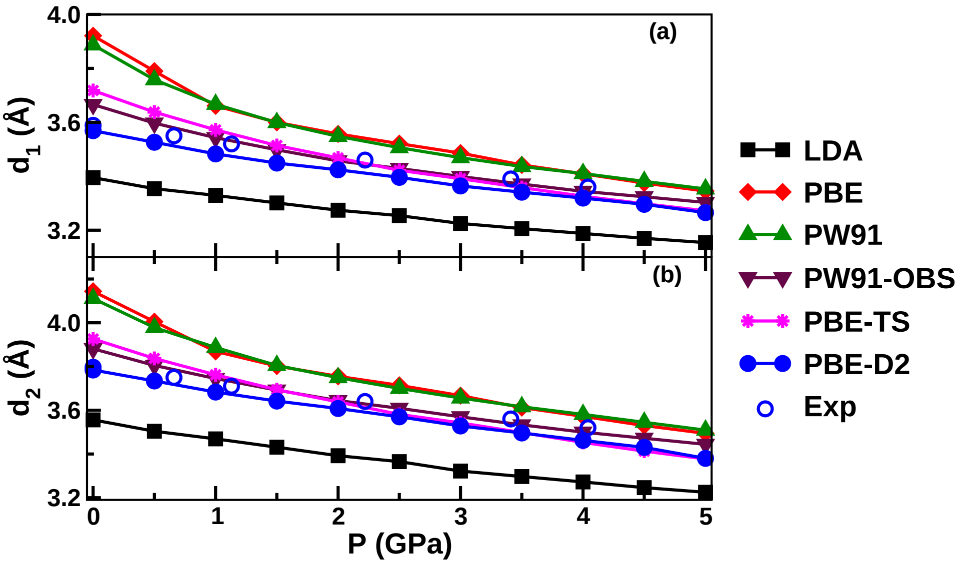

Figure 3.5: Calculated (a): nearest neighbour (d_1) and (b): next-nearest neighbor (d_2) interlayer atomic separations (see. Fig. 1) of black phosphorus up to 5 GPa within LDA, GGA and GGA-D, compared with experimental values (Ref. [55]).

marginally better agreement with experiments than the pure GGA functionals. Also, Fig. 3.5 illustrates the pressure dependence of the nearest and next nearest interlayer atomic distances, d_1 and d_2 in Fig. 3.1. It is seen that LDA grossly underestimates and the pure GGA functionals overestimate these parameters. For the vdW corrected functionals, the agreement with experiments is much better, and the pressure evolution of the interlayer atomic distances is best reproduced with the D2 functional. This is of course in line with the better agreement found for the equilibrium volume and the other properties under pressure.

3.3.2 Elastic properties

Elastic constants are fundamental mechanical properties for crystalline materials and describe the stiffness of the material against externally applied strains. The calculations were performed for single crystal elastic properties for black phosphorus within the GGA and vdW-corrected GGA approximations. In the orthorhombic crystal structure there are nine independent elastic constants: C_{11}, C_{22}, C_{33}, C_{44}, C_{55}, C_{66}, C_{12}, C_{13}, C_{23}. Here, we follow the conventions of the experimental papers [52, 53] in which the indices $1, 2, 3$ are defined to correspond to the crystallographic directions X, Y, Z ($\boldsymbol{c}$,$\boldsymbol{a}$,$\boldsymbol{b}$), respectively, as indicated in Fig. 1. To calculate the elastic constants, the equilibrium crystal structure is deformed by the appropriate strain and the variation in total energy gives the elastic constants. The calculated elastic constants are presented in Table 1.3. All the calculated elastic constants satisfy Born's mechanical stability criteria [56] implying that the system is mechanically stable at ambient pressure. The experimental elastic constants have been determined for black phosphorus in Refs. [52, 53] by ultrasound velocity measurements. Following the convention of these works, the C_{11}, C_{22}, and C_{33} elastic constants directly relate to sound propagation along the crystallographic $\boldsymbol{c}$, $\boldsymbol{a}$, and $\boldsymbol{b}$-axes, respectively, and reflect the stiffness to uniaxial strains along these directions [51]. The reported experimental values are scattered over a range of values, which probably reflects the difficulty of the measurements. Also, the elastic constants show some variation with temperature, as discussed in Ref. 53.

Table 3.3: Single-crystal elastic constants (C_{ij}, in GPa) and bulk modulus (B in GPa) of black phosphorus. All quantities are calculated at the respective theoretical equilibrium volumes using the various GGA and GGA-D functionals.

	DFT		DFT-D			
	PW91	PBE	PW91-OBS	PBE-TS	PBE-D2	Exp
C_{11}	45.2	40.7	44.4	36.8	52.3	55.1^a, 80^b
C_{22}	186.7	183.4	192.4	185.9	191.9	178.6^a, 284^b
C_{33}	19.2	13.0	40.5	30.6	73.0	53.6^a, 57^b
C_{44}	10.3	8.6	15.9	31.2	25.5	21.3^a, 11.1^a, 17.2^b
C_{55}	4.2	2.6	5.6	23.4	8.8	5.5^a, 10.8^b
C_{66}	48.3	48.5	57.3	57.4	63.6	14.5^a, 15.6^a, 59.4^b
C_{12}	32.3	30.0	35.6	31.5	40.8	—
C_{13}	-4.3	-4.6	-5.3	-0.9	0.6	—
C_{23}	1.0	-1.6	1.5	-0.6	8.3	—
B	11.6	8.1	18.6	16.2	30.7	32.5^c, 36^d

a: Ref. [52] (at room temperature); b: As read from figures of Ref. [53] (at T=0 K); c: Ref. [4]; d: From *PV*-data of Ref. [55].

From Table 1.3, it is seen that the calculated elastic constants show some variations when evaluated with different functionals, which is a combined effect of the different effective forces and equilibrium structures obtained with the various functionals such as DFT and +D correction methods. The C_{22} elastic constant is significantly larger than C_{11} and C_{33}. This shows that the material is stiffer for strains along the ***a***-axis than the ***b***- and ***c***-axes, consistent with the results shown in Fig. 3.2, which again can be attributed to the strong covalent bonds between P atoms along the crystallographic ***a***-axis. For C_{22}, the calculated values are consistent between the different functionals and is in excellent agreement with the experimental value reported by Kozuki et al [52], on the other hand significantly larger by other experimental value (see Ref. 53). The C_{11} is relatively constant among the considered functionals and again in fair agreement with the experimental value of Kozuki et al [52], whereas the value is larger by other reported experimental value (see Ref. 53). The C_{33} describes stiffness to stress along the ***b***-axis, and this has a small value when evaluated in pure GGA, whereas the vdW-corrected methods give larger values, for the OBS and TS flavors in reasonable agreement with the experimental values, whereas the D2 approach significantly

Table 3.4: Calculated values of the polycrystalline bulk (B_X) and shear moduli (G_X) in the Voigt, Reuss and Hill approximations ($X = V, R, H$, respectively). Units are GPa. Also listed are the Young's modulus, E (in GPa), Poisson's ratio, σ, and the shear anisotropy factors, A_i. All values are calculated at the theoretical equilibrium volume using the PBE-D2 functional.

B_V	B_R	B_H	G_V	G_R	G_H	E	σ	A_1	A_2	A_3
46.3	30.7	38.5	37.4	21.4	29.4	70.3	0.30	0.8	0.1	1.6

overestimates this parameter. The C_{44} and C_{55} constants are relatively small and in good agreement between theory and experiment (although the value of C_{55} calculated with PBE-TS stands out as too large). On the other hand, for C_{66} the calculated values are fairly consistent and is in good agreement with the experimental value of Ref. [53], whereas the measured value reported by Ref. [52] is a factor 3 to 4 smaller. Among the off-diagonal elastic constants, C_{12} is large and relatively consistent between the various functionals, whereas, the C_{13} and C_{23} are small, and in some cases take negative values. It is to be noted that there are no reported experimental values of C_{12}, C_{13} and C_{23} . From the single crystal elastic constants the single-crystal bulk modulus B can be calculated [51] and the obtained bulk modulus value of $B = 30.7$ GPa (using the D2 functional) is in good agreement with the experimental values of $B = 32.5$ GPa [4] or $B = 36$ GPa [55], as well as with the value derived from the $V(P)$ relation in Fig. 3.3, $B = 31.3$ GPa (also in the D2 approximation). Altogether, the agreement between the measured and the calculated elastic constants is fair while not perfect.

The bulk and shear moduli of polycrystalline black phosphorus may be obtained from the elastic constants using the Voigt-Reuss-Hill approximations [57–59]. Here, the Voigt and Reuss approximations represent extreme values, and Hill recommended that their average is used in practice for polycrystalline samples. Their definitions for orthorhombic systems are given in Ref. 51 and their values for black phosphorus are quoted in Table 1.4. Using the calculated bulk and shear moduli in the Hill approximation, B_H and G_H, we have evaluated the Young's modulus, E, and Poisson's ratio, σ. Young's modulus reflects the resistance of a material towards uniaxial tensions, whereas, Poisson's ratio gives information about the stability against shear strain. The results obtained are summarized in

Table 1.4. It is seen that, for polycrystalline black phosphorus, $B_H > G_H$, which implies that the parameter limiting the mechanical stability of black phosphorus is the shear modulus G_H. The bulk and shear moduli provides information about the brittle-ductile nature of materials through Pugh's ratio. [60] According to Pugh, a B_H/G_H ratio below (above) 1.75 indicates the *brittle* (*ductile*) nature of the material. For black phosphorus the calculated value is $B_H/G_H = 1.31$, i. e. indicating a brittle nature of the material. Generally, Poisson's ratio is connected with the volume change of a material during uniaxial deformation and the nature of interatomic forces. If σ is 0.5, no volume change occurs, whereas, lower than 0.5 means that large volume change is associated with elastic deformation [51]. In our calculation $\sigma = 0.30$ is obtained, which shows that a considerable volume change can be associated with the deformation in black phosphorus. The anisotropy in bonding between atoms in different planes is related to an anisotropic thermal expansion. This anisotropy plays an important role for all orthorhombic systems, as they influence the durability of the material to repeated heating cycles. The shear anisotropy factors measure this effect in terms of the elastic constants (see definitions for orthorhombic crystals in Ref. 51, 61). If the anisotropy factor is unity it represents complete elastic isotropy, whereas values smaller or greater than unity measure the degree of elastic anisotropy. For black phosphorus the calculated shear anisotropy factors A_1 is close to unity, which shows that the resistance to shears of $\langle 100 \rangle$ planes (i.e. planes having $\boldsymbol{c}$ as a normal) along the $\boldsymbol{a}$ and $\boldsymbol{b}$ directions are approximately equally. In contrast, the A_2 and A_3 anisotropy factors are very different from unity, implying that shears of planes orthogonal to $\boldsymbol{a}$ and of planes orthogonal to $\boldsymbol{b}$ both behave very anisotropically.

3.3.3 Optical Phonons

The optical phonons of black phosphorus have been obtained by the linear response method within density functional perturbation theory [67]. In this method the force-constant matrix is obtained by differentiation of the Hellmann Feynman forces on atoms with respect to the ionic coordinates. In order to understand the optical phonons of black phosphorus, it is necessary to first consider the dynami-

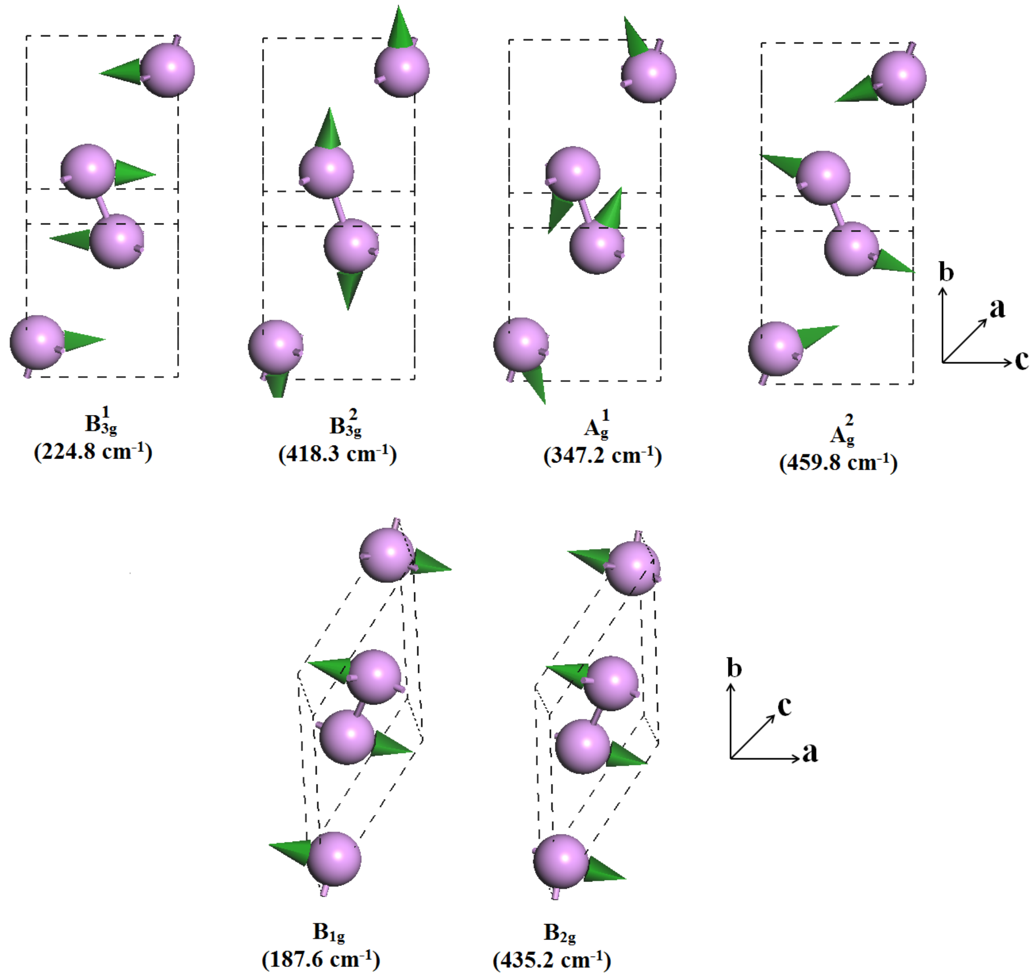

Figure 3.6: Snapshots of Raman active modes for primitive black phosphorus. The listed frequencies are as calculated within GGA-D2 at P = 0.

cal properties of this structure. The primitive cell contains four atoms leading to 12 vibrational modes, i. e. 9 optical and 3 acoustic phonons branches. From the group-theoretical analysis of the *Cmca* space group, the irreducible representation at the Brillouin zone center is

$$\Gamma_{acoustic} = B_{1u} + B_{2u} + B_{3u}$$

and

$$\Gamma_{optical} = B_{1u} + B_{2u} + A_u + 2A_g + B_{1g} + B_{2g} + 2B_{3g}$$

All the optical phonons are Raman active except the B_{1u} and B_{2u} modes, which are infrared active, and the A_u mode, which is silent. The optical phonons of black phosphorus were investigated by Sugai and Shirotani [68] and by Akahama et al [26]. The Raman frequencies turn out to be relatively insensitive to the details of the functional employed, for which reason we show the results obtained using the GGA-D2 fuctional. This is probably a reflection of the fact that the optical phonons are described by near-neighbour interatomic forces, which are dominated by covalent interactions, which are generally well accounted by the LDA. The eigenvectors of the Raman modes, as calculated at ambient pressure within the GGA-D2 approach are illustrated in Fig. 3.6, which are in good agreement with earlier work [26, 68]. From the calculated Raman eigenmodes, the A_g^1 , A_g^2 and B_{3g}^2 modes are seen to constitute inter-layer vibrations with a strong component along the ***b*** direction. In the modes B_{1g} and B_{2g} the atoms move along the ***a*** direction, whereas, in the B_{3g}^1 mode the atoms move along the ***c*** direction. In Fig. 3.7 the calculated Raman frequencies under pressure up to 5 GPa are compared with the available experimental results [26]. The agreement between theory and experiment is excellent. The strongest pressure dependence is seen for the inter-layer A_g^1 mode, for which the pressure coefficient is $d\omega/dP = 8.2$ cm^{-1}/GPa in theory, and $d\omega/dP = 5.78$ cm^{-1}/GPa according to experiment [26].

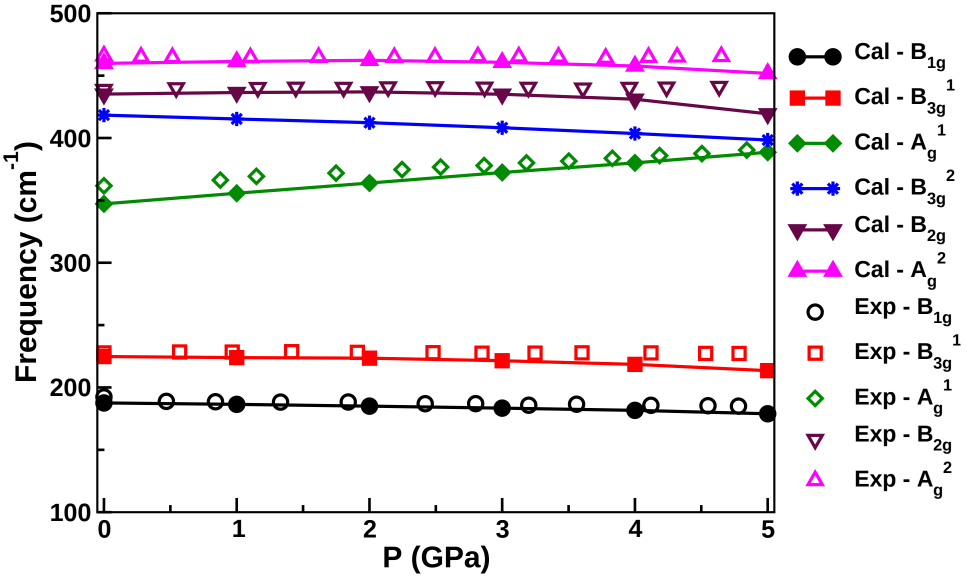

Figure 3.7: Calculated (PBE-D2) Raman frequencies under pressure compared with experiments (Ref. [26]).

3.4 Transition to the *A*7 structure

Black phosphorus transforms under pressure from the orthorhombic structure (*A*17) to a rhombohedral structure (*A*7) at roughly $P_t = 5$ GPa [5–9]. This transition was studied previously by Schiferl [23] using an empirical local pseudopotential, and was analysed by Burdett et al [62] using the concept of orbital symmetry conservation. Chang and Cohen [24] performed calculations using the pseudopotential method within the local density approximation. However, they found it necessary to apply a shift (of 2.3 mRy per P atom) to their calculated total energy of the *A*7 phase in order to reproduce the experimental value of the transition pressure, which is pointing out the inadequacy of the LDA to describe correctly the energetics of black phosphorus. This is in contradiction with the results of Ahuja [19] who obtained a transition pressure of P_t= 4.5 GPa using the LMTO method and LDA. In the present paper, we also studied the transition pressure using D2's vdW functional. This leads to a value of $P_t = 0.8$ GPa, implying that although the D2 functional is correctly ranking the *A*17 structure versus the *A*7 structure in terms of the total energy at $P = 0$ GPa, the transition happens at a too low pressure in the calculation compared to the experimental pressure. Similar calculations were carried out using either of the PW91, PBE, OBS or TS functionals, but in all cases, the transition pressure is found to be too low, within a 1-GPa range around the value obtained with the D2 functional. Possibly, a better agreement with the experimental transition pressure could be obtained using a more advanced description of the van der Waals interactions, such as the adiabatic-connection fluctuation-dissipation method [63–65] in the random phase approximation or quantum Monte-Carlo [66] method. However, these methods are numerically heavier than the simple dipole-dipole corrections considered here, and to our knowledge the implementation of the corresponding forces necessary to perform the structural relaxation under pressure is not available.

3.5 Conclusions

First-principles calculations based on the DFT have been used to investigate the structural properties of black phosphorus within LDA and GGA. It was found that the calculated material parameters differ significantly from the experimental data, whereas, including empirical methods to account for van der Waals interactions (DFT-D) leads to structural properties in good agreement with experiments. This demonstrates that van der Waals interactions play a major role in black phosphorus. Among the OBS, TS and D2 parametrizations of van der Waals interactions, the calculated structural parameters are in closest agreement with experimental data when PBE-D2 is used. Also, the influence of external pressure on the lattice parameters were calculated. The b lattice parameter was found to be most sensitive to which vdW functional was used, reflecting the dominance of van der Waals interactions along the crystallographic b-direction. Furthermore, the elastic properties of single crystal as well as polycrystalline black phosphorus were examined using the GGA-PBE-D2 functional. Our calculations confirm that black phosphorus is mechanically stable anisotropic material, and that the system is stiffest along the a-axis. The calculated shear anisotropy factors for different directions indicate strong anisotropies for shears perpendicular to the a and b axes. The polycrystalline bulk, shear and Young's moduli, as well as Poisson's ratio were calculated. From the ratio of bulk to shear modulus, black phosphorus is found to be brittle. Finally, the frequencies of Raman active vibrational modes were calculated, and they are in excellent agreement with the available experimental data.

References

[1] S. Böcker and M. Häser, Z. Anorg. Allg. Chem., **321**, 258 (1995).

[2] A. Morita, Appl. Phys. A: Solid Surf., **39**, 227 (1986).

[3] Y. Akahama, S. Endo and S. Narita, Physica, **139-140**, 397 (1986).

[4] L. Cartz, S. R. Srinivasa, R. J. Riedner, J. D. Jorgensen and T. G. Worlton, J. Chem. Phys., **71**, 1718 (1979).

[5] J. C. Jamieson, Science, **139**, 1291 (1963).

[6] M. J. Duggin, J. Phys. Chem. Solids, **33**, 1267 (1972).

[7] T. Kikegawa and H. Iwasaki, Acta Cryst., **B 39**, 158 (1983).

[8] T. Suzuki, T. Yagi, S. Akimito, T. Kawamura, S. Toyoda and S. Endo, J. Appl. Phys., **54**, 748 (1983).

[9] M. Okajima, S. Endo, Y. Akahama and S. Narita, J. Appl. Phys., **23**, 15 (1984).

[10] Y. Akahama, M. Kobayashi and H. Kawamura, Phys. Rev. B, **59**, 8520 (1999).

[11] Y. Akahama and H. Kawamura, S. Carlson, T. Le Bihan and D. Häusermann, Phys. Rev. B, **61**, 3139 (2000).

[12] H. Asahina, Y. Maruyama and A. Morita, Physica, **117 - 118**, 419 (1983).

[13] S. Narita, Y. Akahama, Y. Tsukiyama, K. Muro, S. Mori, S. Endo, M. Taniguchi, M. Seki, S. Suga, A. Mikuni and H. Kanzaki, Physica B+C, **117 - 118**, 422 (1983).

[14] T. Takahashi, K. Shirotani, S. Suzuki and T. Sagawa, Solid State Commun., **45**, 945 (1983).

[15] M. Ikezawa, Y. Kondo and I. Shirotani, J. Phys. Soc. Japan, **52**, 1505 (1983).

[16] Y. Fujii, Y. Akahama, S. Endo, S. Narita, Y. Yamada and G. Shirane, Solid State Commun., **44** 579, (1982).

[17] B. Nolang, O. Eriksson and B. Johansson, J. Phys. Chem. Solids, **51**, 1025 (1990).

[18] M. Rajagopalan, M. Alouani and N. E. Christensen, J. Low Temp. Phys., **75**, 1 (1989).

[19] R. Ahuja, Phys. Stat. Sol. B, **235**, 282 (2003).

[20] O. K. Andersen, Phys. Rev. B, **12**, 3060 (1975).

[21] H. Asahina and A. Morita, J. Phys. C: Solid State Phys., **17**, 1839 (1984).

[22] C. Kaneta, H. Katayama-Yoshida and A. Morita, J. Phys. Soc. Japan, **55**, 1213 (1986).

[23] D. Schiferl, Phys. Rev. B, **19**, 806 (1979).

[24] K. J. Chang and M. L. Cohen, Phys. Rev. B, **33**, 6177 (1986).

[25] I. Shirotani, K. Tsuji, M. Imai, H. Kawamura, O. Shimomura, T. Kikegawa and T. Nakajima, Phys. Lett. A, **144**, 102 (1990).

[26] Y. Akahama, M. Kobayashi and H. Kawamura, Solid State Commun., **104**, 311 (1997).

[27] A. Nishikawa, K. Niizeki and K. Shindo, Phys. Status Solidi B, **223**, 189 (2001).

[28] F. J. H. Ehlers and N. E. Christensen, Phys. Rev. B, **69**, 214112 (2004).

[29] Ø. Prytz and E. Flage-Larsen, J. Phys. Cond. Matt., **22**, 015502 (2009).

[30] S. M. Clark and J. M. Zaug, Phys. Rev. B, **82**, 134111 (2010).

[31] S. E. Boulfelfel, G. Seifert, Yu. Grin and S. Leoni, Phys. Rev. B, **85**, 014110 (2012).

[32] Y. Du, C. Ouyang, S. Shi and M. Lei, J. Appl. Phys., **107**, 093718 (2010).

[33] S. Grimme, J. Comp. Chem., **27**, 1787 (2006).

[34] M. C. Payne, M. P. Teter, D. C. Allan, T. A. Arias and J. D. Joannopoulos, Rev. Mod. Phys., **64**, 1045 (1992).

[35] M. D. Segall, P. J. D. Lindan, M. J. Probert, C. J. Pickard, P. J. Hasnip, S. J. Clark and M. C. Payne, J. Phys. Cond. Matt., **14**, 2717 (2002).

[36] D. Vanderbilt, Phys. Rev. B, **41**, 7892 (1990).

[37] D. M. Ceperley and B. J. Alder, Phys. Rev. Lett., **45**, 566 (1980).

[38] J. P. Perdew and A. Zunger, Phys. Rev. B, **23**, 5048 (1981).

[39] J. P. Perdew and Y. Wang, Phys. Rev. B, **45**, 13244 (1992).

[40] J. P. Perdew, K. Burke and M. Ernzerhof, Phys. Rev. Lett., **77**, 3865 (1996).

[41] F. Ortmann, F. Bechstedt and W. G. Schmidt, Phys. Rev. B, **73**, 205101 (2006).

[42] A. Tkatchenko and M. Scheffler, Phys. Rev. Lett., **102**, 073005 (2009).

[43] T. Bucko, J. Hafner, S. Lebègue, and J. G. Angyán, J. Phys. Chem. A, **114**, 11814 (2010).

[44] T. Bucko, J. Hafner, S. Lebègue, and J. G. Angyán, Phys. Chem. Chem. Phys., **14**, 5389 (2012).

[45] T. F. Zhang, M. Sacchi, D. A. King, and S. M. Driver, J. Phys. Chem. C, **116**, 5637 (2012).

[46] B. Santra, J. Klimes, D. Alfe, A. Tkatchenko, B. Slater, A. Michaelides, R. Car and M. Scheffler, Phys. Rev. Lett, **107**, 185701 (2011).

[47] N. Marom, J. Bernstein, J. Garel, A. Tkatchenko, E.Joselevich, L. Kronik and O. Hod, Phys. Rev. Lett., **105**, 046801 (2010).

[48] H. J. Monkhorst and J. Pack, Phys. Rev. B, **13**, 5188 (1976).

[49] P. Pulay, Mol. Phys., **17**, 197 (1969).

[50] M. J. Mehl, J. E. Osburn, D. A. Papaconstantopoulus and B. M. Klein, Phys. Rev. B, **41**, 10311 (1990).

[51] P. Ravindran, L. Fast, P. A. Korzhavyi and B. Johansson, J. Appl. Phys., **84**, 4891 (1998).

[52] Y. Kozuki, Y. Hanayama, M. Kimura, T. Nishitake and S. Endo, J. Phys. Soc. Japan **60**, 1612 (1991).

[53] M. Yoshizawa, I. Shirotani and T. Fujimura, J. Phys. Soc. Japan, **55**, 1196 (1986).

[54] L. Hedin and B. I. Lundqvist, J. Phys. C, **4**, 2064 (1971).

[55] T. Akai, S. Endo, Y. Akahama, K. Koto and Y. Maruyama, High Pressure Research, **1**, 115 (1989).

[56] M. Born and K. Huang, *Dynamical Theory of Crystal Lattices*, Oxford University Press, Oxford (1998).

[57] W. Voigt, Ann. Phys., **38**, 573 (1889).

[58] A. Reuss, Z. Angew. Math. Mech., **9**, 55 (1929).

[59] R. Hill, Proc. Phys. Soc., London, Sect. A, **65**, 349 (1952).

[60] S. F. Pugh, Philos. Mag., **45**, 823 (1954).

[61] Ch. Bheema Lingam, K. Ramesh Babu, Surya. P. Tewari and G. Vaitheeswaran, J. Comp. Chem., **32**, 1734 (2011).

[62] J. K. Burdett and S. Lee, J. Solid State Chem., **44**, 415 (1982).

[63] O. Gunnarsson and B. I. Lundqvist, Phys. Rev. B, **13**, 4274 (1976).

[64] D. C. Langreth and J. P. Perdew, Solid State Comm., **17**, 1425 (1975).

[65] D. C. Langreth and J. P. Perdew, Phys. Rev. B, **15**, 2884 (1977).

[66] W. M. C. Foulkes, L. Mitas, R. J. Needs, and G. Rajagopal, Rev. Mod. Phys., **73**, 33 (2001).

[67] X. Gonze, Phys. Rev. B, **55**, 10337 (1977).

[68] S. Sugai and I. Shirotani, Solid State Commun., **53**, 753 (1985).

Chapter 4

Structural and dynamical stability of molecular solid Xenon difluoride.

In the previous chapter, the results of various dispersion corrected density functional theory methods (DFT-D) were presented for elemental phosphorus and found that PBE-D2 method preferably presents the good description of ground state properties. Similar to layered materials, molecular solids are also good example for the weakly bonded systems and often dispersion interactions dominates the stability of system. This chapter focus towards understanding the role of van der Waals interactions on structural properties from ambient to wide range of pressures using PBE-D2 method for well known molecular sold ***Xenon difluoride (XeF_2)***. In addition, the stability of XeF_2 up to 120 GPa was revisited in terms of energetics and phonons .

4.1 Introduction

Xenon (Xe) is a noble gas, having a closed-shell electronic configuration $5s^2 5p^6$ would therefore be expected to be chemically unreactive, and it was believed that it would not have the tendency to form chemical compounds because of the stability of its electronic structure [1]. After several years of experiments in the area of halogen chemistry with noble gases, Hoppe et al. [2] published a short communication about the synthesis of XeF_2 by an electrical discharge method, and a comprehensive study of the synthesis and various physical and chemical properties of XeF_2 was carried out by the same group [3] who concluded that XeF_2 is colourless with nauseating odor, exhibits a considerable birefringence and also is diamagnetic. Immediately after the successful synthesis of XeF_2, efforts have been made to refine the crystal structure, and it was concluded that XeF_2 crystallizes in a tetragonal structure with space group *I4/mmm* [4, 5]. Xenon difluoride is now commercially available, and is the noble-gas fluoride, which is most easy to synthesize in high purity form [6]. It is quite stable at room temperature and has application as convenient fluorinating agent in synthetic organofluorine chemistry [7]. This opened a new avenue for using XeF_2 in radiopharmacueticals for use in medical imaging by means of positron emission tomography. In addition Xenon difluoride is now extensively used in the electronics industry as a dry, pas phase etchant to isotropically etch elements such as Si, Mo, and Ge in the production of microelectromechanical systems [8].

Quite recently, researchers from high-pressure experimental and theoretical groups reported the formation of solid novel Xe compounds with simple halides, oxides, hydrides, transition metals such as Fe/Ni and liquid mixture of Xe and ethane under high pressure [9–15]. However, Xenon-hydrides[13] and -oxides [12] can be formed only under pressure, whereas Xe-F compounds have been identified with +2 to +8 oxidation states at ambient and high pressure conditions [11]. Under ambient conditions, XeF_2 is the most stable molecular crystal among the other noble gas fluorides and, especially, its simple structure provides the large share of ionicity between Xe and most electronegative atom F [4, 5, 16]. It crystallizes in body centered tetragonal structure with space group *I4/mmm* (Z=2), with lattice parameters a = 4.315 Å and c = 6.990 Å [16]. It consists **of** linear chain of XeF_2 molecules along c-axis with a equal bond length (d_1=1.99 Å) between Xe and F atoms, the arrangement of XeF_2 molecules along a-axis shows van der Waals (vdW) forces due to nearest neighbor distance between Xe-Xe contacts, the corresponding experimental crystal structure of XeF_2 unit cell is shown in Figure. 4.1. Earlier studies of XeF_2 were mainly focused on the molecular geometry, bonding, structural as well as vibrational properties under pressure [17–20]. Schwarz and co workers reported the structural and optical properties of XeF_2 up to 98 GPa and concluded that the tetragonal structure of the molecular solid is stable in the pressure range studied by means of powder

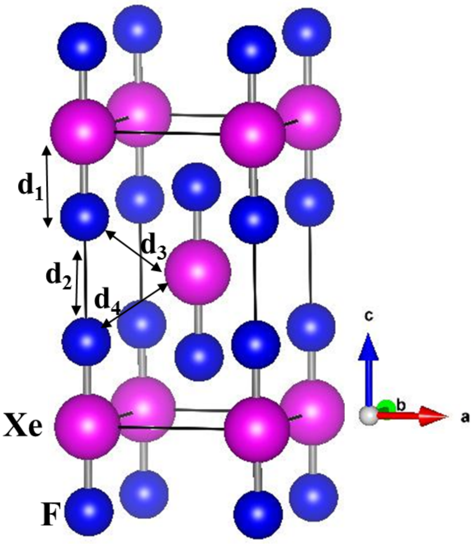

Figure 4.1: Experimental crystal structure of XeF_2 unit cell. Here d_1, d_2 (along c-axis) and d_3, d_4 (along a-axis) nearest neighbor contacts between Xe and F atoms

x-ray diffraction measurements [21, 22]. The authors also reported that the compressions curves are highly anisotropic and a color change from white to yellow is seen under pressure around 45 GPa indicating a pressure induced decrease of the optical gap [23]. Recently, Kim et al conducted experiments on solid XeF_2 under pressure and reported nearly four possible structural phase transitions up to 70 GPa and also found XeF_2 to become metallic at this pressure [10]. On contrary to experiments, Dominik et al. [11] predicted the stability of XeF_2 using genetic algorithm techniques and found that the parent tetragonal structure is stable upto 105 GPa and then transforms to Pnma symmetry [11]. The authors also claimed metallization around 60 GPa with standard the Perdew-Burke-Ernezrhof (PBE) exchange-correlation functional which is well known to underestimate the band gaps of insulators and semiconductors when compared to experiments. To the best of our knowledge, there are no other theoretical reports available to address the complete structural, vibrational and electronic properties on solid XeF_2.

Motivated by these, we present a careful re-examination on structural, electronic and vibrational properties of XeF_2 by means of calculations based on the density functional theory (DFT). To be more specific, care has been taken to examine the effect of van der Waals (vdW) interactions on the ground state properties and metallization of XeF_2 at high pressures. Recent developments in DFT calculations provides several implementations to treat vdW forces. Among them, Grimme [24] method is found to be successful in reproducing the ground state properties for molecular crystals and layered materials [25–30]. Hence, this method is used in the present chapter along with standard GGA-PBE method for determining the structural and vibrational properties.

4.2 Computational details

The calculations of the structural and dynamical characteristics were carried out within the generalized gradient approximation (GGA [31] using the plane-wave pseudopotential technique as implemented in the Pwscf package [32]. Structural optimizations for each pressure were performed by constant pressure variable-cell method, which minimize total energies as well as forces on both lattice parameters and internal coordinates of Fluorine (F) atom. Trouiller-Martins type norm conserving pseudopotentials were adopted to treat valence electronic configurations. Structural minimizations were done by Broyden-Fletcher-Goldfarb-Shanno (BFGS) algorithm [33] with the convergence criteria set in a way of that error in total energies should be less than 1e-07 eV, residual forces less than 1e-4 eV/Å, and stress is limited to 0.05 GPa. All these calculations were performed with a plane wave basis kinetic energy cut off of 120 Ry and a (14 12 12) Monkhorst-Pack *k*-point [34] grid to sample irreducible Brillouin zone (IBZ). The vdW interaction is taken into account by means of Grimme's (called as D2 and D2) correction to GGA-PBE [24]. The dynamical properties such as zero point motions and complete phonon dispersion relations were calculated from the response to small atomic displacements within the linear response approach [35] as implemented in Pwscf. We computed the dynamical matrices by using the (4 4 4) *q* grid for the *I4/mmm* phase of XeF_2 in the IBZ, and the full phonon dispersion was obtained through Fourier interpolation of the dynamical matrices.

Table 4.1: Calculated ground-state properties of tetragonal XeF_2 at ambient pressure using PW-PP method. a, and c are the lattice parameters (in Å), V is the volume (in Å^3) of the tetragonal unit cell, d_1, d_2 (along c-axis) and d_3, d_4 (along a-axis) bond distances (in Å), B and B' are bulk modulus (in GPa) and its pressure derivatives. The experimental values are taken from Ref. 16

Parameter	PBE	PBE+D2	Exp
a	4.54	4.24	4.315
c	7.20	7.05	6.990
V	148.22	126.84	130.15
u	0.282	0.288	0.286
d_1	2.03	2.03	1.99
d_2	3.14	2.99	3.02
d_3	3.57	3.35	3.42
d_4	3.24	3.05	3.08
B	14.13	10.45	9.8
B'	8.9	6.5	5.8

4.3 Ground state structural properties

First the zero-pressure structure was optimized using the standard PBE functional and PBE+D2 methods. For this, we adopted the experimental crystal structure of XeF_2 and performed structural optimizations by minimizing forces on lattice parameters and internal coordinate (u) of F atom. Table. 4.1 contains the calculated lattice parameters of the tetragonal cell, *u* of the F atom, and bond lengths using two computed methods in the present work together with experimental values. From this it can be seen that, in the case of the standard DFT functional, equilibrium volume differs by +14% when compared to experiment and corresponding *a*- lattice parameter (is overestimated by +5%) shows large discrepancies with experimental value as compared with *c*- lattice parameter (overestimated by +3%). As discussed in previous section, the weak vdW forces are more pronounced along *a* - axis and this variation could not be captured with standard PBE functional due to limitation of semilocal method to treat vdW forces which are non local in nature. However, PBE+D2 method, significantly improved the values such as -2% for *a*- lattice parameter, +0.8% for *c*- lattice parameter and volume is also good in agreement with experiments with a underestimation of -2.1%. The obtained internal coordinate is shown equal variation with experiments using both methods. On the other hand, similar situation was observed in calculated intra and intermolecular bond lengths. The obtained intra-molecular Xe-F bond length (d_1, along *c*-axis as shown in Figure 4.1) is 2.03 Å using both PBE and PBE+D2 methods, which is comparable with experimental value of 1.99 Å. While other intermolecular bond lengths (d_2 along *c*-axis, d_3 and d_4 along *a*-axis) are overestimated to a greater extent with PBE method and the introduction of dispersion correction is seen to have considerable improvement over PBE results. Overall, the observed results suggest that vdW forces play an important role in determining the ground state properties of XeF_2, and the PBE+D2 method is found to work well at ambient pressure.

4.4 Role of van der Waals forces up to 5 GPa

As a next step, we examine the effect of vdW forces on geometry of XeF_2 under pressure. Experimental study by Kim et al. [10] reported a structural phase transitions in XeF_2 starting from 7 GPa [10]. Hence we restrict ourself in calculating the structural properties from 0 to 5 GPa and 6 to 10 GPa with a step sizes of 0.5 and 1 GPa respectively. Figure 4.4 shows the calculated pressure dependence of lattice parameters (*a*, *c*) and volume (*V*) with PBE and PBE+D2 methods along with experimental values reported by Schwarz and Syassen [16]. From this it is clearly seen, that the calculated lattice parameters and volumes with PBE+D2 are in good agreement with experiments from 0 to 5 GPa, whereas both PBE and PBE+D2 shows similar behavior between 5 to 10 GPa. In addition at low pressure region (0 to 5 GPa), the *a* - parameter calculated with PBE+D2 method is closer to the experiment than PBE results, and above 5 GPa, the two methods yield identical results. On the other hand, the *c* - parameter is slightly overestimated using both PBE and PBE+D2 in the complete pressure range of 0 to 10 GPa. Also, the *a*-axis is more compressible between 0 to 5 GPa with a large reduction (0.28 Å with in PBE+D2 and 0.54 Å with in PBE) than *c*-axis (0.17 Å with in PBE+D2, 0.28 Å with in PBE), and whereas in pressure region 5 to 10 GPa , lattice parameters are lowered around 0.1 Å with both methods. Further-

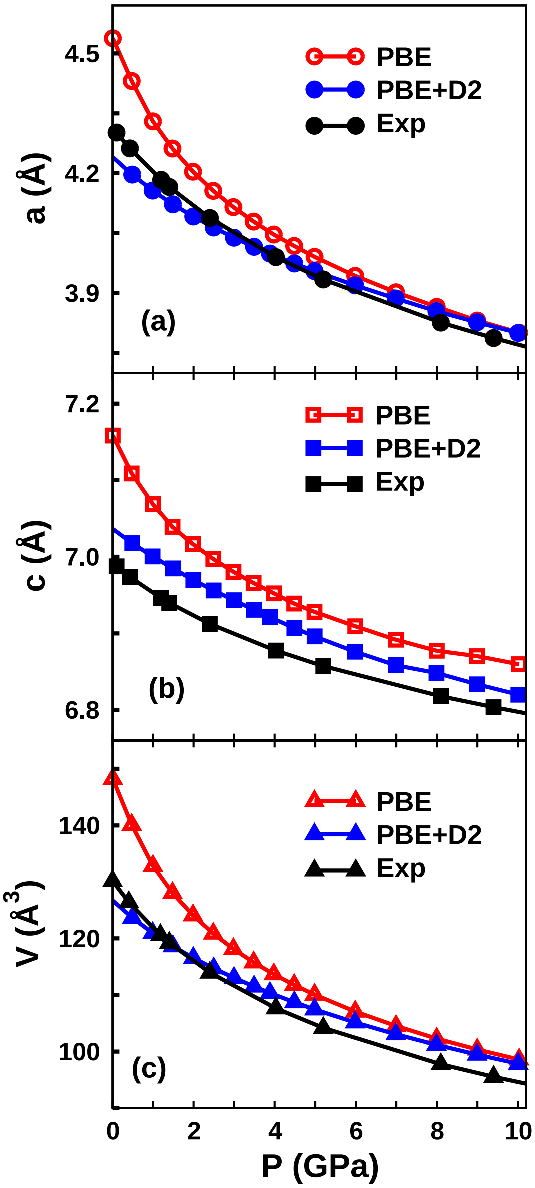

Figure 4.2: Comparison of the pressure dependent lattice parameters (*a*, *c*) up to 10 GPa within PBE (in red), and PBE + Grimme (in blue), compared to experimental values (Ref. [16, 23]).

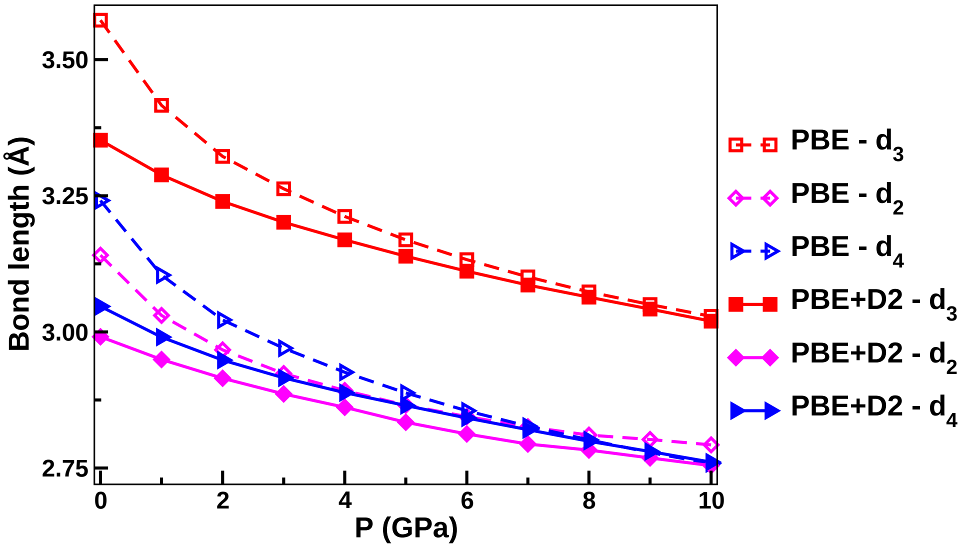

Figure 4.3: Calculated pressure dependent bond lengths (in Å) along ***a*** (d_3, d_4) and ***c*** -axes (d_2) of XeF_2 (cf. Fig 1) up to 10 GPa.

more, the computed intermolecular distances d_2(along ***c*** -axis), d_3 and d_4 (along ***a*** -axis) also show similar picture in these pressure regions (see Figure. 4.3). Since, there are no experimental bond lengths available, in the present case we compared our calculated values between PBE and PBE+D2. In low pressure region 0 to 5 GPa, a reduction of 0.42 and 0.64 Å for d_3 and d_4 bond lengths respectively are obtained using PBE method and these values further decreases to 0.16 and 0.22 Å with D2 correction to PBE. As for the pressure region 5 to 10 GPa, all bond lengths shows less variation with pressure and the reduction values are in the order of 0.1 Å with both methods. Definitely, these variations in the reduction of bond lengths are due to response of ***a*** lattice parameter with pressure and this as expected resembles the effect of vdW forces on XeF_2. The intra molecular bond length d_1 results smaller variation with pressure using both functionals, which is not shown in Figure. 4.3. Together with all these results, we confirms that the PBE+D2 method improved the results in the lower pressure region and the corrections to PBE do not play major role at above 5 GPa, which confirms that the vdW forces do not affect the geometry above 5 GPa.

The pressure-volume relation is a part of the-equation-of-state of the system.

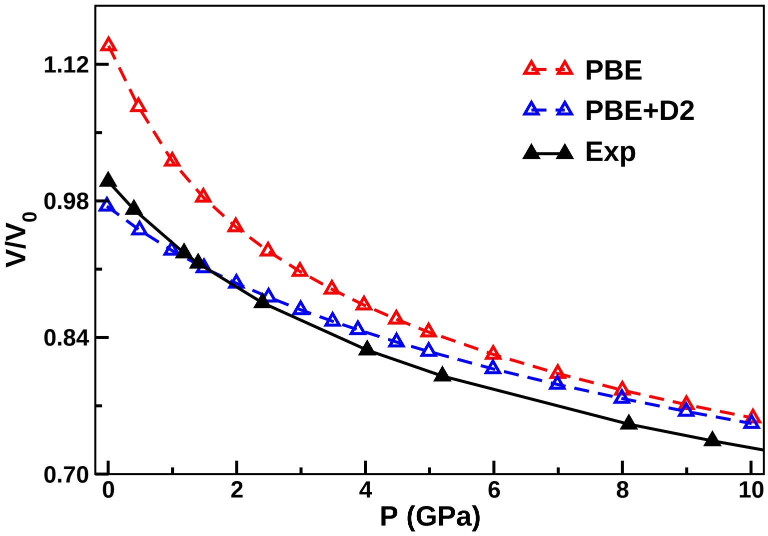

Figure 4.4: Comparison of the pressure dependent volume (V) up to 10 GPa within PBE (in red), and PBE+Grimme (in blue), compared to experimental values (Ref. [16, 23]).

In this work, the calculations for the low pressure region of 0 to 5 GPa are fitted to the Murnaghan equation with respect to the experimental volume. The obtained bulk modulus and its pressure derivatives using standard and vdW corrected methods are presented in Table. 4.1. We found that the bulk modulus obtained with PBE is in poor agreement with experiments, while the other one obtained with PBE+D2 is in very good agreement with the experimental value.

4.5 Energetics and phonons up to 120 GPa

As mentioned in the introduction of this chapter, earlier high pressure experiments reported four possible polymorphic phase transitions such as from ground state tetragonal phase *I4/mmm* → *Immm* (at 7 GPa) → *Pnnm1* (at 21 GPa) → *Pnnm2* (at 32 GPa) → *Fmmm* (at 70 GPa). Dominik et al. [11] predicted *I4/mmm* phase is stable up to 100 GPa using genetic algorithms, and also reported that the tetragonal *I4/mmm* phase transforms to the orthorhombic *Pnma* phase at 105 GPa. Since, it's a goal of the present work to examine metallization of XeF_2 under pressure, it is essential to determine the high-pressure structures correctly, and

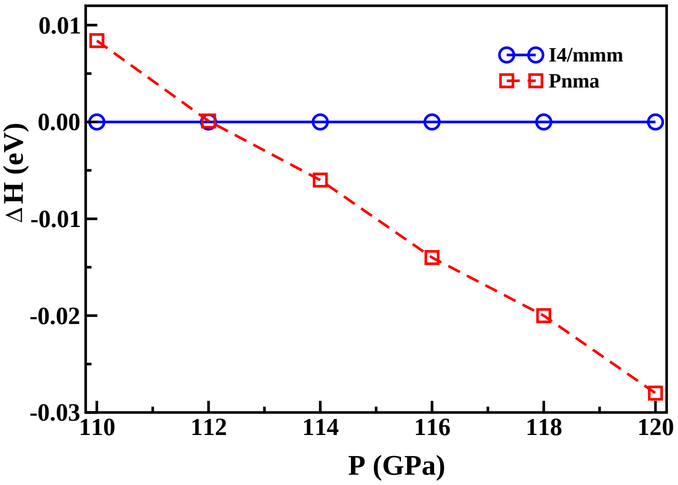

Figure 4.5: Calculated enthalpy difference per formula unit between *I4/mmm* and *Pnma* from 110 to 120 GPa.

the calculations were extended from 10 to 120 GPa (with a step size of 10 GPa) in order to examine the stability of different phases of XeF_2. To understand the stability of *I4/mmm* phase under pressure, we have chosen two well-known criteria for solids such as total energies for the ground state as well as high pressure phases and phonon dispersions for *I4/mmm* phase in the present work. From the structural properties up to 5 GPa, we noticed that vdW forces do not play a very important role for pressures beyond 5 GPa, and just the PBE method was used for these calculations. From the total energies, it was found that the *I4/mmm* phase has appropriate minimum energy (per one formula unit) than any other experimentally observed structures up to 100 GPa, and the total energy differences are $\sim$ -0.5 eV with *Immm*, *Pnnm1*, *Pnnm2* structures and $\sim$ -2.2 eV with *Fmmm* structure at their transition pressures (0, 21, 32 and 70 GPa) and a similar situation was observed at near pressure regions of reported transition pressures. This agrees with what was found by Dominik et al.[11], and also the detailed discussions of discrepancy between experiments and theory were reported in their work. Upon increasing the pressure beyond 100 GPa, we found an energetic sequence E(*Pnma*) $<$E(*I4/mmm*) from 110 to 120 GPa. This indicates a possible phase transition between these pressure regions. For the completeness, we

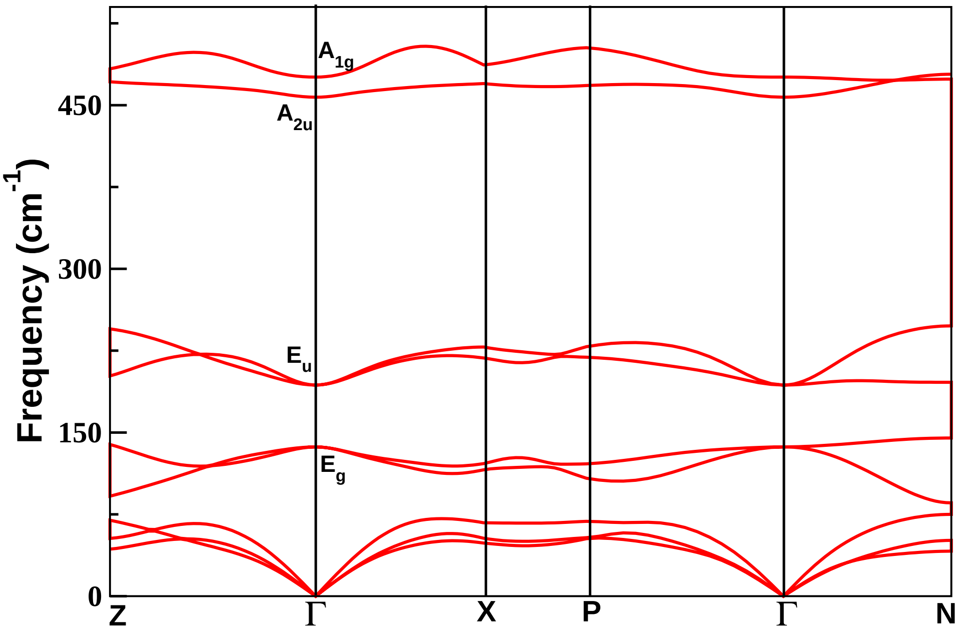

Figure 4.6: Calculated Phonon dispersions 0 GPa with in PBE+D2 method.

plotted the enthalpy differences between the *I4/mmm* and *Pnma* phases of XeF_2 with in the pressure region 110-120 GPa by using a step size of 2 GPa (see Figure 4.5). It can be seen that the *Pnma* phase becomes more favorable above 112 GPa. The difference in the obtained transition pressure value in the present work and the earlier work is expected due to the usage of different pseudopotentials in the works.

Although the calculated total energies show stability of ground state structure of XeF_2 up to 110 GPa, we have performed the lattice dynamics of the *I4/mmm* phase by computing complete phonon dispersion under pressure in their fully relaxed configurations. The obtained dispersion curves at ambient pressure (see Fig. 4.6) as well as high pressures are shown in Fig. 4.7 and Fig. 4.8 respectively.

Note that the calculations for 0 GPa are within PBE+D2 optimized geometries and the other high pressure results (10, 20, 40 and 70 GPa) were carried out within the geometries of PBE method. It should also be pointed out that, we determined the dynamical stability of *I4/mmm* phase around the reported transition pressures by Dominik et al.[11]. From the crystal structure of *I4/mmm* phase- XeF_2, a

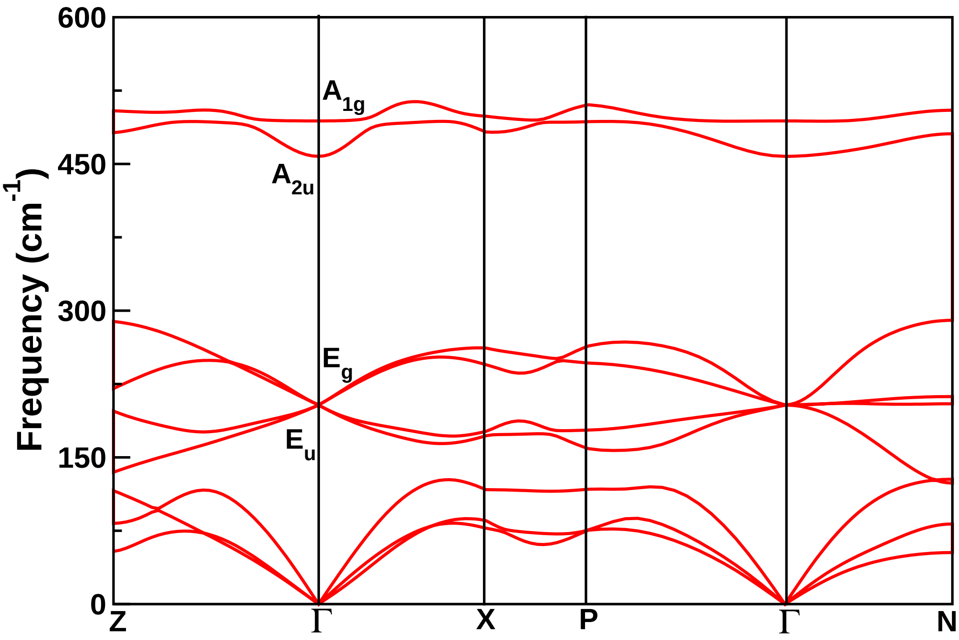

(a)

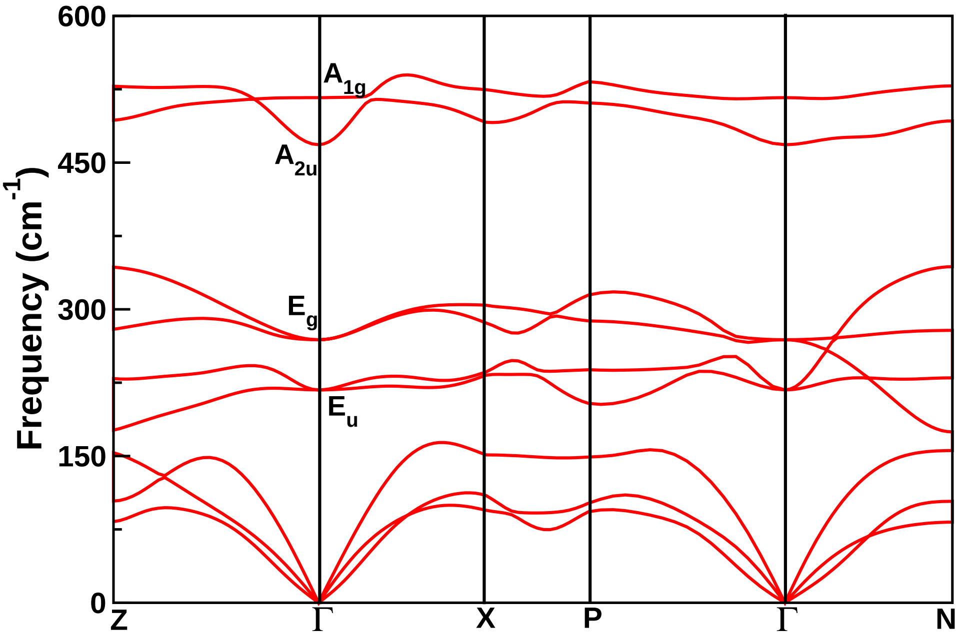

(b)

Figure 4.7: Calculated phonon dispersion at (a). 10, and (b). 20 GPa with in PBE method.

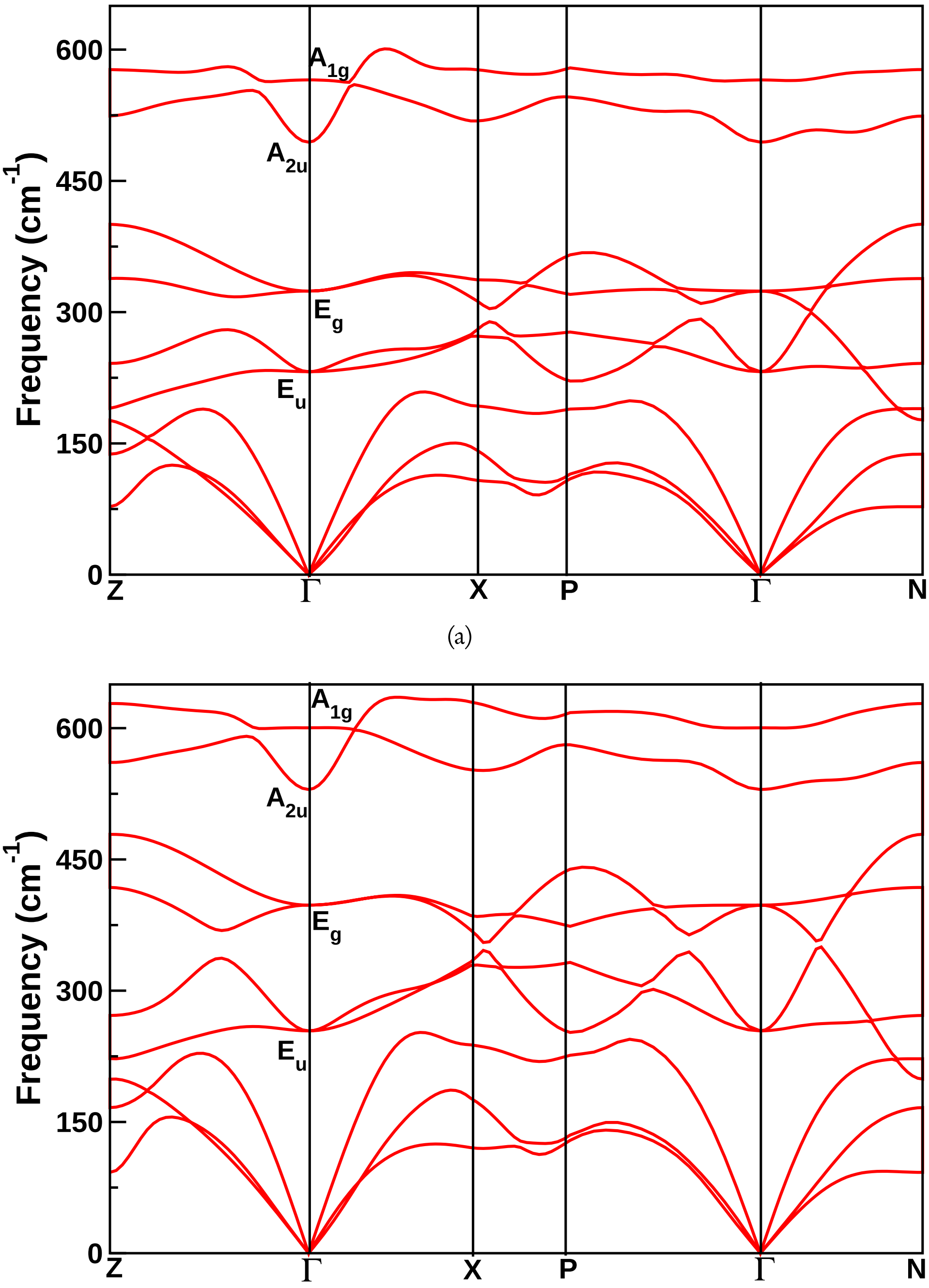

(a)

(b)

Figure 4.8: Calculated phonon dispersion at (a). 40, and (b). 70 GPa with in PBE method.

factor group theory symmetry analysis indicates that the zone centered acoustic and optical frequencies are distributed as $\Gamma_{acoustic}$= A_{2u}⊕2 E_u for acoustic modes; $\Gamma_{optical}$= $2E_g \oplus 2E_u \oplus A_{1g} \oplus A_{2u}$ for optical modes. Here, E_g and A_{1g} are Raman active and E_u and A_{2u} are IR active frequencies. From the phonon dispersion curves we could unambiguously show the dynamical stability of *I4/mmm* phase at ambient and high pressures. Hence, we can clearly see that the *I4/mmm* phase is stable throughout the pressure region studied which compliments the total energy calculations in the present work.

As mentioned earlier, metallization of *I4/mmm* phase of XeF_2 is one of the aim in this work, we further proceed to calculate the band gaps of XeF_2 under pressure. Similar to previous theory [11], we also found metallization of XeF_2 at around 70 GPa using standard DFT methods. However, it is a well known fact that the standard DFT methods always underestimate (~ 40 %) band gaps with experiments and it is necessary to revisit the same when compared to beyond DFT methods. On the other hand, the Quasi particle Self-consistent *GW* (QSGW)calculations shows that XeF_2 remains as a semiconductor up to very high pressures and likely to become metal beyond 150 GPa[1]

Apart from the phase transition, we also observed strong anisotropy in the calculated lattice parameters up to 100 GPa. This was calculated through pressure coefficients($\gamma = \frac{1}{X}\frac{dX}{dP}$, X=$a$, c) of relative lattice parameters. The calculated γ values for lattice parameters $\boldsymbol{a}$ and $\boldsymbol{c}$ are $\gamma_a = 6.2 \times 10^{-3}$ and $\gamma_c = 1.7 \times 10^{-3}$ respectively, between the pressure region of 10 to 100 GPa. The calculated relative lattice parameters and volume along with experimental data[16] are shown in Figure. 4.9. Good agreement between the calculations and the experiment can be seen and the compressibility along $\boldsymbol{a}$-axis is larger than along the $\boldsymbol{c}$-axis. Therefore it is expected that the reduction in inter-molecular bond lengths is larger along $\boldsymbol{a}$-axis, and this is the case, as can be seen from Fig. 4.10. Overall, it is found, that the compressibility of the *I4/mmm* phase becomes highly anisotropic with increasing

---

[1]

- *QSGW:* These calculations performed by A. Svane and N. E. Christensen using quasi-particle self-consistent *GW* (QSGW) approximation.

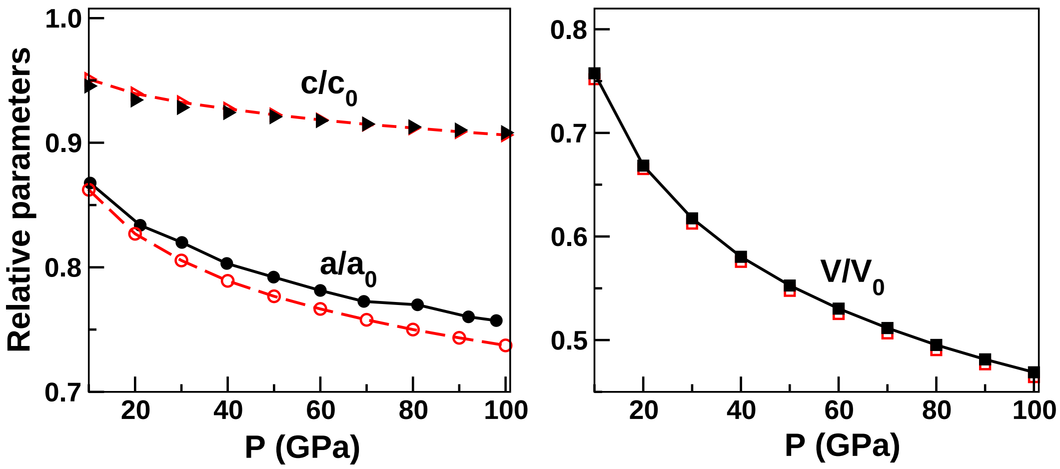

Figure 4.9: Comparison of pressure dependence of the relative lattice parameters (a/a_0, c/c_0) and volume (V/V_0) of XeF_2 up to 100 GPa within PBE (in open symbols), compared to experimental values (in closed symbols) from Ref. [16, 23]. Here a_0, c_0 and V_0 are 0 GPa experimental parameters (see Table 1).

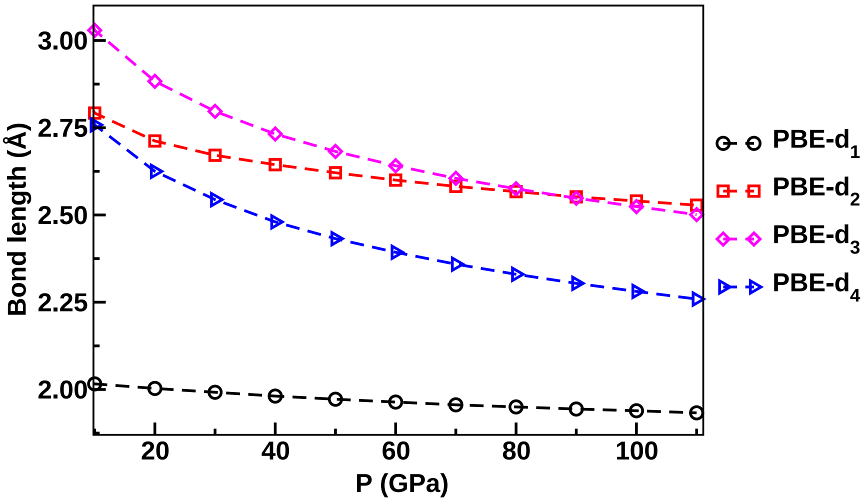

Figure 4.10: Calculated bond distances d_1(Xe-F), d_2(F-F) along c-axis and d_3(Xe-F), d_4(F-F) along a-axis of XeF_2 from 10 to 100 GPa using PBE method. The description of bond lengths are in Fig. 1

pressure. The reduction in the volume ($\Delta V/V$) upto 50 GPa are 0.51 and 0.43 as calculated with PBE and PBE+D2, respectively, and are in close agreement with reported value of 0.45 [16].

4.6 Conclusions

In summary, we have presented a detailed study on the structural stability, electronic properties and possible metallization of XeF_2 under pressure. The *I4/mmm* phase is predicted to be energetically and dynamically stable up to 110 GPa. The lattice parameters and volume calculated with the Grimme dispersion correction to standard DFT method at low pressures are closer to experiments than those obtained with the standard PBE. We have also successfully reproduced the structural properties under pressure up to 100 GPa. More importantly, the role of vdW forces and then influence on the structural properties at low pressure region up to 5 GPa was reported through dispersion corrected DFT method Grimme. We have also confirmed the stability of of *I4/mmm* phase of XeF_2 under pressure up to 100 GPa using total energies and phonon dispersions. Our computations are also in fair agreement with predicted transition from tetragonal to orthorhombic structure by genetic algorithms and obtained transition pressure shows slight variations due to different methodologies.

References

[1] L. Pauling, *College Chemistry*, Second edition., W. H. Freeman, San-Francisco 83 (1955)

[2] R. Hoppe, W. Dähne, H. Mattauch, K. M. Rödder, Angew. Chem. Int. Ed. **1**, 599 (1962); Angew. Chem. Int. Ed. **74**, 903 (1962)

[3] R. Hoppe, H. Mattauch, K. M. Rödder, W. Dähne, Z. Anorg. Allg. Chem. **324**, 214 (1963)

[4] S. Siegel, E. Gebert, J. Am. Chem. Soc. **85**, 240 (1963)

[5] H. A. Levy, P. A. Agron, J. Am. Chem. Soc. **85**, 241S (1963)

[6] R. Betz, G. J. Schrobilgen, Z. Anorg. Allg. Chem. 1385 (2012)

[7] D. F. Halpern, in: *Encyclopedia of Reagents for Organic Synthesis*, Second edition, Vol. 13 (Eds: L. A. Paquette, D. Crich, P. L. Fuchs, G. A. Molander), John Wiley and Sons Ltd., Chichester, UK, 10869 (2009)

[8] C. Easton, C. B. O eal, J. Microelectrochem. Syst. **18**, 1054 (2009)

[9] W. Grochala, Chem. Soc. Rev., **36**, 163 (2007)

[10] M. Kim, M. Debessai, C. -S. Yoo, Nat. Chem., **2**, 61 (2010).

[11] D. Kurzydlowski, P. Z. -Ejgierd, W. Grochala, R. Hoffmann, Inorg. chem. **50**, 3832 (2011).

[12] Q. Zhu, D. Y. Jung, A. R. Oganov, C. W. Glass, C. Gatti, A. O. Lyakhov, Nat. Chem. **5**, 61 (2013).

[13] M. Somayazulu, P. Dera, A. F. Goncharov, S. A. Gramsch, P. Liermann, W. Yang, Z. Liu, H. -K. Mao, R. J. Hemley, Nat. Chem. **2**, 50 (2010).

[14] L. Zhu, H. Liu, C. J. Pickard, G. Zou, Y. Ma, Nat. Chem. **6**, 644 (2014).

[15] R. J. Magyar, S. Root, K. Cochrane, T. R. Mattsson, D. G. Flicker, arXiv:1410.5305v1 [cond-mat.mtrl-sci] 20 Oct 2014.

[16] U. Schwarz, K. Syassen, High. Pre. Res. **9**, 47 (1992).

[17] P. A. Agron, G. M. Begun, H. A. Levy, A. A. Mason, C. G. Jones, D. F. Smith, Science, **135** 842 (1963).

[18] R. Bersohn, J. Chem. Phys, **38**, 2913 (1963).

[19] H. Basch, J. W. Hollister, D. Hankin, J. Chem. Phys. **55**, 2913 (1971).

[20] N. J. Brassington, H. G. Edwards, J. Mol. Struct. **162**, 69 (1987).

[21] M. -S. Liao, Q. -E. Zhang, J. Phys. Chem. A **102**, 10647 (1998).

[22] B. Braïda, P. C. Hiberty, Nat. Chem. **2**, 61 (2010).

[23] U. Schwarz, K. Syassen, K. Takemura, N. E. Christensen, International Conference on High Pressure Science and Technology (Joint Conference: AIRAPT-16 & HPCJ-38), 136 (1997).

[24] S. Grimme, J. Comp. Chem. **27**, 1787 (2006).

[25] T. Bucko, J. Hafner, S. Lebègue, and J. G. Angyán, J. Phys. Chem. A **114**, 11814 (2010).

[26] T. Bucko, J. Hafner, S. Lebègue, and J. G. Angyán, Phys. Chem. Chem. Phys. **14**, 5389 (2012).

[27] S. Appalakondaiah, G. Vaitheeswaran, S. Lebègue, N. E. Christensen, A. Svane, Phys. Rev. B **86**, 035105 (2012).

[28] S. Appalakondaiah, G. Vaitheeswaran, S. Lebègue, J. Chem. Phys. **138**, 184705, (2013).

[29] S. Appalakondaiah, G. Vaitheeswaran, S. Lebègue, J. Chem. Phys. **140**, 014105, (2014)

[30] S. Appalakondaiah, G. Vaitheeswaran, S. Lebègue„ Chem. Phys. Lett. **605-606**, 10 (2014).

[31] J. P. Perdew and Y. Wang, Phys. Rev. B **45**, 13244 (1992).

[32] P. Giannozzi et al., J. Phys.:Condens. Matter 21 395502 (2009); http://www.quantum-espresso.org.

[33] T.H. Fischer, J. Almlof, J. Phys. Chem. **96**, 9768 (1992)

[34] H. J. Monkhorst and J. Pack, Phys. Rev. B **13**, 5188 (1976).

[35] X. Gonze, Phys. Rev. B **55**, 10337 (1977).

[36] F. Shimojo, Z. Wu, K. Nakano, R. K. Kalia, P. Vashishta, J. Chem. Phys. **132**, 094106 (2010).

[37] Z. Wu, R. K. Kalia, A. Nakano, P. Vashishta, J. Chem. Phys. **134**, 204509 (2011).

[38] C. -Z. Wang, R. Yu, H. Krakauer Phys. Rev. B **54**, 11161 (1996).

[39] C. Falter, M. Klenner, G. A. Hoffmann, S. Schnetgoke, Phys. Rev. B **60**, 12051 (1999).

[40] W. Zhong, D. K. -Smith, D. Vanderbilt, Phys. Rev. Lett **72**, 3618 (1994).

Chapter 5

Dispersion corrected structural properties and phase stability of energetic solids: Nitromethane and FOX-7

As seen in previous two chapters, dispersion corrected Density functional theory (DFT) methods are well accounted for predicting or reproducing the ground state properties of elemental and binary systems. Now, we further proceed to organic molecular solids in which van der Waals (vdW) as well as hydrogen bonding are more demanding, and stress the need for dispersion corrections in DFT calculations. This chapter mainly presents the results of ground state as well as high pressure structural and dynamical properties of two well known energetic materials such as ***solid nitromethane*** (CH_3NO_2) and ***FOX-7*** ($C_2H_4N_4O_4$, 1, 1 - diamino-2, 2 - dinitroethelene).

5.1 Introduction

Nitromethane and FOX-7 are primarily organic molecular solids, which belongs to the class of secondary explosives. Among the two complex solids, nitromethane is the simplest than any other energetic material, insensitive, safe to handle, used as a storable monopropellant and as an additive fuel for combustion engines. Because of its simple crystal structure compared with other secondary explosives, it has been used as a prototype material to understand the energetic materials by both experimentalists [1–10] and theoreticians [11–17]. On the other hand, FOX-

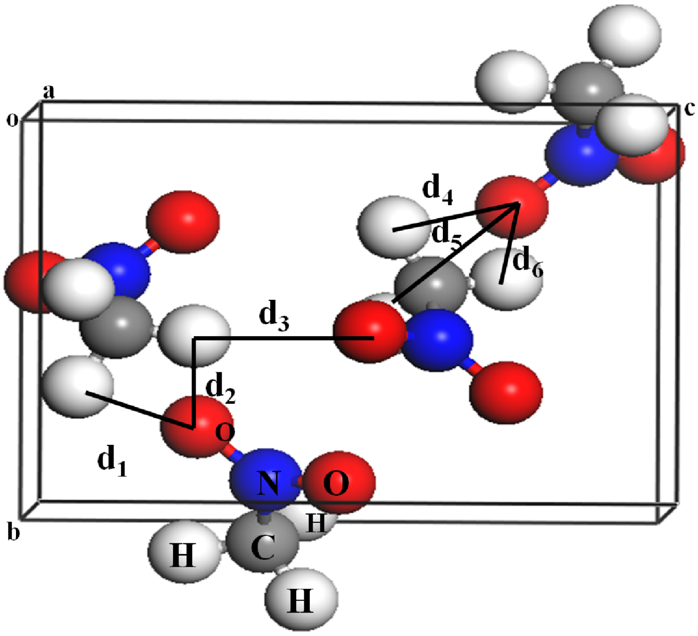

Figure 5.1: Optimized crystal structure of solid nitromethane using PBE+D2 at 0 GPa. Here d_i (i=1-6) are the different O-H bonds.

7 is a layered molecular crystal, which has generated considerable interest due to its low sensitivity and high thermal conductivity. It is also an attractive high energy material among the class of C-H-N-O based materials due to its extreme energetic characteristics such as high performance and sensitivity. For example, detonation properties of FOX-7 are compared to other well known energetic solids RDX, HMX and sensitivity is more than TATB [18, 19].

Structurally, nitromethane is liquid at room temperature, whereas it condense to form a solid at around 4.2 K. Trivero et al [1] first reported X-rays and neutron diffraction experiments, and found that solid nitromethane crystalizes in orthorhombic structure with the space group $P2_12_12_1$ as shown in Figure. 5.1 (28 atoms per unit cell). The crystal structure of FOX-7 is found to be monoclinic with the space group $P2_1/n$, which contains four molecules (56 atoms) per unit cell [20] (see Figure. 5.2). From the crystal structure of two systems, it is clearly understood that intra, inter-molecular interactions are from vdW forces as well as hydrogen bonding, and these interactions play a crucial role in determining the stability of respective structures. Earlier, Sorescu et al. [22] and Landerville et

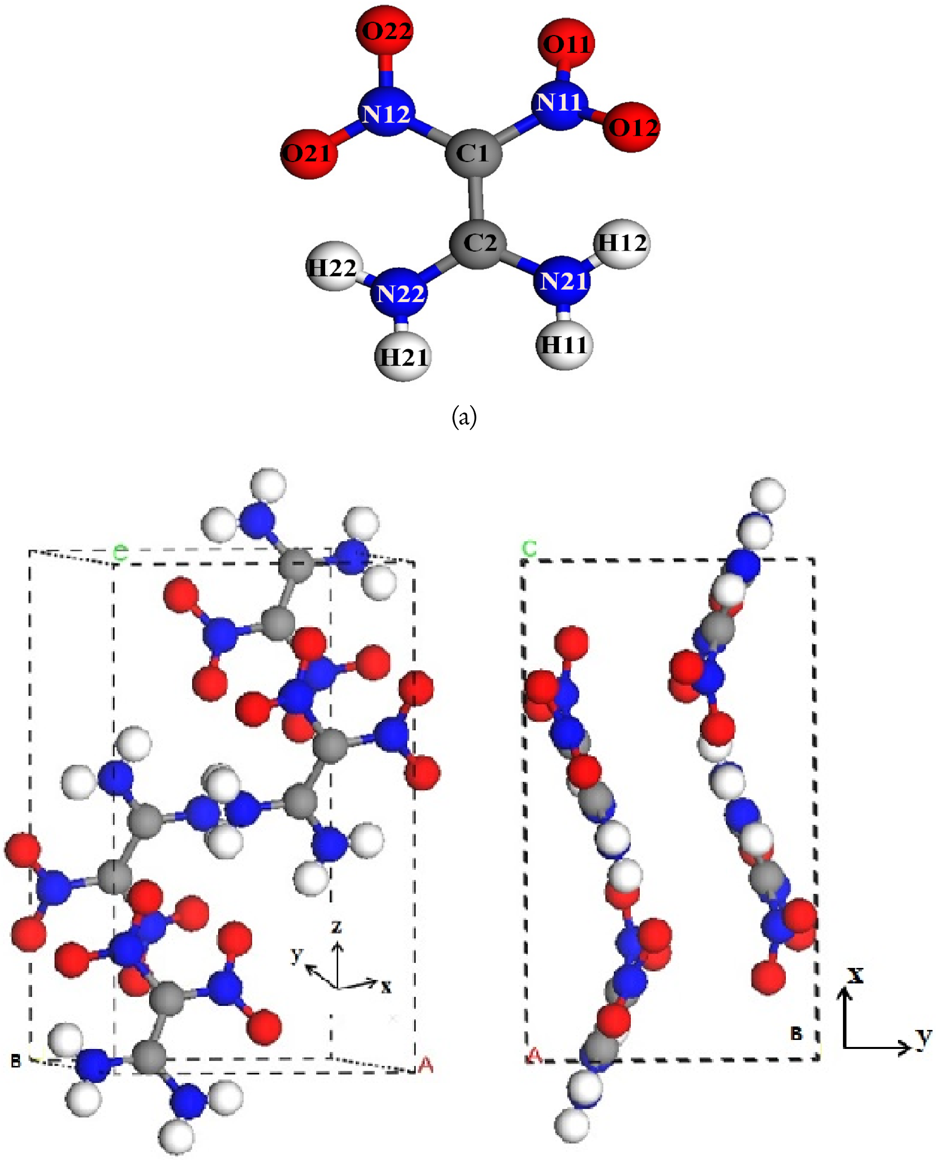

(a)

(b)

Figure 5.2: Experimental structure of FOX-7: (a) single molecule (b) complete crystal structure along different directions.

al. [23] reported the structural properties of these systems using the dispersion correction parametrization of Grimme [24] and of Neumann and Perrin. [25] approaches. In the present chapter, efforts are taken to understand the structural, vibrational properties and stability of these compounds at ambient to high pressures with the dispersion corrected DFT methods.

5.2 Computational details

The ground state properties are obtained using DFT in the Kohn - Sham formalism [26] as implemented in the CASTEP simulation package [27, 28]. Vanderbilt type ultra soft pseudo potentials [29] are used to describe the electron-nuclei interactions. Here the number of valence electrons are treated as 1 for hydrogen, 4 for carbon, 5 for nitrogen and 6 for oxygen. Similar to chapter 3, the Ceperley and Alder [30] as parameterized by Perdew and Zunger (CAPZ) in LDA [31] as well as the GGA schemes of Perdew and Wang [32] (PW91) and of Perdew-Burke-Ernzerhof [33] (PBE) for the treatment of the exchange and correlation are used. Structural optimizations were performed by minimizing the forces on each atom until they were lower then 0.03 eVÅ^{-1}. A plane wave kinetic energy cutoff of 620 eV and 540 eV were used for nitromethane and FOX-7. The Brillouin zone was sampled on a regular Monkhorst-Pack [34] grid with a minimum spacing of 0.025 Å^{-1} and 0.004 Å^{-1} for both the compounds respectively. To take into account of the vdW interactions which are generally present in molecular crystals, we have used various DFT-D methods as implemented in CASTEP. In the case of DFT-D calculations, different DFT-D approaches to treat vdW interactions were employed, notably the Ortmann, Bechstedt and Schmidt [35] (OBS) correction to PW91, as well as the Tkatchenko and Scheffler [36] (TS) and Grimme (D2) [24] corrections to PBE. Zone center vibrational properties of both the compounds were computed using linear response method within density functional perturbation theory, as implemented in the CASTEP code.

5.3 Structural properties and EOS

As a starting point of the calculations, we adopted experimental crystal structure of solid nitromethane [1] and FOX-7 [20] using various functionals mentioned above and in previous chapters. The calculated equilibrium lattice parameters, volumes and relative deviations with experimental results are presented in Table. 5.1 and 5.2 for solid nitromethane and FOX-7 respectively. We observe a large difference between our calculated values obtained with either LDA, GGA-PBE, or GGA-PW91 functional and the experimental data for both the systems. For instance, the equilibrium volume obtained with LDA ($<$ 10%) is much lower than the experimental values , while the values obtained with GGA-PW91 or GGA-PBE are overestimated more than 20 %. This inconsistency between the experimental data and the calculated results obtained with standard DFT functionals can be corrected by using the DFT+D methods: the calculated volume using the GGA functional corrected with the OBS method is underestimated by 3.2 % (for Nitromethane), 0.6% (for FOX-7), the TS method overestimates the same by 6.1 % (for Nitromethane), 2.7% (for FOX-7) while the D2 correction improves the volume to a greater extent by +1.7 % (for Nitromethane) and almost 0.1% (for FOX-7) compared with the experimental values. This clearly indicate that the various +D corrections improves the computed volume than standard DFT methods and average deviations in the volumes with experiments are not equivalent for both the compounds. Overall, the structural properties obtained with the PBE-D2 show closest agrement with experiments than any other +D correction in this chapter. Also, the present results are in agreement with previous studies using similar methods [5, 22, 23]. Therefore, for further calculations, we proceed with PBE-D2 method, along with the standard functionals LDA and PBE for comparison.

The equation of state (EoS) of solid nitromethane and FOX-7 were calculated to examine the effect of hydrostatic pressure on both lattice parameters as well as volume. In the case of nitromethane, the structural properties were computed up to 30 GPa (0-15 GPa with a step size of 2 GPa and 15-30 GPa with a step size of 5 GPa) to cover the various pressure ranges studied by different experiments. For

Table 5.1: The calculated ground state properties of solid nitromethane at zero pressure. ***a***, ***b*** and ***c*** are the lattice parameters, *V* the volume of the orthorhombic unit cell. (in parenthesis: relative deviations from experiments[1]

Method	XC	a(Å)	b(Å)	c(Å)	V(Å^3)
DFT	LDA	4.91	6.03	8.10	239.82
		(-5.3%)	(-3.3%)	(-4.9%)	(-12.9%)
	PW91	5.49	6.76	9.15	339.59
		(+5.9%)	(+8.4%)	(+7.4%)	(+23.3%)
	PBE	5.47	6.73	9.10	334.98
		(+5.5%)	(7.9%)	(+6.8%)	(+21.7%)
GGA-D	PW91-OBS	5.05	6.24	8.44	266.43
		(-2.6%)	(0.1%)	(-0.9%)	(-3.2%)
	PBE-TS	5.21	6.48	8.64	291.97
		(+0.5%)	(3.9%)	(+1.4%)	(+6.1%)
	PBE-D2	5.19	6.29	8.58	280.01
		(+0.1%)	(+0.9%)	(+0.7%)	(+1.7%)
Exp[1]		5.183	6.235	8.518	275.31

Table 5.2: The calculated ground state properties of FOX-7 at zero pressure. ***a***, ***b*** and ***c*** are the lattice parameters, *V* the volume of the orthorhombic unit cell. (in parenthesis: relative deviations from experiments [20]

Method	XC	a(Å)	b(Å)	c(Å)	B	V(Å^3)
DFT	LDA	6.75	6.21	11.05	90.62	462.51
		(-2.7%)	(-5.5%)	(-2.3%)	(0.1%)	(-10.3%)
	PW91	7.24	7.88	11.63	92.14	662.45
		(4.3%)	(19.96%)	(2.8%)	(1.7%)	(28.4%)
	PBE	7.23	7.78	11.65	92.02	654.22
		(4.3%)	(18.43%)	(2.9%)	(1.6%)	(26.8%)
GGA-D	PW91-OBS	6.93	6.56	11.29	90.98	512.65
		(-0.2%)	(-0.1%)	(-0.2%)	(0.5%)	(-0.6%)
	PBE-TS	6.99	6.66	11.38	91.41	529.64
		(0.7%)	(1.4%)	(0.6%)	(0.9%)	(2.7%)
	PBE-D2	6.99	6.52	11.31	91.23	515.45
		(0.7%)	(-0.7%)	(0.0%)	(0.7%)	(-0.1%)
Exp[20]		6.941	6.569	11.315	90.55	515.89

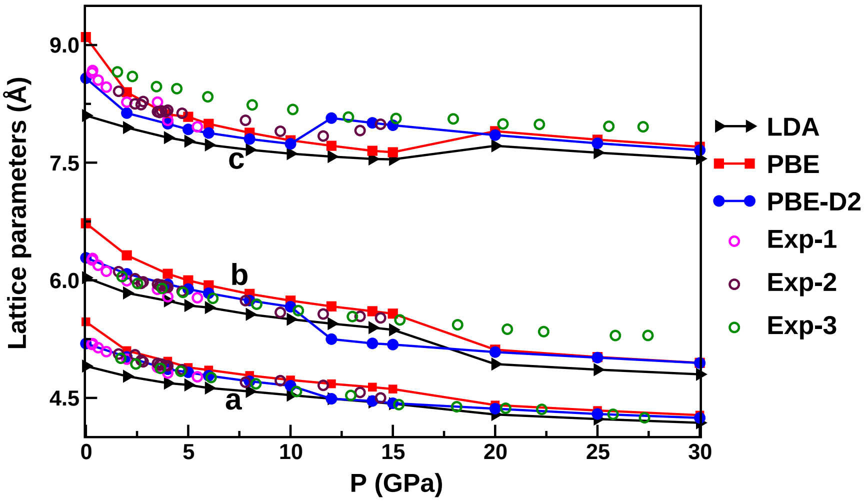

Figure 5.3: Hydrostatic pressure dependence of lattice parameters properties of solid nitromethane up to 30 GPa as calculated within LDA, GGA with PBE, and PBE-D2, compared to experiments (Exp1: Ref. 3, Exp2: Ref. 4:, Exp3: Ref. 5). Here, (a). Pressure dependence of ***a***, ***b***„ and ***c*** -lattice parameters , (b). crystal volume.

FOX-7, the EOS was calculated in a pressure range from 0-10 GPa with a step size of 0.5 GPa between 0-5 GPa and step size of 1 GPa for 5-10 GPa pressures. The variation in the lattice constants (a, b, and c) as well as volume for both the compounds are compared with experiments and are illustrated in Figure. 5.3, 5.4, 5.5, and 5.6

In the case of nitromethane, at low pressure the D2 correction to PBE is essential to reproduce the experimental values, whereas at large pressures the three computed methods show consistent results, which mainly implies that at high pressures the long-range vdW forces become less important. Moreover it is seen that , a sudden change in the lattice parameters occurs between 10 GPa to 12 GPa using PBE-D2 functional, the similar situation was observed in the lattice parameters ***a*** and ***b*** decreases with increasing pressure, whereas ***c*** lattice parameter increases with pressure. A similar behavior is observed with the LDA and PBE functionals, although it happens at higher pressure (between 15 GPa to 20 GPa). This will be discussed in subsequent sections. Figure. 5.4 shows our calculated pressure-volume relation up to 30 GPa and the same are compared with experi-

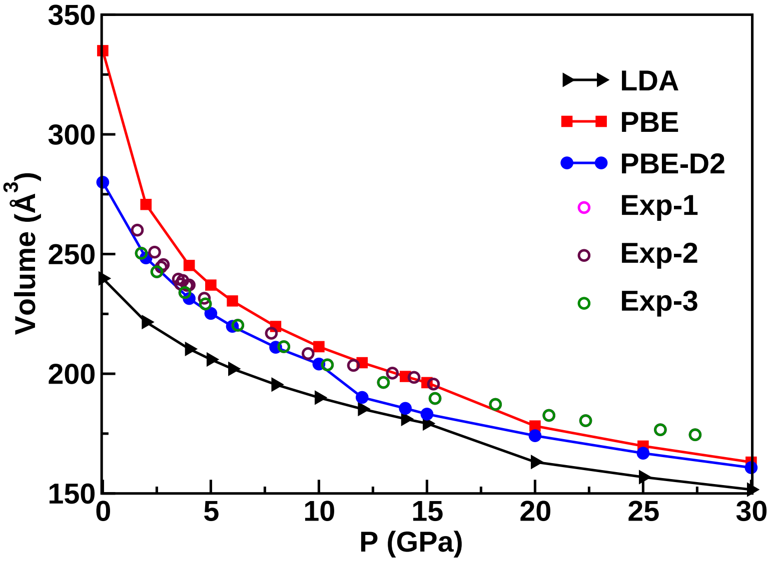

Figure 5.4: Hydrostatic pressure dependence of volume of solid nitromethane up to 30 GPa as calculated within LDA, GGA with PBE, and PBE-D2, compared to experiments (Exp1: Ref. 3, Exp2: Ref. 4:, Exp3: Ref. 5). Here, (a). Pressure dependence of ***a***, ***b***,, and ***c*** -lattice parameters , (b). crystal volume.

ments. The calculated bulk modulus and its pressure derivative obtained with the PBE-D2 functional are B = 11.6 GPa and B' = 6.5 respectively, which is in good agreement with experimental values of 7 GPa [3], 10.1 GPa [4], 9.25(±1.9) GPa[5] and closely comparable with the reported theoretical values of 5.7 GPa [11, 16] with standard DFT method.

On the other hand, FOX-7 clearly highlights the fact that van der Waals interaction becomes more important under large pressure. The deviation of our calculated lattice parameters from 0 GPa and 4 GPa are compared available experiments are listed in Table 5.3. By comparing the three lattice parameters, the reduction of the ***b*** lattice parameter under pressure is larger than the other two parameters as clearly observed from the first order pressure coefficients ($\gamma = \frac{1}{X}\frac{dX}{dP}$, X=$a$, b, c). The calculated pressure coefficients obtained with either LDA, PBE and GGA+D2 are presented in Table 5.4, following an order of b> c> a with all the three methods. This clearly implies that FOX-7 having the largest compressibility along the b-axis and the same was reported experimentally [21]. Then, the

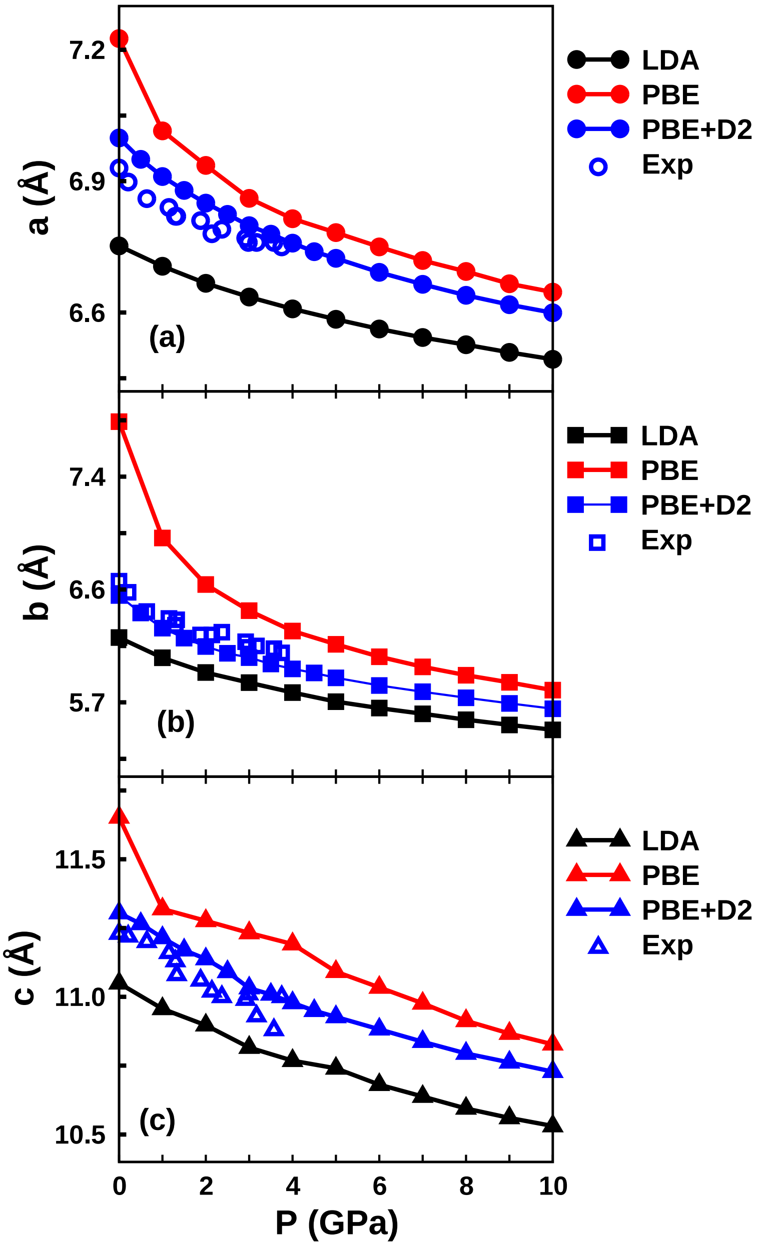

Figure 5.5: Hydrostatic pressure dependence of lattice parameters (*a*, *b*, and *c*) and crystal volume of FOX-7 up to 10 GPa as calculated within LDA, PBE, and PBE-D2 and as compared with experiments [21].

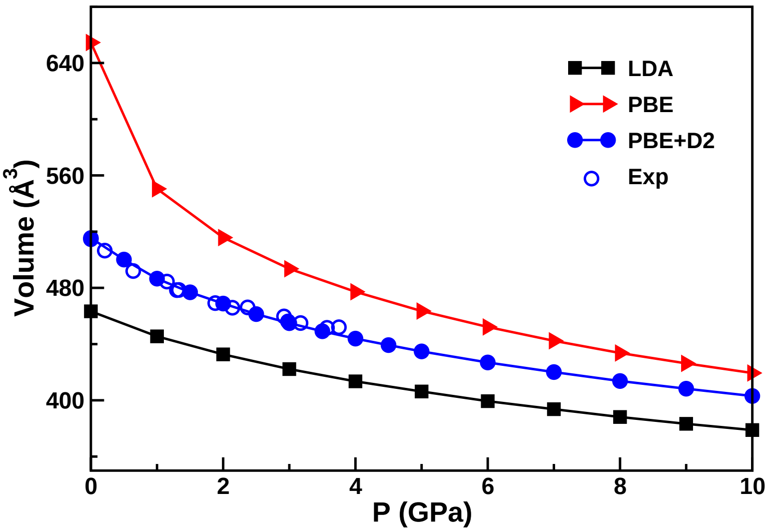

Figure 5.6: Hydrostatic pressure dependence of crystal volume of FOX-7 up to 10 GPa as calculated within LDA, GGA with PBE, and PBE-D2 and as compared with experiments [21].

Table 5.3: The deviation of the lattice parameters (in Å) of monoclinic FOX-7 at 0 GPa and 4 GPa with experiments. Here '-' sign indicates an underestimation and '+' indicates an overestimation in comparison with experimental values

XC	at 0 GPa			at 4 GPa		
	a	b	c	a	b	c
LDA	-0.18	-0.41	-0.19	-0.17	-0.28	-0.15
PBE	+0.30	+1.16	+0.42	+0.05	+0.17	+0.27
GGA+D2	+0.07	-0.10	+0.07	+0.01	-0.11	+0.06

Table 5.4: The calculated first order pressure coefficients(in 10^{-3} GPa^{-1}) of the lattice parameters and second order bulk moduli (in GPa) of monoclinic FOX-7.

XC	a	b	c	B
LDA	-3.9	-9.3	-7.6	31.26
PBE	-7.9	-19.8	-12.2	8.13
GGA+D2	-3.4	-6.3	-5.0	18.43

EoS of FOX-7 is determined by fitting the obtained P-V data (see Figure 5.6) to a second order Birch-Murnaghan (B-M) EoS, . We found that the bulk moduli (see Table 5.4) obtained within LDA or GGA is in poor agreement with experiments, while the one obtained with PBE+D2 is in very good agreement with the experimental value of 17.6 GPa [21].

5.4 Bonding and Vibrational properties

5.4.1 Solid Nitromethane

As mentioned earlier, in order to understand the sudden change in the lattice parameters of solid nitromethane, we have calculated the pressure dependence of bond lengths, bond angles, and the corresponding data are shown in Figure. 5.7 and 5.8. The change observed in the lattice parameters is also reflected in the bond lengths and bond angles. In particular, when hydrostatic pressure is increased from 0 GPa to 10 GPa with the PBE-D2 functional, the bond lengths C-N, N-O_i (i=1,2), O-H_i (i=1,6) and the bond angle O_1-N-O_2 decreases significantly but in contrast, the C-N-O_i (i=1,2) bond angles increases with pressure. However in the pressure region from 10 GPa to 12 GPa, an increase in the N-O_2 bond length is observed together with a sudden change in the C-N-O bond angles.

Also, the O-H distances (see Figure. 5.8) d_1, d_3 and d_6 are in the range of 2.2 Å to 3.2 Å at ambient pressure, whereas these values decreases to 2.0 Å to 2.6 Å at high pressures and weakening of hydrogen bond strength is observed between the pressure range of 10 to 12 GPa. This behavior indicates slight changes in the hydrogen bonding and more generally in the intermolecular geometry of solid nitromethane. Snap shots of the unit cell of solid nitromethane for differ-

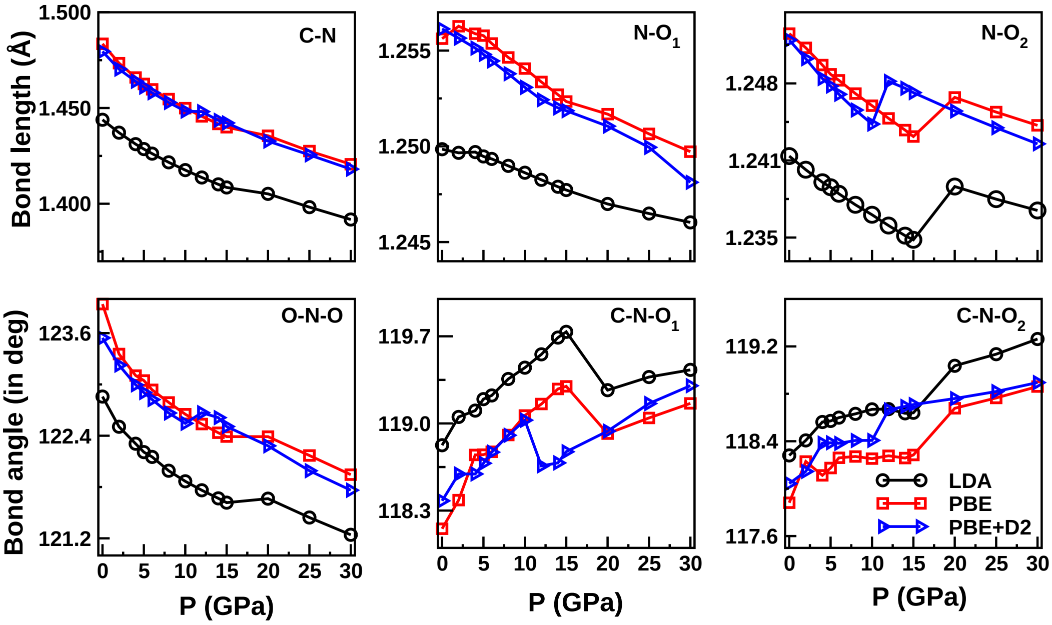

Figure 5.7: Bond lengths and bond angles of solid nitromethane up to 30 GPa as calculated within LDA, PBE, and PBE-D2.

ent pressures are shown in Figure. 5.9 . Indeed this indicates a possible phase transition in solid nitromethane,from Phase I to Phase II known experimentally [5] to occur at 11 GPa. In the present calculations using PBE+D2 method, the transition pressure is slightly lower than experiment, but the overall agreement is found to be good. Of course a similar situation is observed with the LDA and PBE functionals between 15 to 20 GPa, which emphasis the inclusion of +D2 correction to the DFT method. To have better understanding on the phase stability of nitromethane, further calculations of vibrational frequencies at the gamma point were continued with PBE+D2 approach.

Since the unit cell of solid nitromethane contains 28 atoms, the corresponding number of modes are 84, of which 3 are acoustic modes and remaining 81 modes are optical modes. The optical modes at the Brillouin zone center (Γ point) have the following irreducible representation:

$$A(R) + B_1(R + IR) + B_2(R + IR) + B_3(R + IR) \tag{5.1}$$

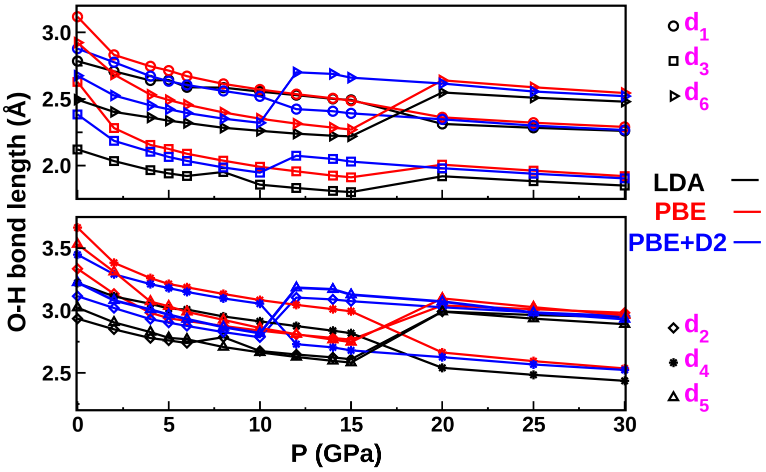

Figure 5.8: Oxygen-hydrogen bond lengths of solid nitromethane up to 30 GPa as calculated within LDA, PBE, and PBE-D2.

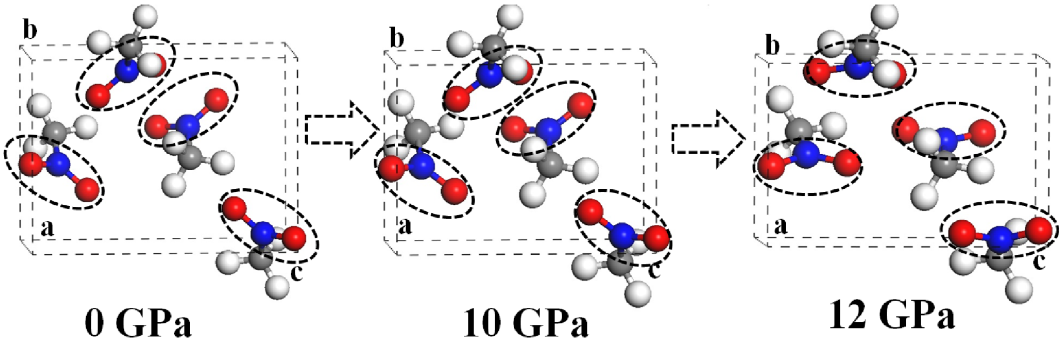

Figure 5.9: Snap shots of solid nitromethane unit cells using PBE+D2 at 0 GPa, 10 GPa and 12 GPa. The circles shows the orientation of C-N-O bond angle with pressure.

Table 5.5: Vibrational frequencies (in cm^{-1}) of the internal modes of solid nitromethane. All quantities are calculated at the respective theoretical equilibrium volume using the PBE+D2 functional. Here A(R), B_1(R+IR), B_2(R+IR) and B_3(R+IR) are irreducible representation of space group $P2_12_12_1$.

no.	Mode	Irr rep	Cal. fre	Ass.	Exp[8]	other[16]
1		B_1	3127.8			
2	M1	B_2	3127.3	CH_3 An.St	3082.2 (B_2)	3117
3		B_3	3126.5			
4		A	3126.3			
5		B_2	3082.7			
6	M2	B_1	3081.6	CH_3 An.St.	3049.6 (B_3)	3072
7		B_3	3081.2			
8		A	3080.9			
9		B_2	2983.1			
10	M3	B_1	2981.8	CH_3 Sy.St		2980
11		B_3	2981.4			
12		A	2981.0		2970.6 (A)	
13		B_3	1483.1		1566.0 (B_3)	
14		B_1	1480.1	CH_3 Wa +		
15	M4	B_2	1479.2	NO_2 An.St	1565.4 (B_2)	1528
16		A	1456.3			
17		B_1	1434.5			
18	M5	B_3	1429.3	CH_3 De +	1429.6 (B_3)	
19		B_2	1419.1	NO_2 An.St	1430.9 (B_2)	1434
20		A	1418.6			
21		B_2	1406.9		1414.1 (B_2)	
22		B_1	1396.6	CH_3 De +	1412.7 (B_1)	
23	M6	B_3	1384.1	NO_2 Sy. St	1413.6 (B_3)	1414
24		A	1381.3		1412.0 (A)	
25		B_2	1371.4		1414.7 (B_2)	
26	M7	B_1	1368.2	CH_3 De +		
27		B_3	1360.6	NO_2 Sy. St		1387
28		A	1356.0		1403.9 (A)	(cont..)

Table 5.6: Cont.. vibrational frequencies (in cm^{-1}) of the internal modes of solid nitromethane.

29	M8	B_2	1310.3	CH_3 Wa + NO_2 S + CN St	1376.5 (B_2)	1342
30		B_3	1310.1		1378.2 (B_3)	
31		B_1	1308.2		1379.3 (B_1)	
32		A	1307.9		1375.4 (A)	
33	M9	B_2	1095.4	NCH De	1120.1 (B_2)	1098
34		B_1	1090.5		1121.2 (B_1)	
35		B_3	1089.5		1124.3 (B_3)	
36		A	1088.3			
37	M10	B_3	1076.7	CH_3 Tw + NO_2 An. St	1108.2 (B_3)	1083
38		A	1075.5		1105.3 (A)	
39		B_2	1073.5		1107.1 (B_2)	
40		B_1	1070.7		1106.1 (B_1)	
41	M11	A	890.1	CN St + NO_2 Be	923.6 (A)	906
42		B_2	889.9		923.8 (B_2)	
43		B_1	889.1		922.0 (B_1)	
44		B_3	888.9			
45	M12	B_1	641.5	CN St + NO_2 Sc	658.0 (B_1)	650
46		B_2	641.1		664.4 (B_2)	
47		B_3	641.0			
48		A	636.3			
49	M13	B_1	592.4	NCH Wa + NO_2 An. St	610.1(B_1)	601
50		B_2	591.4		608.0 (B_2)	
51		B_3	587.3		607.7 (B_3)	
52		A	585.9			
53	M14	B_2	472.7	NO_2 Ro	484.1 (B_2)	472
54		A	470.9		484.9 (A)	
55		B_3	470.6		484.0 (B_3)	
56		B_1	470.3		483.7 (B_1)	

Here, St: stretching; An. St: Antisymmetric stretching; Sy. St: Symmetric stretching; Wa: Wagging; De: Deformation; Tw: Twisting; Be: Bending; Sc: Scissor; Ro: rocking

Table 5.7: Vibrational frequencies (in cm^{-1}) of the external modes of solid nitromethane. All quantities are calculated at the respective theoretical equilibrium volume using the PBE+D2 functional. Here A(R), B_1(R+IR), B_2(R+IR) and B_3(R+IR) are irreducible representation of space group $P2_12_12_1$.

no.	Mode	Irr rep	Cal. fre	Exp[8]
57		A	180.9	
58		B_2	171.1	165.4(B_2)
59		B_1	162.0	
60	L1	B_3	161.4	
61		A	153.6	154.9(A)
62		B_2	148.5	
63		B_3	145.7	
64	L2	B_1	132.9	138.8(B_1)
65		B_3	116.1	114.6(B_3)
66		B_1	113.0	
67	L3	B_2	107.7	
68		A	106.3	112.9(A)
69		B_3	100.5	
70		B_2	97.6	95.1 (B_2)
71	L4	B_1	91.2	99.7(B_1)
72		B_3	90.5	85.0(B_3)
73		A	84.4	84.5(A)
74		B_1	73.1	78.2(B_1)
75		B_2	71.6	71.5(B_2)
76	L5	A	70.1	70.7(A)
77		A	66.1	58.6(A)
78		B_3	62.7	
79		A	53.7	52.1(A)
80	L6	B_2	51.8	44.4(B_2)
81		B_1	44.1	

Here R and IR represents the Raman active and infrared active modes respectively. Table 5.5, 5.6, 5.7 presents the calculated internal and external modes for +D2 calculations, with the corresponding mode assignment and are compared with earlier experimental and other theoretical results. By following the previous notation, the high energy domain(> 400 cm^{-1}) contains 14 internal modes, where, each mode is grouped into four set of symmetries. These modes are indexed going from highest energy mode M1 (CH_3 antisymmetric stretching) to the lowest energy mode M14 (NO_2 rocking). The main features of the internal modes are as follows: (1) The higher frequency modes M1, M2 and M3 are mainly from CH_3 stretching, (2) optical modes M5 to M8 are due to CH_3 deformation and NO_2 stretching, (3) NCH deformation is observed in mode M9, (4) mixed motions are observed in M10 to M13, which are from NO_2, CH_3 and CN bonds (5) M14 mode is mainly from the NO_2 rocking. The calculated internal modes differ by few cm^{-1} when compared with earlier reported GGA-PBE calculated frequencies [16]. This is mainly due to +D2 correction to PBE which improved the volume compared to the results without inclusion of vdW and thereby intermolecular distance varies considerably. The low energy domain(< 400 cm^{-1}) consists of 25 fundamental external (lattice) modes, namely $7A+6B_1+6B_2+6B_3$. The internal and external modes are separated by 292.6 cm^{-1}, which is in good agrement with experimental gap of 289.2 cm^{-1}. Overall, the calculated external and internal modes are in good agrement with experiments [8–10].

Now, we discuss the pressure dependence of the vibrational frequencies of solid nitromethane. Figure. 5.10 shows the frequency of the internal modes as a function of pressure up to 30 GPa (with a step size of 5 GPa). It is observed that the frequencies of all the internal modes increases with external pressure. However, in the pressure ranges of 10 GPa to 15 GPa, a large discontinuity is noticed for the vibrational modes M2, M3, M4, M7 and M8. From Table 5.5, 5.6, it is found that the mentioned modes are from CH_3 and NO_2 stretching at ambient conditions and hydrostatic compression shows significant effect on CH_3 and NO_2 groups. A similar behavior has been observed from 9 to 13 GPa in the experiments using Raman measurements [8–10]. The variation of lattice modes under pressure are shown in Figure. 5.11. From this, we can clearly see that the

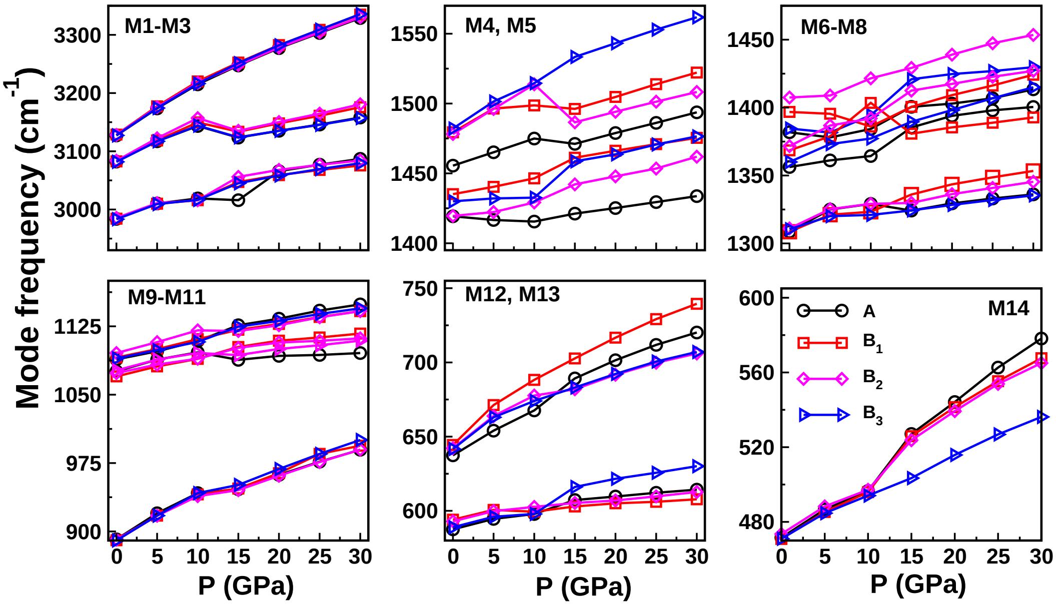

Figure 5.10: Pressure evolution of internal vibrational frequencies of solid nitromethane up to 30 GPa using PBE-D2 at Gamma point.

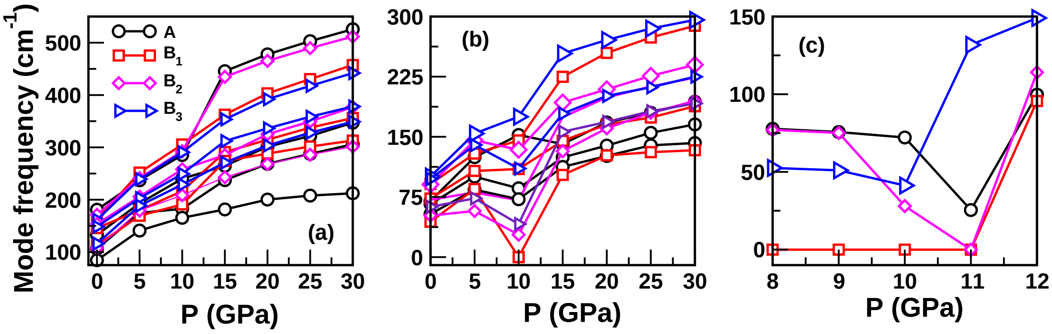

Figure 5.11: Calculated L1-L3 (a), L4-L6 (b) external vibrational frequencies of solid nitromethane at Gamma point up to 30 GPa (step size of 5 GPa) within PBE-D2 and (c) shows the L6 mode frequencies from 8 GPa to 12 GPa with a step size of 1 GPa.

calculated lattice modes from L1 to L3 (Figure. 5.11(a)) are hardening with increasing pressure, whereas L4 to L6 modes(Figure. 5.11(b)) starts to soften from 5 GPa to 10 GPa. As the pressure increases from 10 GPa, all these modes(L4 to L6) shift towards higher frequencies. However in the pressure region 8 to 10 GPa, B_1 modes decreases to zero and are shown in Figure. 5.11(c). Overall, the calculated vibrational frequencies at high pressure using PBE-D2 functional shows distinct intra and intermolecular modes at high pressures and the discontinuity in the internal and lattice modes point out to the structural transition in solid nitromethane between 10 to 12 GPa at low temperatures which is in good agreement with the available experimental data [5, 9]. From 15 to 30 GPa, all the internal modes increases continuously without any discontinuity, in good agreement with earlier experiments. Also, by increasing the pressure the energy gap between the internal and the external modes decreases to 30 cm^{-1}, which is also comparable with previous experiment.

5.4.2 FOX-7

From the crystal structure of FOX-7 (see Figure. 5.2), it is clearly clearly seen that the intra as well as inter molecular interactions of FOX-7 molecules were together with vdW forces between the layers and strong hydrogen bonding due to the close contact of the NH_2 group of one molecule with the NO_2 group of the adjacent molecule. Also, recent experiments under pressure reported that variations in the hydrogen bond strength, leads to solid-solid phase transitions of FOX-7 [37, 38]. To confirm the nature of hydrogen bonding under hydrostatic pressure, we have proceeded with the investigation of the intra- as well as inter- molecular N-H...O hydrogen bonds and the IR spectra of FOX-7 under pressure. The intra and inter molecular Donor (Nij)- Hydrogen (Hij), Acceptor (Oij)- Hydrogen (Hij) and Acceptor (Oij)- Donor (Nij) bond lengths (here ij notations are defined in Figure. 5.2(a)) under pressure are shown in Figure. 5.12. All the intramolecular N-H bond lengths (shown in Figure. 5.12(a)) decreases except N21-H11. The bond length variations for O-H and N-H are shown in Fig 5.12(b) and Figure. 5.12(c) respectively. Also the O-H and N-O bonds between adjacent molecules are found to decrease drastically with pressure and some of the O-H bond lengths are found to be shorter than the sum of their vdW radii. This indicates a large variation in the intermolecular interactions and affects the strength of hydrogen bonding in FOX-7. The signature of hydrogen bond was observed from IR spectra in two cases previously [39, 40]. In the first case, the red shift of the hydrogen bond in N-H...O is from N-H bond length hardening with an associated decrease in the N-H stretching frequency and accompanied by an increase of the IR intensity [39]. In the second case, the blue shifted hydrogen bond results from the shortening of the N-H bond lengths, and an increase in stretching frequency of NH group with decrease in IR intensity [40]. To understand the nature of IR spectra for FOX-7, further calculations on IR spectra of FOX-7 were performed an are presented in this chapter. The unit cell contains 56 atoms and has therefore a total of 168 (3 acoustic + 165 optical) modes. The optical modes have the following irreducible representation:

$$A_g(R) + B_g(R) + A_u(IR) + B_u(IR) \tag{5.2}$$

Here A_g, B_g modes have inversion symmetry and are Raman active; A_u, B_u are IR active due to change of sign under inversion symmetry. The main characteristics of optical modes are the following: the lower frequencies from 22 to 470 cm^{-1} are external modes, i.e. vibration from all the atoms in unit cell, (a) The internal modes from 530-713 cm^{-1} corresponds to wagging and rocking motion of the NH_2 group (b) Mixed motions from the NH_2, NO_2, C-N groups stretching and N-C-N rotations are observed between 713-832 cm^{-1}, (c) Individual NH_2 group rocking is found from 1006-1053 cm^{-1}, (d) The modes between 1104-1605 cm^{-1} corresponds to NO_2 stretching, NO_2 bending and C-C stretching (e) the very high frequencies (more than 3200 cm^{-1}) are from NH_2 symmetric and asymmetric stretching modes. The calculated IR spectra from 0 to 10 GPa, is shown in Figure. 5.13. According to our calculated IR spectra, we found that all internal modes from 530-1006 cm^{-1} are shifted towards higher frequencies with increasing pressure. On the contrary, the modes above 3200 cm^{-1} , are shifted to lower values with increasing pressure.

The enhancement of intermolecular N22-H11 bond strength, decrement of

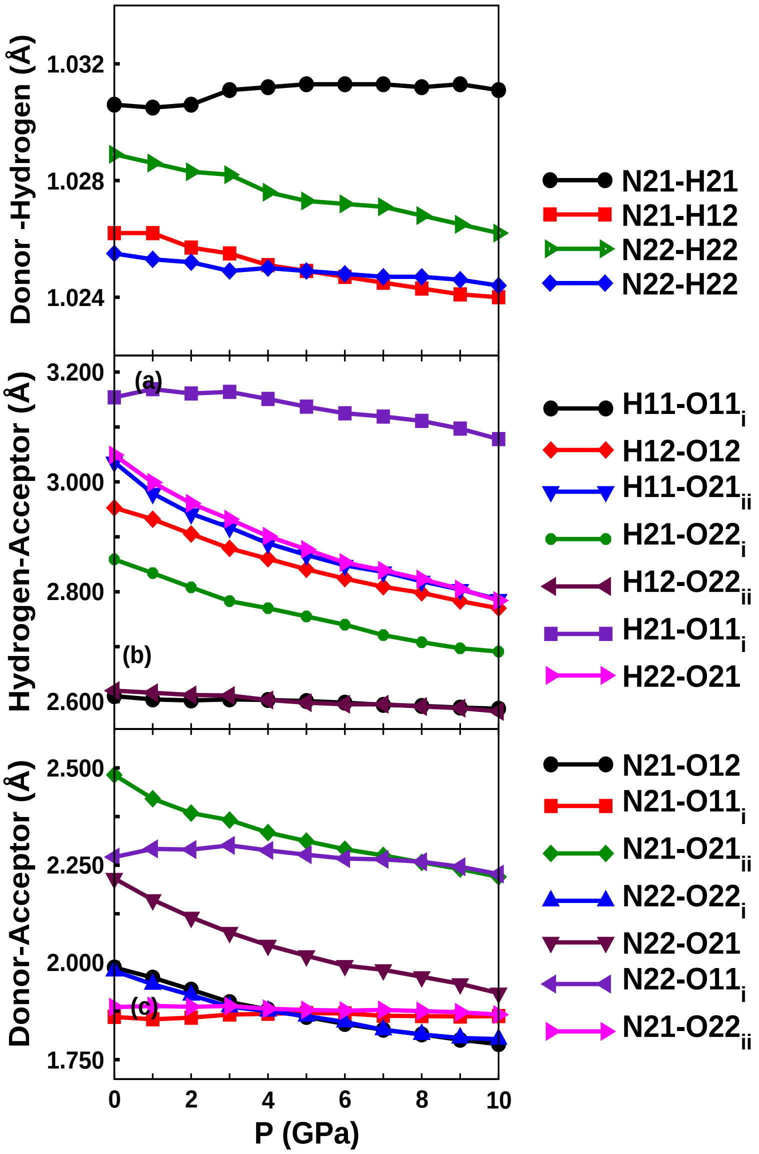

Figure 5.12: Calculated pressure dependence of inter- and intramolecular hydrogen bond lengths of FOX-7, (a). Donor-Hydrogen, (b). Acceptor-Hydrogen and (c). Acceptor-Donor. Note the different set of bond lengths were taken from experimental notation [20].

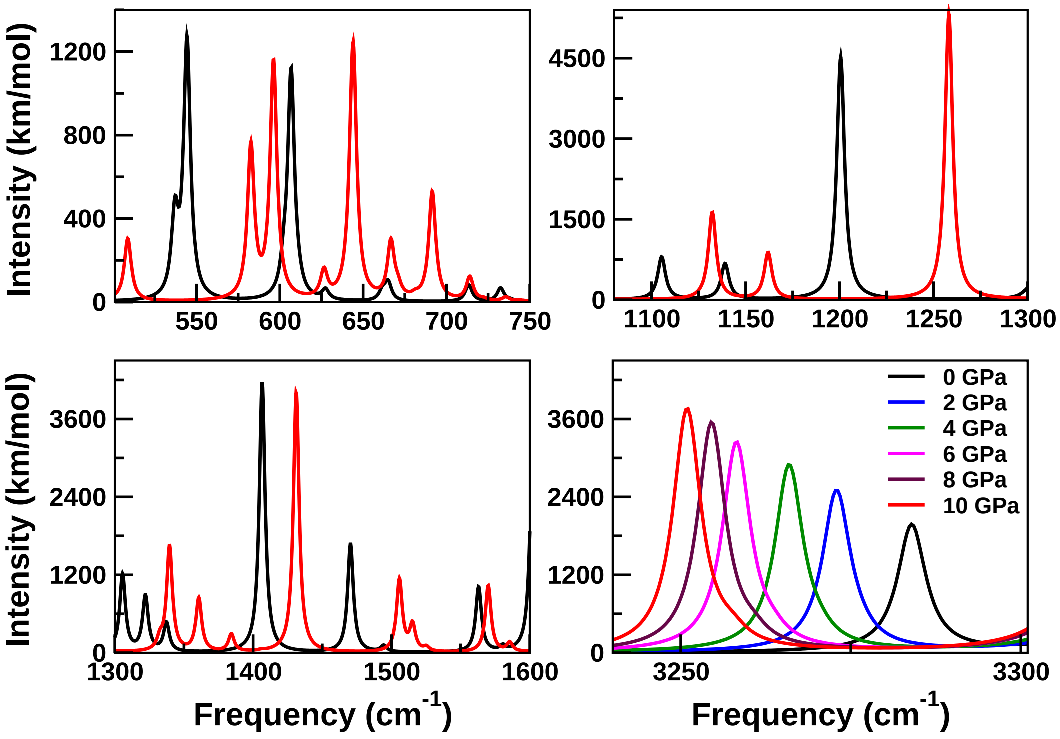

Figure 5.13: IR spectra of FOX-7 under hydrostatic pressure range from 0 to 10 GPa.

mid-IR region (above 3000 cm^{-1}) frequencies under hydrostatic pressure conditions illustrates the strengthening of intermolecular bond strength.

5.5 Transition from α to t α' structure in FOX-7

Starting from the synthesis of this compound in 1998 [41], several studies were carried out on FOX-7 to investigate its structural properties from ambient[20] to extreme conditions [21, 42, 43, 45]. Beeman and Ostrak [20] determined the crystal structure of FOX-7 to be monoclinic with the space group P2$_1$/n, which contains four molecules (56 atoms) per unit cell. Later Peris et al [21] studied its structural properties and Raman spectra under the influence of non-hydrostatic pressure and found a quasi-amorphous phase above 4.5 GPa. However, they found that no lattice transformations could be observed up to 8 GPa under hydrostatic conditions. Recent experiments at different temperatures and pressures found three possible phase transitions (at 2 GPa, 5 GPa and above 10 GPa) in mid and far IR regions [37, 38]. Pravica et al [37] reported the strengthening of the hydrogen bond and softening of NH_2 stretching frequencies at high pressure by using IR experiments. Very recently, Dreger et al [48] studied Raman spectra under isothermal compression (up to 15 GPa) and isobaric heating (up to 500K), and claimed that two phase transitions are observed at 2 and 4.5 GPa respectively. Apart from this, FOX-7 has shown three (possibly four) solid polymorphic phases as a function of temperature [42–44]. The α phase (monoclinic, $P2_1/n$, $Z=4$) appears to be most stable under ambient conditions, and it transforms to β phase (orthorhombic, $P2_12_12_1$, $Z=4$) beyond 378 K at ambient pressure and further transforms to γ phase (monoclinic, $P2_1/n$, $Z=8$) upon heating above 448 K. Experiments also indicate a phase transition from α to α' phase at pressure around 2 GPa [37, 38], (the α' phase was considered to be identical to the β phase of FOX-7 found previously at 373 K). In contrast to this, recent experiment using isothermal compression (at 298 K) found a phase transition at the same pressure but they claimed that the structure was different from the β structure [48]. With the aim to have a better understanding of this phase transition, calculations for enthalpy differences were computed for the both α and β phases taking into account Grimme's correction for vdw interactions. However, the present results didn't observe any sign of a possible transition, and the α phase stayed with the lowest enthalpy for the range of pressures that we have investigated. It is also be noted that the presented calculations are within hydrostatic pressure limit performed at 0 K. Therefore, present computations anticipate that temperature might certainly play a major role during the transition, and/or that the level of theory (dipole-dipole correction) that are used to take into account the dispersive interactions in the present computations are might not be sufficient, leading to the discrepancies observed between experiments and theoretical results.

5.6 Conclusions

In summary, the present chapter provides the detailed investigation of the structural properties of solid nitromethane and FOX-7 within LDA, GGA and different dispersion corrections including with GGA functional to treat vdW forces. It was found that the structural properties using PBE-D2 are in good agreement with experiments, which highlight the role of vdW interactions in solid nitromethane. Subsequently, the influence of hydrostatic pressure on the structural properties such as the lattice parameters, bond lengths, and bond angles was calculated for nitromethane and a discontinuity in bond lengths and bond angles was observed between 10 GPa to 12 GPa. In particular, solid nitromethane is stiffest along the crystallographic a-axis, followed by the b-axis, and then by the c-axis. The vibrational properties of solid nitromethane at ambient conditions have been calculated and a fairly good agrement with experiments is obtained. The influence of hydrostatic pressure on solid nitromethane shows distinct behavior from 8 to 15 GPa. The weakening of hydrogen bond strength, softening of lattice modes supports a possible structural transition in solid nitromethane between 8 to 12 GPa and this was in excellent agreement with reported experiments. On the other hand the computed lattice parameters of FOX-7 at high pressures shows a large compressibility along the b-axis, which is also similar with available experiments. The vibrational properties computed under pressure shows a large contribution of intermolecular interactions taking place up to 10 GPa and demonstrate an evidence of strong hydrogen bonding in the mid IR region. It is also found that ground state FOX-7 could be structurally stable under hydrostatic pressure up to 10 GPa.

References

[1] S. F. Trevino, E. Prince and C. R. Hubbard, J. Chem. Phys., **73**, 2996 (1980).

[2] J. M. Seminario, M. C. Concha and P. Politzer, J. Chem. Phys., **102**, 8281 (1995).

[3] Don T. Cromer, Robert R. Ryan and David schifel, J. Phys. Chem., **89**, 2315-2318 (1985).

[4] F. L. Yarger and B. Olinger, J. Chem. Phys., **85**, 1534 (1986).

[5] M. Citroni, F. Datchi, R. Bini, M. Di Vaira, P. Pruzan, B. Canny and V. Schettino, J. Phys. Chem. B, **112**, 1095-1103 (2008).

[6] P. J. Miller, S. Block and G. J. Piermarini, J. Phys. Chem., **93**, 462-466 (1989).

[7] J. R. Hill, D. S. Moore, S. C. Schmidt and C. B. Strom, J. Phys. Chem., **95**, 3037-3044 (1991).

[8] R. Ouillon, J.-P. Pinan-Lucarre, P. Ranson and G. Baranovic, J. Chem. Phys., **116**, 4611 (2002).

[9] J.-P. Pinan-Lucarre, R. Ouillon, B. Canny, Ph. Pruzan and P. Ranson, Journal of Raman Spectroscopy, **34**, 819 (2003).

[10] R. Ouillon, J.-P. Pinan-Lucarre, B. Canny, Ph. Pruzan and P. Ranson, Journal of Raman Spectroscopy, **39**, 354 (2008).

[11] D. C. Sorescu, B. M. Rice and D. L. Thompson, J. Phys. Chem. B, **104**, 8406 (2000).

[12] D. C. Sorescu, B. M. Rice and D. L. Thompson, J. Phys. Chem. A, **105**, 9336 (2001).

[13] P. M. Agarwal, B. M. Rice and D. L. Thompson, J. Chem. Phys., **119**, 9617 (2003).

[14] E. F. C. Byrd, G. E. Scuseria and C. F. Chabalowski, J. Phys. Chem. B, **108**, 13100 (2004).

[15] E. J. Reed, J. D. Joannopoulos and L. E. Fried, Phys. Rev. B, **62**, 16500 (2000).

[16] H. Liu, J. Zhao, D. Wei and Z. Gong, J. Chem. Phys., **124**, 124501 (2006).

[17] Frank J. Zerilli, Joseph P. Hooper and Maija M. Kuklja, J. Chem. Phys., **126**, 114701 (2007).

[18] D. Mathieu, J. Phys. Chem. A, **116**, 1794 (2012).

[19] M. Anniyappan, M. B. Talawar, G. M. Gore, S. Venugopalan and B. R. Gandhe, J. Hazard. Mater., **137**, 812 (2006).

[20] U. Bemm and H. Ostmark, Acta. Cryst. C, **54**, 1997 (1998).

[21] S. M. Peiris, C. P. Wong and F. J. Zerilli, J. Chem. Phys., **120**, 8060 (2004).

[22] D. C. Sorescu and B. M. Rice, J. Phys. Chem. C, **114**, 6734 (2010).

[23] A. C. Landerville, M. W. Conroy, M. M. Budzevich, Y. Lin, C. T. White and I. I. Oleynik, Appl. Phys. Lett., **97**, 251908 (2010).

[24] S. Grimme, J. Comp. Chem., **27**, 1787 (2006).

[25] A. Neumann and M.-A. Perrin, J. Phys. Chem. B, **109**, 15531 (2005).

[26] W. Kohn and L. J. Sham, Phys. Rev., **140**, A1133 (1965).

[27] M. C. Payne, M. P. Teter, D. C. Allan, T. A. Arias and J. D. Joannopoulos, Rev. Mod. Phys., **64**, 1045 (1992).

[28] M. D. Segall, P. J. D. Lindan, M. J. Probert, C. J. Pickard, P. J. Hasnip, S. J. Clark and M. C. Payne, J. Phys. Cond. Matt., **14**, 2717 (2002).

[29] D. Vanderbilt, Phys. Rev. B, **41**, 7892 (1990).

[30] D. M. Ceperley and B. J. Alder, Phys. Rev. Lett., **45**, 566 (1980).

[31] J. P. Perdew and A. Zunger, Phys. Rev. B, **23**, 5048 (1981).

[32] J. P. Perdew and Y. Wang, Phys. Rev. B, **45**, 13244 (1992).

[33] J. P. Perdew, K. Burke and M. Ernzerhof, Phys. Rev. Lett., **77**, 3865 (1996).

[34] H. J. Monkhorst and J. Pack, Phys. Rev. B, **13**, 5188 (1976).

[35] F. Ortmann, F. Bechstedt and W. G. Schmidt, Phys. Rev. B, **73**, 205101 (2006).

[36] A. Tkatchenko and M. Scheffler, Phys. Rev. Lett., **102**, 073005 (2009).

[37] M. Pravica, Y. Liu, J. Robinson, N. Velisavlijevic, Z. Liu and M. Galley, J. Appl. Phys., **111**, 103534 (2012).

[38] M. M. Bishop, R. S. Chellappa, M. Pravica, J. Coe, Z. Liu, D. Dattlebaum, Y. Vohra and N. Velisavlijevic, J. Chem. Phys., **137**, 174304 (2012).

[39] J. Joseph and Eluvathingal D. Jemmis, J. Am. Chem. Soc., **129**, 4620 (2007).

[40] X. Li, Lei Liu and H. B. Schlegel, J. Am. Chem. Soc., **124**, 9639 (2002),

[41] N. V. Latypov, J. Bergman, A. Langlet, U. Wellmar and U. Bemm, Tetrahedron, **54**, 11525 (1998).

[42] P. B. Kempa and M. Herrmann, Part. Part. Syst. Charact., **22**, 418 (2005).

[43] J. Evers, T. M. Klapotke, P. Mayer, G. Oehlinger and J. Welhch, Inorg. Chem., **45**, 4996 (2006).

[44] M. -J. Crawford, J. Evers, M. Göbel, P. Mayer, G. Oehlinger and J. M. Welch, Propellants, Explosives, pyrotechnics, **32**, 478 (2007).

[45] M. Pravica, M. Galley, C. Park, H. Ruiz and J. Wojno, High Pressure Research, **31**, 80 (2011).

[46] Xue-Zhong Fan, Ji-zhen Li and Zi-ru Liu, J. Phys. Chem A, **111**, 13291 (2007).

[47] G. hong-Xu, Z. Feng-Qi, H. Rong-Zu, P. Qin, W. Bo-Zhou, Y. Zu-Wu, G. Yin, G. Sheng-Li and S. Qi-Zhen Chi, Jou. Chem., **24**, 177 (2006).

[48] Z. A. Dreger, Y. Tao and Y. M. Gupta, Chem. Phys. Lett., **584**, 83 (2013).

Chapter 6

Structural properties and quasiparticle band gaps of organic (C-H-N-O) based energetic solids

This chapter mainly presents the results of ground state structural and electronic properties for a series of C-H-N-O based energetic materials using beyond standard Density Functional Theory (DFT) methods.

6.1 Introduction

Energetic materials are good candidates for many civil, industrial and military applications due to their capability of rapid chemical decomposition with a large energy release to their surroundings by an external stimuli. Recently, a large community of researchers have shown interest on these compounds, conducting their research with new strategies to improve the performance, effectively dealing with safety and have developed new compounds which are less hazardous to the environment. Presently, experiments on these materials are increasing in order to explore the structural, optical and chemical decomposition mechanisms [1–16]. Indeed complex crystal structure and high sensitivity to a small external stimuli of these compounds presents difficulties to experimentalists in examining the desired properties such as analysis of the bonding, stability, and studying the polymorphic phases of these materials. On the other hand, theoretical assessment on these materials is an alternative method to provide a description of the structural and electronic properties at various conditions.

Density functional theory (DFT) is an efficient computational tool, and the

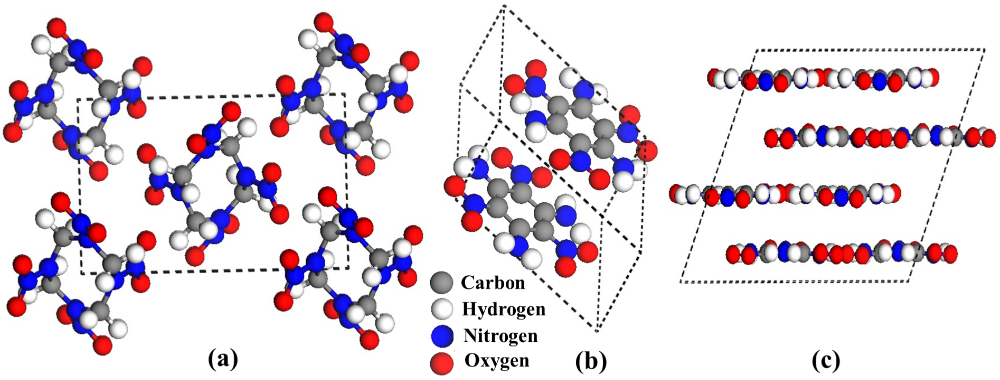

Figure 6.1: Experimental crystal structures: (a) β-HMX, (b) unit cell of TATB and (c) super cell of TATB.

usage of this method resulted in significant advances for various materials. Conventional DFT methods with existing standard approximations to the exchange-correlational functionals (modeled using the local density approximation (LDA) [17] or the generalized gradient approximation (GGA) with different flavors such as PBE [18] or PW91 [19]) are in excellent agreement with experiments for covalent and metallic systems. However standard DFT has two major general drawbacks in: 1) treating long range dispersive interactions and 2) predicting (and reproducing) the band gap from Kohn-Sham eigenvalues. In fact, these two problems play an important role in energetic materials to determine the structure, bonding, and sensitivities, as described below.

It is known that most of the energetic materials are molecular solids (including layered compounds), where the crystal packing between adjacent molecules is governed by both van der Waals interactions and hydrogen bonding (as particulary observed in C-H-N-O based molecular crystals). For example the structures of two widely used high energetic materials, β-HMX and TATB, are shown in Figure. 6.1. Earlier, Byrd and co-workers [20, 21] studied different energetic materials with conventional DFT method using various exchange-correlational functionals (such as LDA, PBE, and PW91). Their results clearly show large errors in reproducing the ground state volume. The discrepancy between theory and experiments leads to difference in the density (ρ_0), which has drastic effects in reproducing the energetic properties of these solids in terms of detonation velocity ($D_v \propto \rho_0$) and pressure ($D_p \propto {\rho_0}^2$). This deviation in reproducing ground state volumes using conventional DFT method was expected due to the fact that non local dispersive interactions were not accounted in their calculations. To correct this discrepancy between available experiments and DFT results for the ground state volumes, it is essential to include dispersive interactions in the calculations. There have been promising attempts made to fix this shortcoming and considerable benchmarking studies are available with advanced methods for noble gas solids, layered, sparse and molecular crystals [22–32]. In the case of energetic materials, Sorescu et al [33] performed calculations using Grimme's [34] method for 10 systems and obtained improved results with an error for the ground state volumes ranging from ~(-3 to 4) %. In addition, Landervilli et al. reported ground state volumes and bulk moduli for some energetic materials using Neuman and Perrin approach [35]. From our previous studies on nitromethane and FOX-7 solids [36, 37], we also found good agreement using Grimme and TS methods [36, 37]. However, it is observed that although the mentioned dispersion corrected methods overcomes most of the difficulty in reproducing ground state volumes, the relative errors still show a mean absolute deviation of about 3 %.

Another important property concerning energetic materials is the electronic band gap. Earlier, Kuklja and coworkers estimated the narrowing of the band gap using molecular level calculations for different energetic materials from ambient to high pressure and studied the key role of band gap as well as electronic excitations on the decomposition process [38–42] Few other studies were also proposed to model the link between the impact sensitivity and the electronic band gap with the PBE functional (for polymorphs of HMX, CL20 and the nitraromatic series MATB, DATB, and TATB), and reported that the lower is the band gap, then higher is the sensitivity [43, 44]. But the well known disagreement of the computed band gap using standard DFT functionals leads to an inaccurate estimation of the properties related to the band gap either in molecular or solid systems. However from our previous studies on some energetic materials (solid nitromethane, FOX-7, cynauric triazide) [36, 37, 45] and another theoretical study on TATB by Fedorov et al [46], and also previous reports using the GW

Table 6.1: Summary of simulated structures(Ref 53–58) used in the present work. All the calculations were performed using the kinetic energy cut off of 800 eV. Here, CS: Crstal structure, SG: space group, Z: no of formulas per unit cell, N: no of atoms per unit cell., V: volume in Å^3.

Compound	CS	SG	Z (N)	V
β-HMX ($C_4H_8N_8O_8$)	Monoclinic	$P2_1/c$	4 (56)	519.39
TATB ($C_6H_6N_6O_6$)	Triclinic	P1	2 (48)	442.49
NTO ($C_2H_2N_4O_3$)	Monoclinic	$P2_1/c$	4 (44)	450.29
TEX ($C_6H_6N_4O_8$)	Triclinic	P1	2 (48)	433.64
TAG ($C_3H_{12}N_{12}O_2$)	Triclinic	P1	2 (58)	525.60
FOX-7 ($C_2H_4N_4O_4$)	Monoclinic	$P2_1/c$	4 (56)	515.89

approximation [47–52] can overcome this problem.

In this chapter , we aim to carry out theoretical study of C-H-N-O based energetic solids for understanding the relative errors in structural properties using various dispersion correction methods and quasiparticle band structure calculations to obtain accurate band gaps values. For this, we have chosen different energetic solids (namely β-HMX, TATB, NTO, TEX, TAG-MNT and FOX-7) to compare the obtained results with available experiments as well previous reports. Here, the computed energetic solids are popularly known compounds in which the inter (intra) molecular interactions resembles with mixed nature of both van der Waals and hydrogen bonding. In addition, the quasiparticle band gaps of these compounds are not yet reported except for TATB [46]. The experimental crystal structure details and the corresponding information are presented in Table. 6.1. It is also to be noted that performing both structural and quasiparticle band structure calculations for the above mentioned compounds are computationally expensive (see Table 1 for structural details [53–58]), and hence we confined our self with six compounds.

6.2 Computational details

The calculations in the present work were carried out with the projector augmented wave (PAW) [59] implementation of VASP [60]. The generalized gradient approximation (GGA) in the PBE parameterization was considered as the exchange correlational functional [18]. Structural optimizations were achieved by setting following convergence criterions: for total energies are below 5e-06 eV, residual forces to be less than 1e-3 eV/ and stresses are limited to 0.02 GPa. To correct the missing dispersion interactions, we have used several recently proposed methods such as PBE functional with pair potential methods D2, D3 (BJ), TS , TS+SCS and density functional (vdW-DF) methods as implemented in the VASP code. The details of the implementations and usage of these methods can be found elsewhere (Ref. 34, 61–64). To obtain accurate band gaps, we have used the GW approximation [65, 66] for all the compounds. For getting accurate quasiparticle eigenvalues, we used 200 bands for the summation over the bands in the polarizability and the self-energy formulas, and the polarizability matrices were calculated up to a cut-off of 200 eV.

6.3 Results and discussions

6.3.1 Ground state volume and bulk modulus

Firstly, geometry optimizations were performed for six organic energetic solids with the various methods mentioned in the previous section. The complete list of resulting lattice parameters and angles, along with experimental results for all the compounds are presented in Table. 6.2. As expected, the PBE functional overestimated the lattice parameters (around 5 %) and in some cases the monoclinic and triclinic angles are slightly too low (around 1 %). Overall the PBE functional overestimated the volumes ranging from 7 to 15 % as compared with experiments for the tested compounds. On the other hand, various dispersion corrections to the PBE functional lead to an improvement in the structural parameters and the obtained results are in good agreement with experiments. Now, we will take a look into the accurate dispersion correction method for organic energetic solids in the present work. In order to enable this, we tested the percentage of relative error ($\triangle X = ((X_{cal}-X_{exp})/X_{exp})\times 100$) in the lattice parameters, volumes and densities using various dispersion corrections. The obtained $\triangle$X with dispersion correc-

Table 6.2: Calculated ground-state properties of CHNO based secondary explosives at ambient pressure using PAW method implemented in VASP.

System	GGA+D	a (Å)	b (Å)	c (Å)	α	β	γ
β-HMX	PBE	6.77	11.48	9.01	90.00	124.24	90.00
	TS	6.56	11.07	8.76	90.00	124.54	90.00
	TS+SCS	6.57	11.10	8.78	90.00	124.38	90.00
	D2	6.54	10.91	8.67	90.00	124.24	90.00
	D3 (BJ)	6.56	11.02	8.72	90.00	124.26	90.00
	vdW-DF	6.53	10.87	8.67	90.0	124.39	90.00
	Exp (Ref. 53)	6.54	11.05	8.70	90.00	124.30	90.00
TATB	PBE	9.26	9.28	7.65	106.15	92.05	120.11
	TS	9.10	9.12	6.74	109.23	91.74	119.96
	TS+SCS	9.10	9.12	6.75	108.85	91.95	120.02
	D2	9.08	9.10	6.57	109.58	91.77	119.90
	D3 (BJ)	9.07	9.10	6.77	108.95	91.81	119.87
	vdW-DF	9.08	9.10	6.62	109.16	92.13	120.03
	Exp (Ref. 54)	9.01	9.03	6.81	108.59	91.82	119.97
NTO	PBE	9.32	5.69	9.68	90.00	100.05	90.00
	TS	9.25	5.50	9.19	90.00	100.73	90.00
	TS+SCS	9.21	5.53	9.23	90.00	100.63	90.00
	D2	9.23	5.49	9.02	90.00	101.02	90.00
	D3 (BJ)	9.24	5.51	9.17	90.00	100.72	90.00
	vdW-DF	9.38	5.47	8.97	90.00	101.70	90.00
	Exp (Ref. 55)	9.33	5.45	9.04	90.00	101.47	90.00
TEX	PBE	7.20	7.91	9.32	82.41	75.48	78.29
	TS	6.90	7.65	8.94	82.32	75.19	78.69
	TS+SCS	6.90	7.65	8.94	82.84	75.67	79.00
	D2	6.85	7.63	8.78	82.21	75.29	78.91
	D3 (BJ)	6.91	7.67	8.92	82.33	75.30	78.80
	vdW-DF	6.82	7.62	8.76	82.15	75.13	79.02
	Exp (Ref. 56)	6.84	7.64	8.78	82.37	75.050	79.46
TAG	PBE	7.17	8.17	10.52	100.23	102.96	103.68
	TS	6.90	7.98	10.39	100.63	104.39	102.75
	TS+SCS	6.92	7.99	10.39	100.54	104.18	102.86
	D2	6.79	7.96	10.33	101.94	103.93	102.53
	D3 (BJ)	6.90	7.98	10.37	100.93	103.90	103.03
	vdW-DF2	6.85	7.97	10.51	101.39	104.58	102.25
	Exp (Ref. 57)	6.87	7.98	10.52	101.31	103.78	103.12

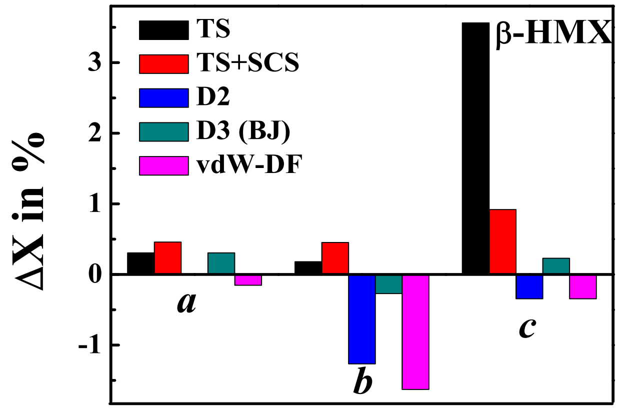

(a)

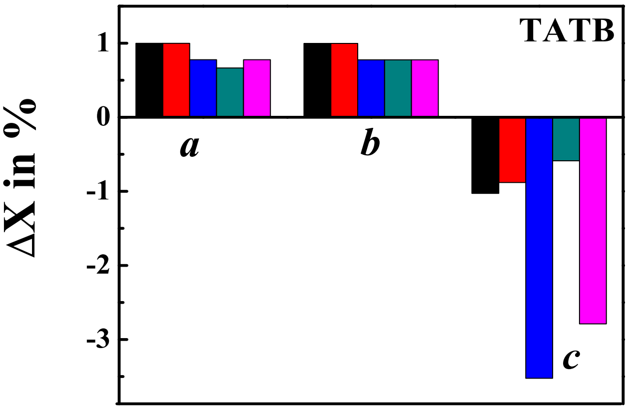

(b)

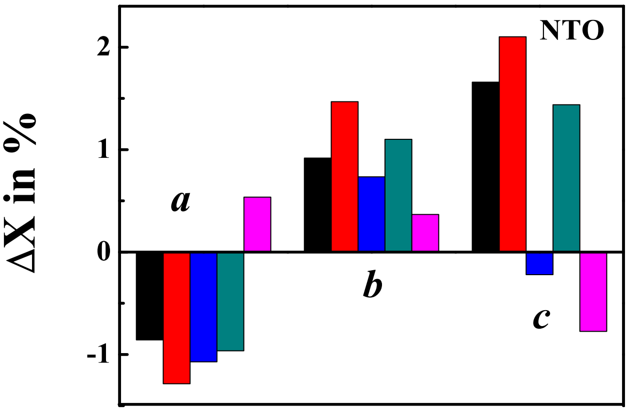

(c)

Figure 6.2: Calculated relative errors (in %) of lattice parameters (*a*, *b*, and *c*) for organic energetic solids. (a). β-HMX, (b). TATB, (c). NTO.

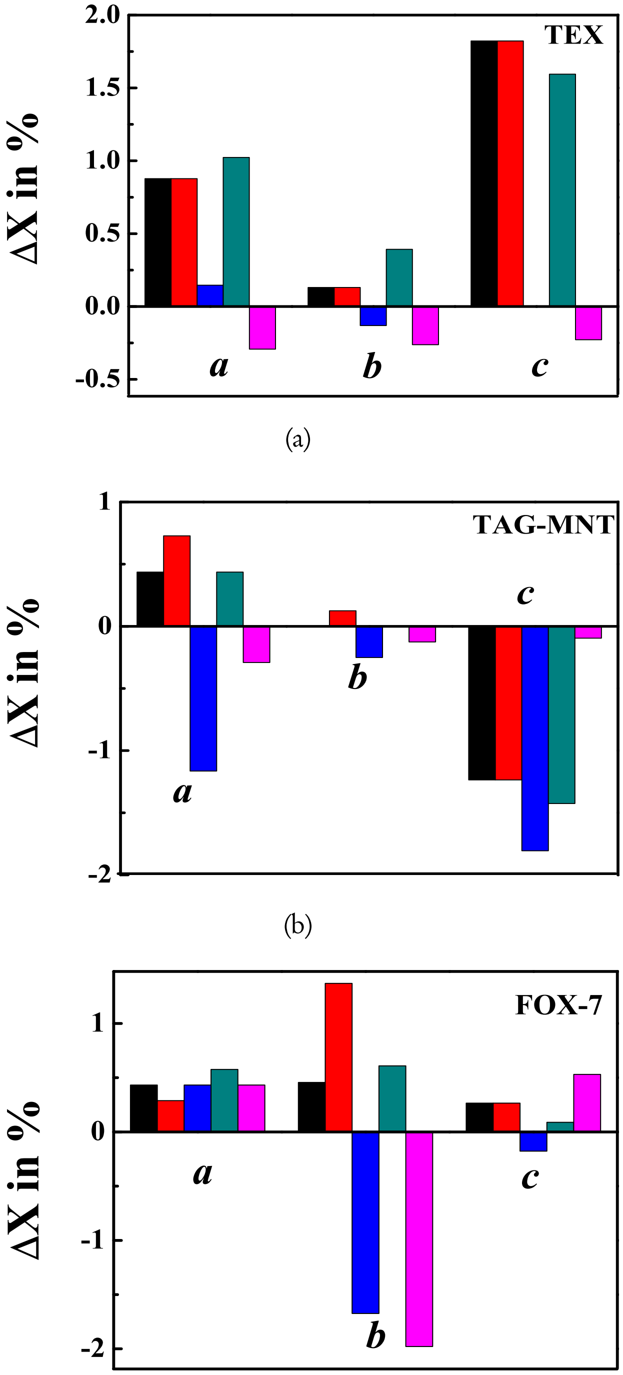

(a)

(b)

(c)

Figure 6.3: Calculated relative errors (in %) of lattice parameters (*a*, *b*, and *c*) for organic energetic solids. (a). TEX, (b).TAG-MNT, (c). FOX-7.

tions for lattice parameters are shown in Figure. 6.2, 6.3 and △X for volumes are illustrated in Table. 6.3.

From Figure. 6.2 and 6.3 , it is clear that △X (X= *a*, *b*, and *c*) for lattice parameters using different approaches varies from -3 to +3 % for all compounds and none of the individual method achieved consistently minimal error results for the tested systems. Obviously this may expected due to the mixed nature of vdW forces and hydrogen bonding in these organic energetic solids. For example, the considered compounds TATB as well as FOX-7 are layered solids and layers are dominated with vdW forces (along c-axis for TATB and b-axis for FOX-7) and hydrogen bonding is also an inherent accessible (C/N...O-H bonding pairs) for stability of these structures.

To further understand the performance of each functional, we considered the equilibrium volumes obtained with the various methods. Turning now to Table. 6.3, the mean absolute deviation (MAD) of all dispersion correction methods are almost within a 1-2 % deviation with experiments and △V in the equilibrium volumes are scattered with each method used. For instance, by considering a case of less than 1 % relative error at equilibrium volume, we found a good agreement with: the TS and D3(BJ) methods for β-HMX; the TS, TS+SCS and D3(BJ) methods for TATB; the D2 and vdW-DF methods for NTO and TEX systems. In contrast to these, all the dispersion corrected schemes (except D2) were found to show $<$ 1 % deviation for TAG-MNT and above 1 % of deviation for FOX-7 in comparison with experiments. In addition to the present work, Sorescu et al [33] found -1.18 % for β-HMX, -3.24 % for TATB, and -0.48 % for FOX-7 using the PBE-D2 method; a deviation of -2 % was observed for β-HMX and TATB using the Neuman and Perrin approach [35] ; Wu et al [67] reported the ground state volume of NTO with a deviation of -0.6 % using the D2 method. At this point, these observations indicates that dispersion correction methods replicate the volume with experiments, but the performance of each method is not unique for different compounds.

We next move to analyse the calculated density, which is an intrinsic parameter to determine explosive properties in energetic solids. As mentioned in the introduction $D_v \propto \rho$ and $D_p \propto \rho^2$ for energetic solids, in Figure. 6.4 we plot the

Table 6.3: The calculated ground state volumes V (in Å), % of relative error ($\triangle$V) with experiments (see Table. 6.1 for experimental volumes) with standard DFT method (PBE) and different dispersion corrected methods.

		PBE	TS	TS-SCS	D2	D3(BJ)	vdW-DF
β-HMX	V	578.70	524.05	528.38	510.75	520.56	507.26
	$\triangle$V	+11.42	+0.90	+1.73	-1.66	+0.22	-2.33
TATB	V	534.28	443.92	445.91	430.32	445.47	433.40
	$\triangle$V	+20.74	+0.32	+0.77	-2.75	+0.67	-2.05
NTO	V	504.87	458.81	462.09	448.86	458.99	450.68
	$\triangle$V	+12.12	+1.89	+2.62	-0.32	+1.93	+0.09
TEX	V	501.40	444.86	447.57	433.16	446.86	430.23
	$\triangle$V	+15.63	+2.59	+3.21	-0.11	+3.04	-0.77
TAG-MNT	V	565.95	523.03	525.55	508.36	521.41	522.93
	$\triangle$V	+07.6	-0.49	$\sim$0.00	-3.28	-0.80	-0.51
FOX-7	V	598.61	522.54	526.78	508.62	521.94	510.19
	$\triangle$V	+16.03	+1.28	+2.11	-1.41	+1.10	+1.17
MAD		14.23	1.24	1.74	1.59	1.30	1.14

obtained $\triangle\rho$ as well $\triangle\rho^2$ for all compounds. Similar to ground state volume, $\triangle\rho$ also varies around -2 to 2 % with various methods and $\triangle\rho^2$ was enhanced to -5 to 5 % with various dispersion correction methods. However, this tendency of relative error in ρ^2 should be considered towards predicting explosive properties such as detonation pressure.

As a next step we also calculated the bulk moduli of organic energetic solids to check the performance of various dispersion correction methods. Besides the ground state volume and density, a similar situation was observed even in the computed bulk moduli for these compounds using various methods. Table. 6.4 shows the obtained bulk moduli (B_0) and their pressure derivatives (B') along with available experimental values. Here, B_0 and B' were computed with the Murnaghan equation of state, where the P-V data were fitted from 0 to 5 GPa with a step size of 0.5 GPa. By comparing the computed B_0 from various dispersion correction DFT methods with the available experimental values, one can understand that the obtained values fall in the range of experiments. We also note that the present computed ground state volume, bulk moduli and pressure derivatives for

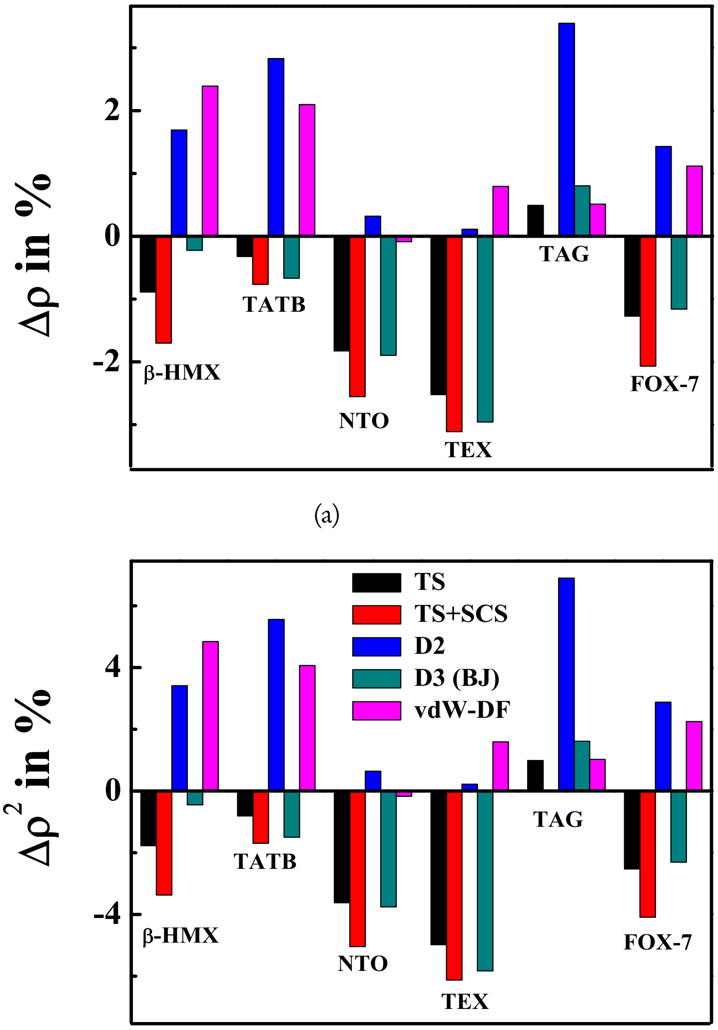

(a)

(b)

Figure 6.4: Calculated relative errors (in %) of density (ρ) for organic energetic solids. Here (a)$\triangle\rho$ and (b)$\triangle\rho^2$ are tested with various dispersion correction methods in the present work.

Table 6.4: The calculated Bulk moduli and its pressure derivative of energetic materials with standard DFT method and different dispersion corrected methods.

Compound	Method	B_0 (B')	Exp
β-HMX	PBE	9.24 (7.27)	
	TS	16.07 (7.84)	
	TS+SCS	14.03 (8.06)	12.4 (10.4)[68]
	D2	17.34 (7.85)	21.0 (7.4)[69]
	D3 (BJ)	15.93 (7.38)	
	vdW-DF	20.98 (8.58)	
TATB	PBE	3.49 (12.66)	
	TS	21.12 (6.30)	
	TS+SCS	17.78 (7.74)	15.7 (8.0)[70]
	D2	14.12 (10.82)	
	D3 (BJ)	14.27 (7.91)	
	vdW-DF	20.95 (7.85)	
TAG-MNT	PBE	5.24 (11.42)	
	TS	20.37 (3.47)	
	TS+SCS	20.65 (3.37)	14.6 (4.8)[71]
	D2	18.72 (4.30)	
	D3 (BJ)	19.59 (3.35)	
	vdW-DF	21.00 (3.83)	
NTO	PBE	11.32 (6.65)	
	TS	21.60 (5.27)	
	TS+SCS	20.29 (5.81)	
	D2	18.06 (6.20)	
	D3 (BJ)	18.68 (6.15)	
	vdW-DF	25.15 (4.26)	
TEX	PBE	7.26 (8.41)	
	TS	15.70 (7.30)	
	TS+SCS	14.38 (6.89)	
	D2	16.91 (7.30)	
	D3 (BJ)	13.51 (8.14)	
	vdW-DF	20.66 (7.75)	

β - HMX and TATB are comparable with previous reports using D2 as well as Neuman and Perrin approaches [33, 35], and to the best of our knowledge experimental or any dispersion corrected DFT calculations for NTO, TEX compounds are not available.

From the corresponding results of ground state volumes, densities and bulk moduli with different dispersion schemes, it is observed that the *best performing* dispersion corrected DFT method for C-H-N-O based energetic solids particularly depends on the chemical environment of the respective crystal. In other words, the chemical bonding (intra as well as inter molecular interactions) in these C-H-N-O based energetic solids are significantly dominated with mixed nature of van der Waals forces and hydrogen bonding, while the geometrical arrangement in these complexes are different from one another. This might be the cause that the computed relative errors are quite different for tested systems. Note that, our preliminary results are in line with recent report on high nitrogen-content energetic salts using various dispersion correction methods [72]. We also consider that, it would be essential to perform theoretical calculations by verifying proper dispersion correction method to qualitative predict important explosive properties such as D_p or D_v, and other properties like elastic or dynamics, polymorphism.

6.3.2 Quasiparticle band gaps

As mentioned in introduction of this chapter, the previous models with standard GGA/LDA methods projected the key role of electronic band gap to understand the sensitivity or decomposition mechanism of energetic materials at various pressure conditions. However, it is a known fact that standard DFT methods have shortcoming in predicting/reproducing band gap due to the derivative discontinuity of the functionals and there is a prerequisite for determining accurate band gap values inorder to propose theoretical models for energetic solids. Therefore, to investigate the fundamental electronic band gap of these energetic solids, we have performed quasiparticle band structure calculations with the GW approximation (G_0W_0) method for the experimental crystal structures. The computed GGA-PBE and G_0W_0 band structures for prototype energetic material solid ni-

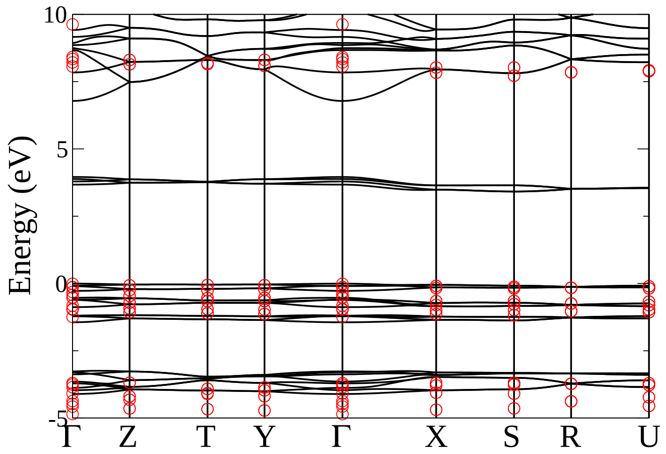

Figure 6.5: Calculated quasiparticle band structures of prototype energetic material solid nitromethane at experimental lattice parameters.

tromethane and other energetic solids are presented in Figure. 6.8, 6.6 and 6.7. From the computed band structures, it is observed that bands near the fermi level are nearly flat with both methods and as compared with PBE band structures, a wide upshift in the conduction band minimum was noticed after taking the quasiparticle correction with PBE functional. Specifically, we found nearly 40 % increment in the computed band gaps for all compounds which substantiate the necessity of quasiparticle corrections to calculate the electronic band gap of these systems. A systematic comparison of our calculated band gaps with G_0W_0 as well as PBE is presented in Figure. 6.9. From this, we noticed that all these C-H-N-O based energetic materials are wide band gap insulators, ranging from 4 to 8 eV (310 to 155 nm), while PBE results yield only from 2 to 4 eV (600 to 300 nm). Since, very limited information is available regarding experimental band gaps (only available for β-HMX and TATB in the present work) of energetic solids, we directly compare our quasiparticle band gaps with available values from absorption spectra. For, β- HMX, the fundamental optical absorption peaks exhibited near to UV region from experiments [73, 74], ranging from at 5.32-6.39 eV (233-194), while the obtained quasiparticle is 7.1 eV (172 nm). The computed

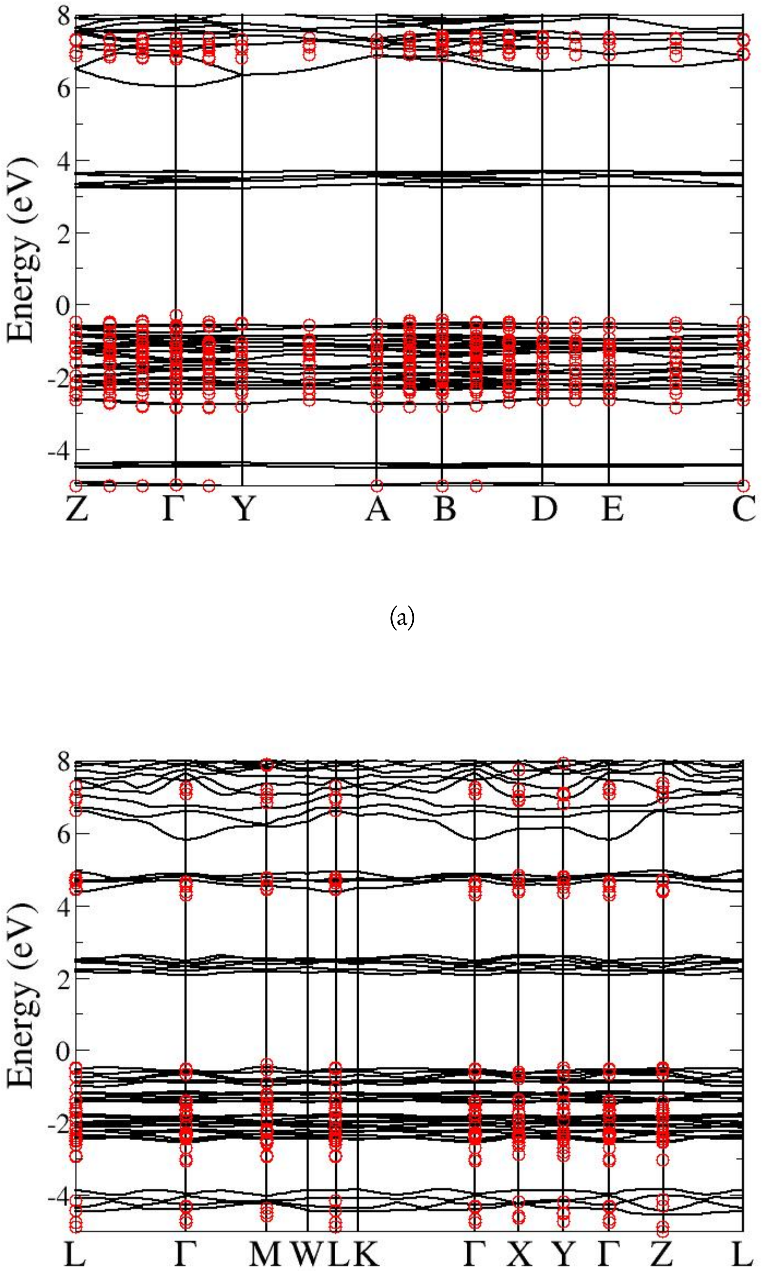

(a)

(b)

Figure 6.6: Calculated quasiparticle band structures of organic energetic solids. (a.β-HMX, (b). TATB at experimental lattice parameters.

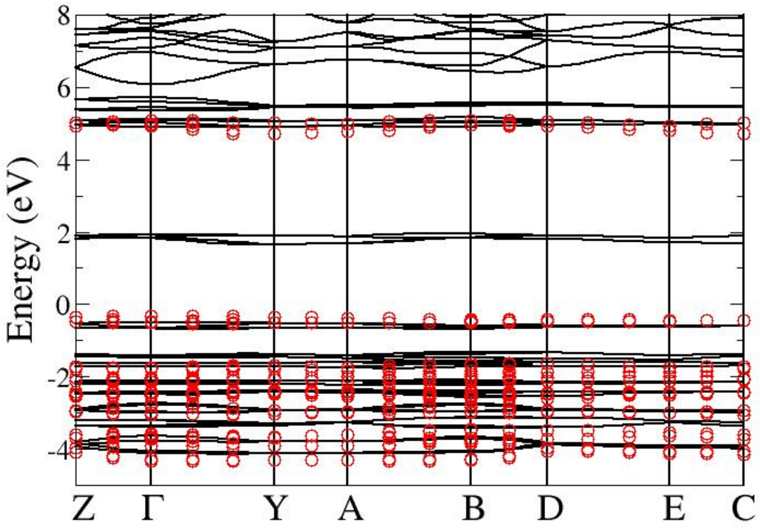

(a)

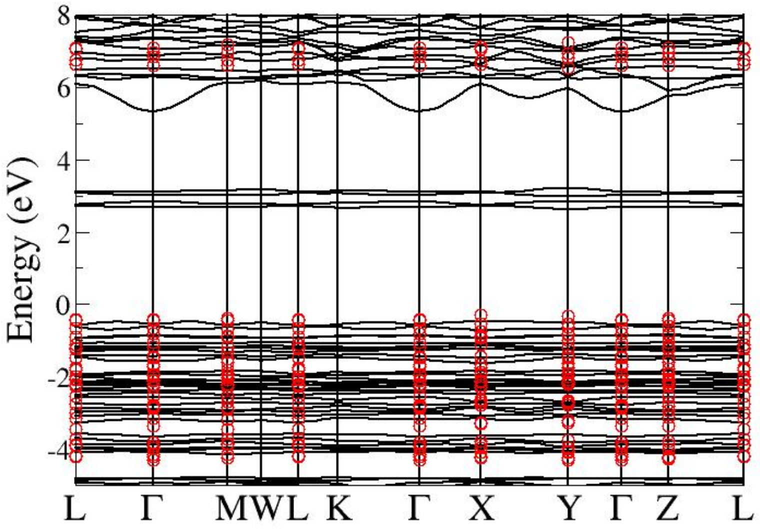

(b)

Figure 6.7: Calculated quasiparticle band structures of organic energetic solids.(a) NTO, (b) TEX at experimental lattice parameters.

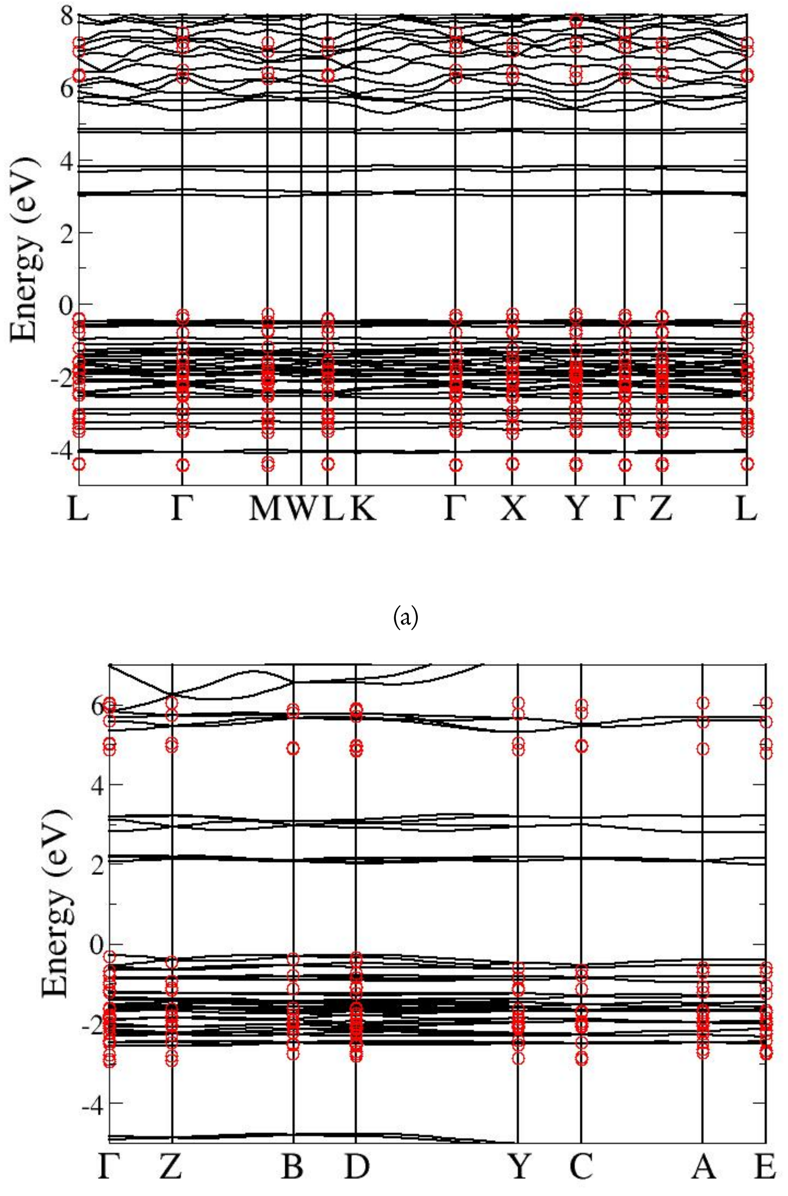

(a)

(b)

Figure 6.8: Calculated quasiparticle band structures of organic energetic solids.(a. TAG-MNT, (b). FOX-7. at experimental lattice parameters.

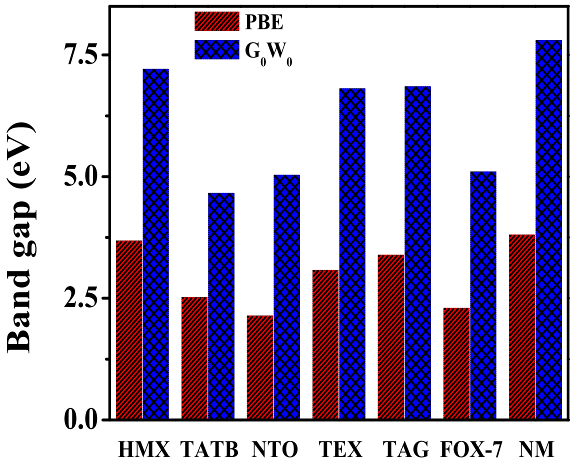

Figure 6.9: Calculated G_0W_0(PBE) band gaps (in eV) for a series of energetic materials. Here the band gaps (in eV) are: for HMX: 7.21 (3.68), TATB: 4.66 (2.52), NTO: 5.03 (2.14), TEX: 6.81 (3.08), TAG : 6.85 (3.39), FOX-7[36]: 5.1 (2.3) and NM[37]: 7.8 (3.8)

G_0W_0 band gap of TATB (4.66 eV) is in excellent agreement with previously reported value of 4.29 eV [46] and relatively low when compare to the experimental value (6.5 eV) using X-ray absorption spectroscopy [75].From these it is found that, the obtained G_0W_0 band gap of β-HMX is overestimated (around 1.69-0.62 eV) with experiments, whereas TATB value is lower than experiments by 1.8 eV in the present work. To the best of our knowledge, the experimental band gaps or absorption spectra for NTO, TEX, TAG-MNT and FOX-7 are not available in the literature. It is to be noted that photoemission experiments are necessary to examine the real band gap for any material and the present results may provide useful inputs to perform experiments. On the other hand, the differences between obtained G_0W_0 band gaps and available absorption regions of energetic solids might be due to the major role of exciton effects, which is beyond the scope of this thesis work. For instance, electronic excitations were observed experimentally for few of the energetic solids such as nitromethane (at 226 nm), RDX (at 230 nm), dimethylnitramine (at 236 nm) and PETN (at 193 nm) [14–16, 73].

Besides the comparison of band gaps with experiments, the results from quasiparticle corrections with PBE insights the necessity of theoretical models to go beyond GGA methods. For example, a quantitative assessment of metallization of pure/defect energetic solids may be expected at high pressures using quasiparticle methods as compared with standard PBE method (see Ref. 76–78). Also, considering other previous theoretical model on *band gap vs impact sensitivity* of energetic solids, it is necessary to revisit the same model with higher than standard GGA/LDA level.

6.4 Conclusions

In summary, we have performed first principles calculations for several energetic materials concerning their structural and electronic properties, which strongly suggest the necessity to go beyond standard DFT. Firstly, we have shown that dispersion corrected methods are necessary to provide an improvement in the calculated volumes to compare with experiments. Furthermore, the mean absolute deviation in theoretical volumes for all tested methods are similar (around 1.2 to 1.8 %) and the performance of relative errors on structural properties calculated using each method varies with an order of $\sim (0-3.5)$ % for different compounds in the present work. Additionally, similar situation was observed for other volume dependent properties such as density and bulk moduli. The present observations clearly demonstrated that one has to test with all the dispersion corrected DFT methods for C-H-N-O based energetic solids before concluding the ground state properties. So that other related explosive properties(detonation pressure or velocity), polymorphic phase transitions, mechanical properties and many more can be predicted with resonalble accuracy. Besides this, we have calculated the dispersion corrected bulk moduli in the low pressure region which suggests the soft nature of these materials. Secondly, the use of quasiparticle band structure calculations indicate a significant enhancement (nearly 40 %) in the band gap in comparison with the results obtained with the PBE functional, which emphasis the wide band gap insulating nature of energetic solids. The calculated fundamental band gap for β-HMX as well as TATB are far from the reported experimental optical absorption values, which might indicate that excitation binding energies play an important role in these compounds. By comparing the present G_0W_0 band gaps with available previous reports on other energetic solids, it open up the necessary for future calculations including electronic excitons within G_0W_0 or higher methods to examine the decomposition mechanism of these energetic solids and possible metallization under pressure. It is manidate to revisit the previous model of *band gap with impact sensitivities* for energetic solids within similar structure or polymorphic phases beyond standard PBE method. Finally, the present work will stimulate experiments to perform photoemission study on the above compounds.

References

[1] V. I. Tarzhanov, *Fast Initiation of Explosives, Special Regimes of Detonation: A Collection of Articles*, RFYaTs VNIITF: Snezhinsk (1998).

[2] N. K. Bourne, Proc. R. Soc. London A, **457**, 1401-1426 (2001).

[3] E. D. Aluker, B. P. Aduev, Yu. A. Zakharov, A. Y. Mitrofanov and A. G. Krechetov, *In Focus on Combustion Research*, Novapublishers: New York, NY, USA, 55–58 (2006).

[4] E. D. Aluker, A. G. Krechetov, A. Y. Mitrofanov, A. S. Zverev and M. M. Kuklja, J. Phys. Chem. C, **116**, 24482-24486 (2012).

[5] E. D. Aluker, A. G. Krechetov, A. Y. Mitrofanov, D. R. Nurmukhametov and M. M. Kuklja, J. Phys. Chem. C, **115**, 6893-6901 (2011).

[6] R. V. Tsyshevsky, O. Sharia and M. M. Kuklja, J. Phys. Chem. C, **118**, 9324-9335 (2014).

[7] J. Sharma, B. C. Beard and M. Chaykovsky, J. Phys. Chem, **95**, 1209-1213 (1991).

[8] F. J. Owens and J. Sharma, J. Appl.Phys, **51**, 1494-1497 (1980).

[9] H. -S. Im, and E. R. Bernstein, J. Chem.Phys., **113**, 7911-7918 (2000).

[10] Z. Yu and E. R. Bernstein, J. Chem.Phys., **135**, 154305:1-10 (2011).

[11] Z. Yu and E. R. Bernstein, J. Chem.Phys.,**137**, 114303:1-11 (2012).

[12] Z. A. Dreger, Y. A. Gruzdkov, Y. M. Gupta and J. J. Dick, J. Phys. Chem. B, **106**, 247-256 (2002).

[13] M. Greenfield, Y. Q. Guo and E. Bernstein, Chem. Phys. Lett., **430**, 277-281 (2006).

[14] A. Bhattacharya, Y. Guo and E. A. Bernstein, J. Chem. Phys., **136**, 024321:1-9 (2012).

[15] P. A. Mullen and M. K. Orloff, J. Phys. Chem., **77**, 910-911 (1973).

[16] Z. Yu and E. R. Bernstein, J. Chem. Phys., **135**, 154305:1-10 (2011).

[17] J. P. Perdew and A. Zunger, Phys. Rev. B, **23**, 5048-5079 (1981).

[18] J. P. Perdew, K. Burke and M. Ernzerhof, Phys. Rev. Lett., **77**, 3865-3868 (1996).

[19] J. P. Perdew and Y. Wang, Phys. Rev. B, **45**, 13244-13249 (1992).

[20] E. F. C. Byrd, G. E. Scuseria and C. F. Chabalowski, J. Phys. Chem. B, **108**, 13100-13106 (2004).

[21] E. F. C. Byrd and B. M. Rice, J. Phys. Chem. C, **111**, 2787-2796 (2007).

[22] BucT. ko, J. Hafner, S. Lebègue and J. G. Ángyán, J. Phys. Chem. A, **114**, 11814-11824 (2010).

[23] A. O. -D. -L. -Roza and E. R. Johnson, J. Chem. Phys., **137**, 054103:1-10 (2012).

[24] J. Klimes and A. Michaelides, J. Chem. Phys., **137**, 120901:1-12 (2012).

[25] T. Risthaus and S. Grimme, J. Chem. Theory Comput., **9**, 1580-1591 (2013).

[26] T. Bucko, S. Lebègue, J. Hafner and J. G. Ángyán, Phy. Rev. B, **87**, 064110-1:15 (2013).

[27] K. Berland and P. Hyldgaard, Phy. Rev. B, **87**, 205421-1:15 (2013).

[28] T. Bucko, S. Lebègue, J. Hafner and J. G. Ángyán, J. Chem. Theory Comput., **9**, 4293-4299 (2013).

[29] A. M. Reilly and A. Tkatchenko, J. Phys. Chem. Lett., **4**, 1028-1033 (2013).

[30] T. Bucko, S. Lebègue, J. G. Ángyán and J. Hafner, J. Chem. Phys., **141**, 034114:1-17 (2014).

[31] J. Moellmann and S. Grimme, J. Phys. Chem. C, **118**, 7615-7621 (2014).

[32] L. Kronik and A. Tkatchenko, Acc. Chem. Res., **47**, 3208 – 3216 (2014).

[33] D. C. Sorescu and B. M. Rice, J. Phys. Chem. C, **114**, 6734-6748 (2010).

[34] S. Grimme, J. Compu. Chem., **27**, 1787-1799 (2006).

[35] A. C. Landerville, M. W. Conroy, M. M. Budzevich, Y. Lin, C. T. White and I. I. Oleynik, Appl. Phys. Lett., **97**, 251908-1:4 (2010).

[36] S. Appalakondaiah, G. Vaitheeswaran and S. Lebègue, J. Chem. Phys., **138**, 184705:1-10 (2013).

[37] S. Appalakondaiah, G. Vaitheeswaran and S. Lebègue, J. Chem. Phys., **140**, 014105:1-7 (2014).

[38] M. M. Kuklja, Appl. Phys. A, **76**, 359-366 (2003).

[39] M. M. Kuklja, B. P. Aduev, E. D. Aluker, V. I. Krasheninin and A. Yu. Mitrofanov, J. Appl. Phys., **89**, 4156-4166 (2001).

[40] M. M. Kuklja, E. V. Stefanovich and A. B. Kunz, J. Chem. Phys., **112**, 3417-3422 (2000).

[41] S. N. Rashkeev, M. M. Kuklja and F. J. Zerilli, Appl. Phys. Lett., **82**, 1371-1373 (2003).

[42] A. B. Kunz, M. M. Kuklja, T. R. Botcher and T. P. Russell, Thermochemica Acta, **384**, 279-284 (2002).

[43] W. Zhu and H. Xiao, Struct. Chem., **21**, 657-665 (2010).

[44] H. Zhang, F. Cheung, F. Zhao and X. -L. Cheng, Int. J. Quan. Chem., **109**, 1547-1552 (2009).

[45] S. Appalakondaiah, G. Vaitheeswaran and S. Lebègue, Chem. Phys. Lett., **605-606**, 10-15 (2014).

[46] I. A. Fedorov and Y. N. Zhuravlev, Chem. phys., **436-437**, 1-7 (2014).

[47] W. -D. Schöne and A. G. Eguiluz, Phy. Rev. Lett., **81**, 1662-1665 (1998).

[48] B. Arnaud and M. Alouani, Phy. Rev. B, **62**, 4464-4476 (2000).

[49] S. Lebègue, B. Arnaud, M. Alouani and P. E. Bloechl, Phy. Rev. B, **67**, 155208-1:10 (2003).

[50] A. Fleszar and W. Hanke, Phy. Rev. B, **71**, 045207-1:11 (2005).

[51] S. Lany, Phy. Rev. B, **87**, 085112-1:9 (2013).

[52] R. H. Scheicher, D. Y. Kim, S. Lebègue, B. Arnaud, M. Alouani and R. Ahuja, Appl. Phys. Lett., **92**, 201903-1:3 (2008).

[53] C. S. Choi and H. P. Boutin, Acta Cryst., **B26**, 1235-1240 (1970).

[54] H. H. Cady and A. C. Larson, Acta Cryst., **18**, 485-496 (1965).

[55] E. A. Zhurova and A. A. Pinkerton, Acta Cryst., **B57**, 359-365 (2001).

[56] K. Karaghiosoff, T. M. Klapötke, A. Michailovski and G. Holl, Acta Cryst., **C58**, 0580-0581 (2002).

[57] T. M. Klapötke, J. Stierstorfer and A. U. Wallek, Chem. Mater., **20**, 4519-4530 (2008).

[58] U. Bemm and H. Östmark, Acta Cryst., **C54**, 1997-1999 (1998).

[59] P. E. Blöchl, Phy. Rev. B, **50**, 17953-17979 (1994).

[60] G. Kresse and J. Furthm*ü*ller, Phy. Rev. B, **54**, 11169- 11186 (1996).

[61] S. Grimme, S. Ehrlich and L. Goerigk, J. Compu. Chem., **32**, 1456-1465 (2011).

[62] A. Tkatchenko and M. Scheffler, Phy. Rev. Lett., **102**, 073005:1-4 (2009).

[63] A. Tkatchenko, Jr. R. A. DiStasio, R. Car and M. Scheffler, Phy. Rev. Lett., **108**, 236402:1-5 (2012).

[64] M. Dion, H. Rydberg, E. Schr*öd*er, D. C. Langreth and B. I. Lundqvist, Phy. Rev. Lett., **92**, 246401:1-4 (2004).

[65] L. Hedin, Phy. Rev., **139**, A796-A823 (1965).

[66] L. Hedin and S. Lundquist, *Solid State Physics*, edited by H. Ehrenreich, F. Seitz, D. Turnbull, **23**, Academic, New York (1969).

[67] Q. Wu, W. Zhu, H. Xiao, Struct. Chem., DOI: 10.1007/s11224-014-0506-3 (2014).

[68] C. -S. Yoo and H. Cynn, J. Chem. Phys., **111**, 10229-10235 (1999).

[69] J. C. Gump and S. M. Peiris, J. Appl. Phys., **97**, 053513:1-7 (2005).

[70] L. L. Stevens, N. Velisavljevic, D. E. Hooks, D. M. Dattelbaum, Propellants, Explosives,Pyrotechnics, **33**, 286-295 (2008).

[71] R. S. McWilliams, Y. Kadry, M. F. Mahmood, A. F. Goncharov and J. C. -Jenkins, J. Chem. Phys., **137**, 054501:1-12 (2012).

[72] D. C. Sorescu, E. F. C. Byrd, B. M. Rice, and K. D. Jordan, J. Chem.Theory Comput., **10**, 4982-4994 (2014),.

[73] J. K. Cooper, C. D. Grant and J. Z. Zhang, J. Phys. Chem. A, **117**, 6043-6051 (2013).

[74] K. J. Smit, Journal of Energetic materials, **9**, 81-103 (1991).

[75] S. Kakar, A. J. Nelson, R. Treusch, C. Heske, T. van Buuren, I. Jiménez, P. Pagoria and L. J. Terminello, Phys. Rev. B, **62**, 15666-15672 (2000).

[76] D. Y. Kim, S. Lebègue, C. M. Araújo, B. Arnaud, M. Alouani and R. Ahuja, Phy. rev. B, **77**, 092104:1-4 (2008).

[77] M. Ramzan, S. Lebègue and R. Ahuja, Phy. rev. B, **81**, 233103:1-4 (2010).

[78] S. Lebègue, C. M. Araujo, D. Y. Kim, M. Ramzan, H. K. Mao and R. Ahuja, PNAS, **109**, 9766-9769 (2012).

[79] N. Zohari, M. H. Keshavarz and S. A. Seyedsadjadi, J. Them. Anal. Calorim., **117**, 423-432 (2014).

Chapter 7

Summary & Future plan

In this chapter we summarize the highlighting contents and conclusions of the thesis. First principles calculations based on density functional theory (DFT) methods have been extensively employed to study the structural, vibrational as well as electronic properties of layered and molecular solids. From the obtained results, it is found that conventional density functional theory (DFT) approximations promise the description of the structural as well as dynamical properties at low computational cost for various systems and omission of long-range dispersion forces which limits the reliability of standard methods for weakly interacting solids. To extend the importance of recently proposed dispersion corrections to standard DFT, we presented a detailed study of structural, vibrational properties and stability of layered as well as molecular solids from ambient to high pressures using various dispersion corrected approaches along with standard DFT methods.

The first highlighting result of this thesis was to achieve good accuracy for inter- and intramolecular dispersion interactions for various systems such as elemental layered compound (black phosphorus), binary molecular solid (XeF_2) and a series of energetic solids. From our calculations it is found that the computed lattice constants, volumes and bulk moduli are in perfect agreement with experiments for all investigated solids at ambient conditions. In order to understand the influence of pressure on structural properties, we have performed hydrostatic pressure calculations with dispersion corrected DFT methods, and the respective results were compared with standard DFT results and available experiments. Lattice constants, bond lengths and bulk moduli obtained from the dispersion corrected DFT are in good agreement with experiments at lower pressures for elemental black phosphorus. On the other hand, dispersion corrections methods improved the structural properties at low pressures upto 10 GPa for XeF_2. In addition to this, both conventional as well as dispersion corrected DFT methods posses similar results at high pressures and are also comparable with experiments, which implies the influence of dispersion forces on bonding for XeF_2 is negligible at very high pressures upto 110 GPa. In the case of organic energetic solids (solid nitromethane and FOX-7), dispersion correction DFT methods are crucial in determining the stability of the systems due to mixed nature of van der Waals and hydrogen bonding. In particular, a possible structural transition in solid nitromethane is observed due to weakening of hydrogen bond strength, and softening of lattice modes. Besides solid nitromethane, an evidence of strong hydrogen bonding in the mid IR region which is also understood a possible reason for the structural stability of FOX-7 under hydrostatic pressure upto 10 GPa. To assess the best performing dispersion correction method for C-H-N-O based energetic solids, we have evaluated the ground state structural properties for set of organic explosives using recently reported dispersion correction methods. From the obtained results, we examine the relative errors in lattice constants, volume, and densities for a set of C-H-N-O based systems. Our calculated results on series of C-H-N-O based energetic solids revealed that the error in the theoretical volumes for all the tested methods are similar, and the performance of each method is not equal for different compounds. Furthermore, we have calculated the dispersion corrected bulk moduli in the low pressure region which suggests the soft nature of energetic solids. Our results clearly demonstrate the need to use dispersion corrected DFT for C-H-N-O energetic solids in order to predict their explosive properties or stability of these systems. The other interesting spotlight of this thesis is the systematic investigation of quasiparticle band gaps of energetic solids. From this study, it is observed that nearly 40 % increment in the computed band gaps is realized for all compounds, which substantiate the necessity of quasiparticle corrections to calculate the electronic band gap of these systems. Also, the results from quasiparticle corrections with PBE insights the necessity to go beyond GGA methods of theoretical models for predict explosive properties of any energetic solids should .

Despite this remarkable success results of the present thesis, there is still room for improvement of the present work in various aspects. Specially in the case of energetic solids, understanding the stability of the energetic solids are also further challenging issue at non-hydrostatic pressures as well as temperatures, which we will focus on our future work. Questions concerning the high pressure structures of energetic solids is an interesting area, which will provide information to the experimentalist towards synthesis new energy materials. This we will carried out using the recently developed genetic algorithm techniques. Also, it is necessary to perform defect level calculations using quasiparticle methods to propose theoretical models between band gap and decomposition process.

List of Publications

Publications included in the thesis

[1] **S. Appalakondaiah**, G. Vaitheeswaran, S. Lebègue, N. E. Christensen and A. Svane, "Effect of van der Waals interactions on the structural and elastic properties of black phosphorus", *Phy. Rev. B* **86**, 035105 (2012).

[2] **S. Appalakondaiah**, G. Vaitheeswaran, and S. Lebègue, "A DFT study on structural, vibrational properties, and quasiparticle band structure of solid nitromethane", *J. Chem. Phys* **138**, 184705 (2013).

[3] **S. Appalakondaiah**, G. Vaitheeswaran, and S. Lebègue, "Structural properties of solid nitromethane: A density functional study", *AIP. Conf. proc* **1512**, 830 (2013).

[4] **S. Appalakondaiah**, G. Vaitheeswaran, and S. Lebègue, "Structural, vibrational, and quasiparticle band structure of 1,1-diamino-2,2- dinitroethelene from ab initio calculations", *J. Chem. Phys* **140**, 014105 (2014).

[5] G. Vaitheeswaran, K. Ramesh Babu, N. Yedukondalu, and **S. Appalakondaiah**, "Structural properties of solid energetic materials: a van der Waals density functional study", *Current Science* **106**, 1219 (2014).

[6] **S. Appalakondaiah**, G. Vaitheeswaran, and S. Lebègue,, "Dispersion corrected structural properties and quasiparticle band gaps of several organic energetic solids", *Submitted to journal.*

[7] **S. Appalakondaiah**, G. Vaitheeswaran, V. Kanchana, M. C. Valsakumar, N. E. Christensen and A. Svane, "Structural stability and pressure induced metallization of molecular solid XeF_2", *manuscript under preparation.*

Publications not included in the thesis

[1] Vijay Kumar Gudelli, V. Kanchana, **S. Appalakondaiah**, G. Vaitheeswaran, and M. C. Valsakumar, "Phase stability and thermoelectric properties of the mineral FeS_2: An Ab Initio study", *J. Phys. Chem. C* **117**, 21120 (2013).

[2] **S. Appalakondaiah**, G. Vaitheeswaran, and S. Lebègue, "Structural, elastic, optical properties and quasiparticle band structure of solid cyanuric triazide", *Chem. Phys. Lett* **605-606**, 10 (2014).

[3] E. Narsimaha Rao, **S. Appalakondaiah**, N. Yedukondalu, and G. Vaitheeswaran, "Structural,electronic and optical properties of novel carbonate fluorides $ABCO_3F$ (A=K, Rb,Cs; B=Ca, Sr)", *Journal of solid state chemistry* **212**, 179 (2014).

[4] M. Sekar, N. V. Chandra Shekar, R. Babu, P. Ch. Sahu, A. K. Sinha, Anuj Upadhyay, M. N. Singh, K. Ramesh Babu, **S. Appalakondaiah**, G. Vaitheeswaran, and V. Kanchana, "High pressure structural behavior of YGa_2: A combined experimental and theoretical study", *Journal of solid state chemistry* **226**, 11 (2015).